



National Aeronautics and
Space Administration

TechBriefs



Electronic Components and Circuits



Electronic Systems



Physical Sciences



Materials



Computer Programs



Mechanics



Machinery



Fabrication Technology



Mathematics and Information Sciences



Life Sciences

INTRODUCTION

TECHNICAL BRIEFS are summaries of new technology derived from the research and development programs of the National Aeronautics and Space Administration. These Briefs emphasize information of potential interest to business and government, industrial, regional, or disciplinary lines and are issued to encourage commercial application.

Availability of NASA Tech Briefs and TSP's

Distribution of NASA Tech Briefs, a monthly periodical publication, is limited to engineers in U.S. Industry and to other domestic technology transfer agents. Requests for individual Tech Briefs or for Technical Support Packages (TSP's) announced herein should be addressed to

NASA Center for AeroSpace Information
Technology Utilization Office
P.O. Box 8757
Baltimore, MD 21240.
Telephone No. (301) 859-5300, Ext. 243, 245

Please reference the three-letter, five-digit control number located at the end of each Tech Brief. Information on NASA's Technology Utilization Program, its documents, and services is also available at the same facility.

Technology Utilization Officers and Patent Counsels are located at NASA field installations to provide technology-transfer access to industrial users. Inquiries can be made by writing to NASA field installations listed below.

Technology Utilization Officers and Patent Counsels

Ames Research Center
Technology Utilization Officer
Mail Code 223-3
Moffett Field, CA 94035

Patent Counsel
Mail Code 200-11
Moffett Field, CA 94035

Goddard Space Flight Center
Technology Utilization Officer
Mail Code 702-1
Greenbelt, MD 20771

Patent Counsel
Mail Code 204
Greenbelt, MD 20771

Lyndon B. Johnson Space Center
Technology Utilization Officer
Mail Code IC-4
Houston, TX 77058

Patent Counsel
Mail Code AL3
Houston, TX 77058

John F. Kennedy Space Center
Technology Utilization Officer
Mail Stop PT-PMO-A
Kennedy Space Center, FL 32899

Patent Counsel
Mail Code PT-PAT
Kennedy Space Center, FL 32899

Langley Research Center
Technology Utilization Officer
Mail Stop 143
Hampton, VA 23665

Patent Counsel
Mail Code 279
Hampton, VA 23665

Lewis Research Center
Technology Utilization Officer
Mail Stop 7-3
21000 Brookpark Road
Cleveland, OH 44135

Patent Counsel
Mail Code LE-LAW
21000 Brookpark Road
Cleveland, OH 44135

Jet Propulsion Laboratory
Technology Utilization Officer
Mail Stop 156-211
4800 Oak Grove Drive
Pasadena, CA 91109

NASA Resident Office-JPL
Technology Utilization Officer
Mail Stop 180-801
4800 Oak Grove Drive
Pasadena, CA 91109

Patent Counsel
Mail Code 180-801
4800 Oak Grove Drive
Pasadena, CA 91109

George C. Marshall Space Flight Center
Technology Utilization Officer
Code AT01
Marshall Space Flight Center,
AL 35812

Patent Counsel
Mail Code CC01
Marshall Space Flight Center,
AL 35812

John C. Stennis Space Center
Technology Utilization Officer
Code HA-30
Stennis Space Center, MS 39529

NASA Headquarters
Technology Utilization Officer
Code CU
Washington, DC 20546

Assistant General Counsel for Patent Matters
Code GP
Washington, DC 20546

Dryden Flight Research Center
Technology Utilization Officer
M/S D21-31
Bldg. 4832 Whess 7
Lily Dr.
Edwards, CA 93523

BLANK PAGE



4 Electronic Components and Circuits



12 Electronic Systems



18 Physical Sciences



28 Materials



32 Computer Programs



36 Mechanics



40 Machinery



42 Fabrication Technology



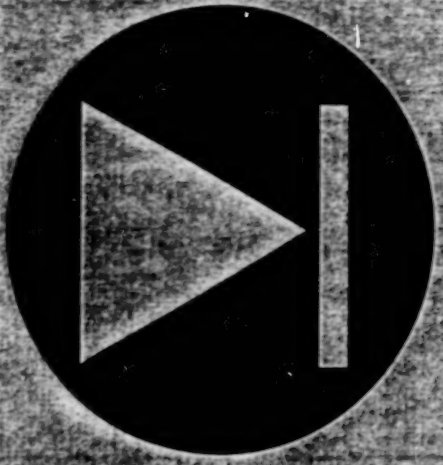
46 Mathematics and Information Sciences



50 Life Sciences



This document was prepared under the sponsorship of the National Aeronautics and Space Administration. Neither the United States Government nor any person acting on behalf of the United States Government assumes any liability resulting from the use of the information contained in this document, or warrants that such use will be free from privately owned rights.



Electronic Components and Circuits

Hardware, Techniques, and Processes

- 5 Instrument Records Magnetic Fields Generated by Lightning
- 6 Tunnel-Junction Mixers Perform Well at 205 GHz
- 7 Noise-Reduction Circuit for Imaging Photodetectors
- 8 Measuring Speed of Rotation With Two Brushless Resolvers
- 8 Wavelength Division Multiplexing With Integrated Optics
- 10 Phased-Array Antenna With Optoelectronic Control Circuits

Instrument Records Magnetic Fields Generated by Lightning

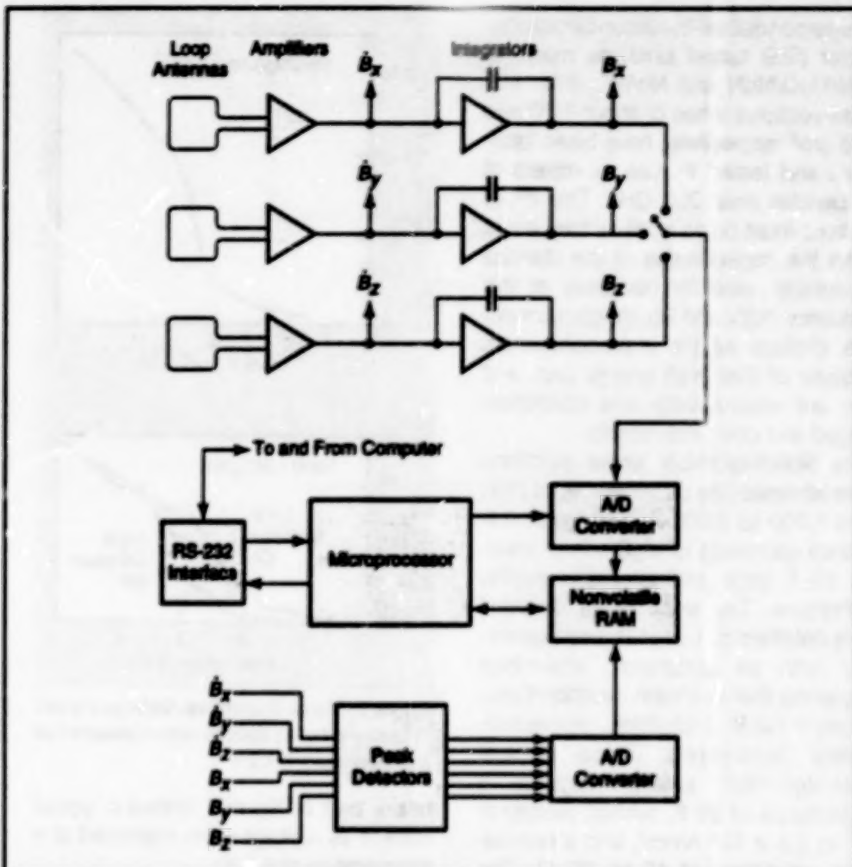
Measurements aid in assessment of potential for damage to sensitive equipment.

John F. Kennedy Space Center,
Florida

A portable, self-contained, compact instrument measures and records transient magnetic fields — particularly those generated by nearby lightning strikes. The instrument is designed to be placed near sensitive electronic equipment in anticipation of thunderstorms. The data recorded by the instrument during thunderstorms can be analyzed afterward to determine whether the magnetic effects of the lightning were strong enough that they might have damaged and/or affected the operation of the sensitive equipment. Thus, the instrument provides data that help engineers decide whether the sensitive equipment should be tested for damage and/or other effects caused by lightning. Typical installations in which this instrument could prove beneficial include outdoor sensing equipment, computer rooms, broadcasting stations, and powerplant control rooms.

The instrument (see figure) includes three orthogonal loop antennas, each of which senses the component of the transient magnetic field along one of three orthogonal axes. It is necessary to sense all three components because there is no way to know the direction of arrival of the magnetic field in advance. The three loops are placed far enough from each other to minimize cross-coupling among them. The output voltage of each loop antenna is proportional to the rate of change of one component of the magnetic field (\dot{B}_x , \dot{B}_y , or \dot{B}_z). This voltage is sampled; it is also processed through an integrator circuit to obtain a voltage proportional to the component of the magnetic field (B_x , B_y , or B_z).

An internal microprocessor controls the operation of the instrument. An analog-to-digital (A/D) converter, acting in conjunction with the microprocessor, samples the peak values of the magnetic field and the rate of change of the magnetic field during sampling periods 1 ms long. When the peak values exceed predefined thresholds, the peak values are stored in an electronic random-access memory (RAM) for subsequent retrieval. An additional A/D converter samples the output of one of the integrators (that is, it samples a signal proportional to one chosen component of the magnetic field) at a rate of 10^7 sam-



Three Loop Antennas sense the three orthogonal components of the rate of change of magnetic-flux density. These components and their time integrals (proportional to the magnetic field) are sampled and recorded for subsequent analysis.

ples per second. The instrument is equipped with a clock, so that the time when each sample is taken is recorded along with the sample. The time record makes it possible to correlate these samples with samples taken by other instruments during the same lightning strike.

The instrument is powered by batteries; it can operate unattended for as long as two weeks. The RAM is nonvolatile, so that the recorded data are not lost in the event of a loss of power. Stored data are retrieved from the instrument by use of a portable computer. The batteries can be changed in the field so the instrument can stay in place to continue measuring without interruptions. The data retrieved include the date and time of each occurrence, the peak positive and negative values of both the magnetic field and rate of change of its derivative (for all three axes), and a string of samples representing a 50- μ s-long waveform of the chosen

component of the magnetic field.

With its 10-MHz sampling rate, this instrument records lightning waveforms more accurately than do portable commercial magnetic-field meters. Lightning waveforms typically include frequencies up to tens of megahertz, while the commercial meters, which are designed to measure magnetic fields of high-voltage power lines, are usually limited in frequency response to a few hundred hertz.

This work was done by Pedro J. Medellin and Howard James Simpson of I-NET, Inc., for Kennedy Space Center. Further information is contained in a TSP [see page 1].

Inquiries concerning rights for the commercial use of this invention should be addressed to the Patent Counsel, Kennedy Space Center [see page 1]. Refer to KSC-11769.

Tunnel-Junction Mixers Perform Well at 205 GHz

NbN/MgO/NbN and NbN/AIO_x/Nb junctions have been tested.

Superconductor-Insulator-Superconductor (SIS) tunnel junctions made of NbN/MgO/NbN and NbN/AIO_x/Nb, with cross-sectional areas of about 0.30 and 0.25 μm^2 respectively, have been fabricated and tested for use as mixers at frequencies near 205 GHz. The cross sections must be as small as they are to make the capacitances of the devices acceptably small for operation at this frequency. NbN and Nb are good materials choices as the superconductors because of their high energy gap, and they are mechanically and electrically rugged and chemically stable.

The NbN/MgO/NbN tunnel junctions were fabricated by dc sputtering of NbN films 1,500 to 2,000 Å thick, radio-frequency sputtering of MgO tunnel barriers 10 Å thick, and photolithographic techniques. The small cross sections were obtained by use of an edge geometry (with an associated fabrication sequence) that has been described previously in *NASA Tech Briefs*. Some estimated parameters of a typical NbN/MgO/NbN junction include a capacitance of 28 fF, current density of 10^4 to 2.5×10^4 A/cm², and a normal-state resistance of 40 to 70 Ω. The

NASA's Jet Propulsion Laboratory, Pasadena, California

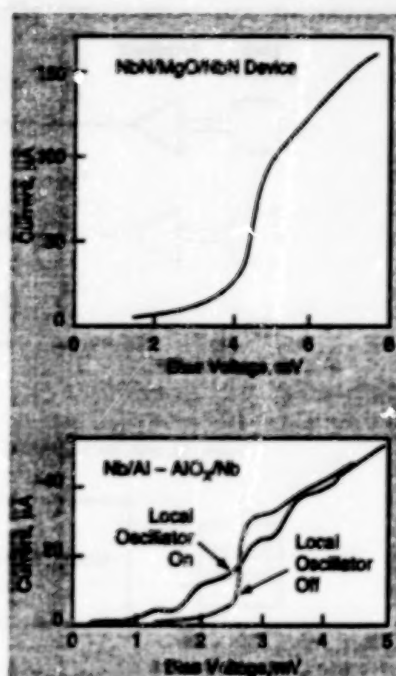


Figure 1. These Current vs.-Voltage curves of tunnel-junction devices were measured at a temperature of 4.2 K.

upper part of Figure 1 shows a typical current-vs.-voltage curve measured at a temperature of 4.2 K.

The Nb/AIO_x/Nb junctions were fabricated by dc sputtering of Nb films 2,000 to 3,000 Å thick, formation of an AIO_x barrier 10 to 20 Å thick, electron-beam lithography to define the junctions, and conventional photolithography to make the junction leads and the associated radio-frequency-filter structure. Estimated parameters of a typical junction of this type include capacitance of 15 fF, current density of 10^4 A/cm², and normal-state resistance of 80 to 100 Ω. The lower part of the figure shows a typical current-vs.-voltage curve measured at 4.2 K; the width of the quasi-particle current rise in this case is 0.3 mV, which is less than $hf/e = 0.85$ mV at 205 GHz (where h is Planck's constant, f is the frequency, and e is the fundamental unit of electrical charge).

Figure 2 is a block diagram of the specially designed cryogenic system used to test the devices as mixers. Each device to be tested was placed in a waveguide mount with an adjustable backshort and electric-field-plane tuner. "Hot" (300 K) and "cold" (77 K) loads were placed in the beam at the radio-frequency input port of the cryostat to provide a source temperature, T_s . A

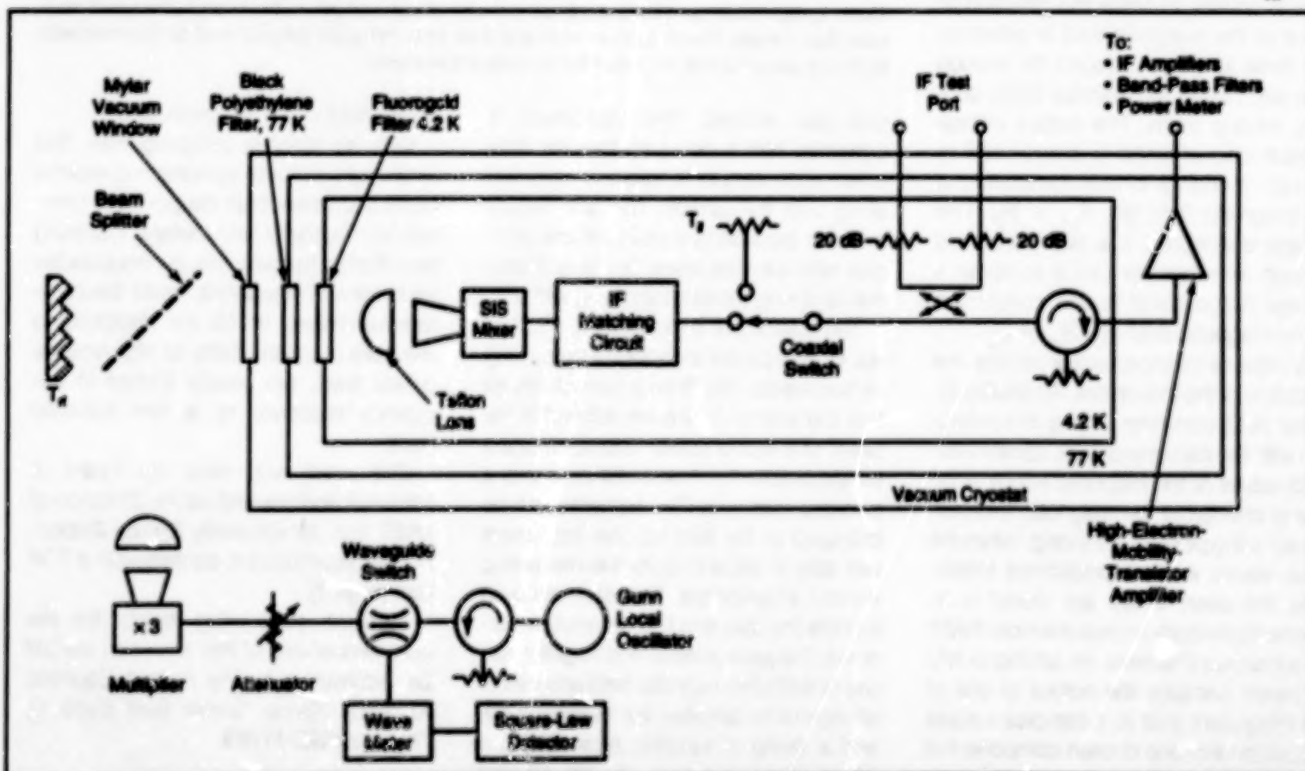


Figure 2. The performance of Tunnel-Junction Devices as mixers was measured at about 205 GHz in this specially designed cryogenic rf system.

specially designed variable temperature load was used to determine the temperature T_g at the output of the intermediate-frequency (IF) matching transformer of the mixer. A bidirectional coupler was used to measure the return loss of the mixer at an IF of 1.4 GHz. Analysis of the T_g -vs.- T_g data yielded the gain and noise of the mixer to an accuracy of ± 10 percent. The gain thus computed was corrected for the IF mismatch to obtain the available gain.

Devices of both types performed well. The Nb devices exhibited a noise temperature of 60 K (SSB), which is the best ever reported for such a mixer near 200 GHz. Other parameters of Nb devices include a sideband ratio of 19 dB, an IF return loss of -7.6 dB, and an available gain of -2.0 dB, which suggests good coupling of the rf signal.

The NbN devices exhibited a noise temperature of 145 K (DSB), which is comparable to that of prior NbN junc-

tions with integrated tuning elements. However, the gain of the NbN devices was very low (-10.7 dB), suggesting that the radio-frequency matching of this device may not have been optimal.

This work was done by Hamid H. S. Javadi, William R. McGrath, Scott R. Cypher, Bruce Bumble, Henry G. LeDuc, and Brian D. Hunt of Caltech for NASA's Jet Propulsion Laboratory. Further information is contained in a TSP [see page 1]. NPO-18419

Noise-Reduction Circuit for Imaging Photodetectors

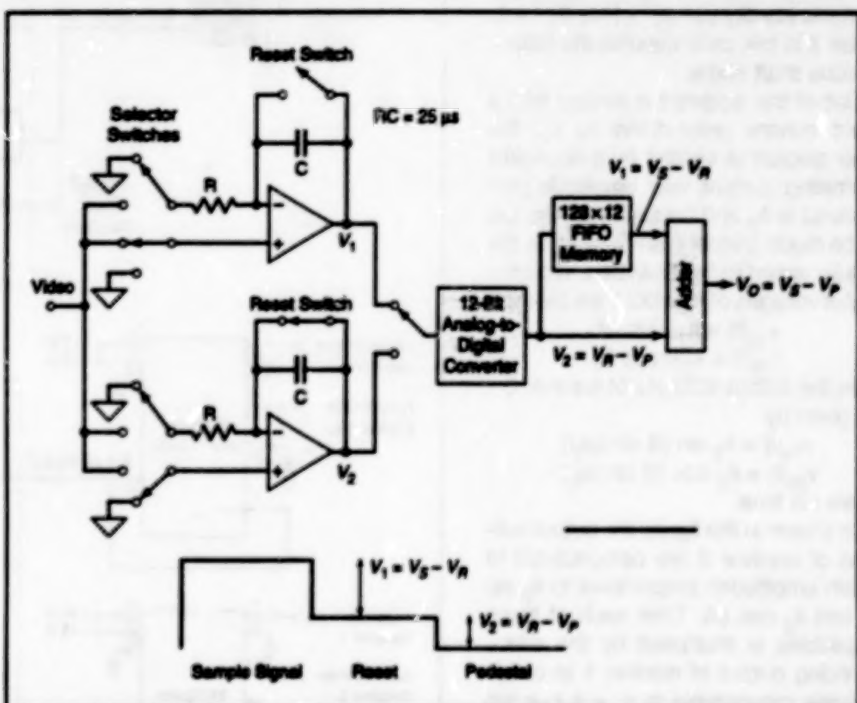
Correlated triple sampling eliminates reset noise and reduces 1/f noise.

A developmental correlated-triple-sampling circuit would suppress capacitor reset noise and attenuate low frequency noise in integrated-and-sampled circuits of multiplexed photodiode arrays. The noise reduction circuit is part of the Visible and Infrared Mapping Spectrometer (VIMS) instrument to be flown aboard the Cassini spacecraft to explore Saturn and its moons. Modified versions of the circuit might also be useful for reducing noise in terrestrial photo-sensor instruments.

The circuit is designed to eliminate the component of noise caused by resetting the voltage on a charge-integrating-and-sampling capacitor after taking each sample. This component is proportional to kTC , where k is Boltzmann's constant, T is the absolute temperature, and C is the integrating capacitance. The circuit is also designed to suppress a component of noise proportional to $1/f$ (where f = frequency) contributed during the times between integrations of photocharges.

The photodiode arrays are interfaced electrically with the signal processing electronics (SPE) which provide the appropriate bias voltages and control signals necessary to operate the array. The signal processing electronics includes a preamplifier, a clamp circuit, a gain-controlled amplifier that conditions the video signal for conversion from analog to 12-bit digital, and the correlated-triple-sampling circuit. The timing and control logic in the SPE command the photodiodes to provide three signal levels [(1) integrated video signal, V_S ; (2) reset level, V_R ; and (3) pedestal level due to switch feedthrough, V_P] to be of the same duration (25 μ s).

NASA's Jet Propulsion Laboratory, Pasadena, California



The Correlated-Triple-Sampling Circuit produces an output signal equal to $V_g - V_R$ from the present video frame period plus $V_R - V_P$ from the previous video frame period; the sum is nominally equal to the present value of $V_g - V_P$.

The correlated-triple-sampling circuit (see figure) contains an analog subtractor/integrator, an analog-to-digital converter, and a first-in/first-out (FIFO) memory. The difference between the digitized reset and pedestal voltages, $V_2 = V_R - V_P$, is stored in the FIFO memory for one video frame time. The difference between the digitized video signal and the reset voltages, $V_1 = V_g - V_R$, is then summed with V_2 in real time to obtain the correlated output voltage. In principle, the three video voltages could be digitized and processed (subtracting, storing, and adding) digitally. In practice,

this cannot be done in the initial intended application because the additional digital circuitry needed to accomplish all-digital processing would cause an unacceptable large increase in the overall size and mass of the spectrometer.

This work was done by Luis J. Ramirez, Bedabrata Pain, Craig Stoller, and Roger W. Hickok of Caltech for NASA's Jet Propulsion Laboratory. Further information is contained in a TSP [see page 1]. NPO-18897

Measuring Speed of Rotation With Two Brushless Resolvers

The measurement principle exploits a simple trigonometric identity.

Marshall Space Flight Center,
Alabama

The speed of rotation of a shaft can be measured by use of two brushless shaft-angle resolvers aligned so that they are electrically and mechanically in phase with each other. In some older tachometer systems, speeds of rotation are determined by electronically differentiating shaft-angle signals with respect to time. Unfortunately, electronic differentiation introduces noise. The present system does not rely on differentiation; instead, it involves electronic multiplication and addition, and exploits the trigonometric identity $[\sin \theta]^2 + [\cos \theta]^2 = 1$, where θ in this case denotes the instantaneous shaft angle.

One of the resolvers is excited with a direct current proportional to k_1 ; the other resolver is excited by a sinusoidal alternating current with amplitude proportional to k_2 and frequency $\omega_2/2\pi$. Let ω_2 be much greater than ω , which is the angular speed to be measured. Then the output voltages of resolver 1 are given by

$$v_{1A}(t) = k_1 \omega \sin(\theta)$$

$$v_{1B}(t) = k_1 \omega \cos(\theta)$$

while the output voltages of resolver 2 are given by

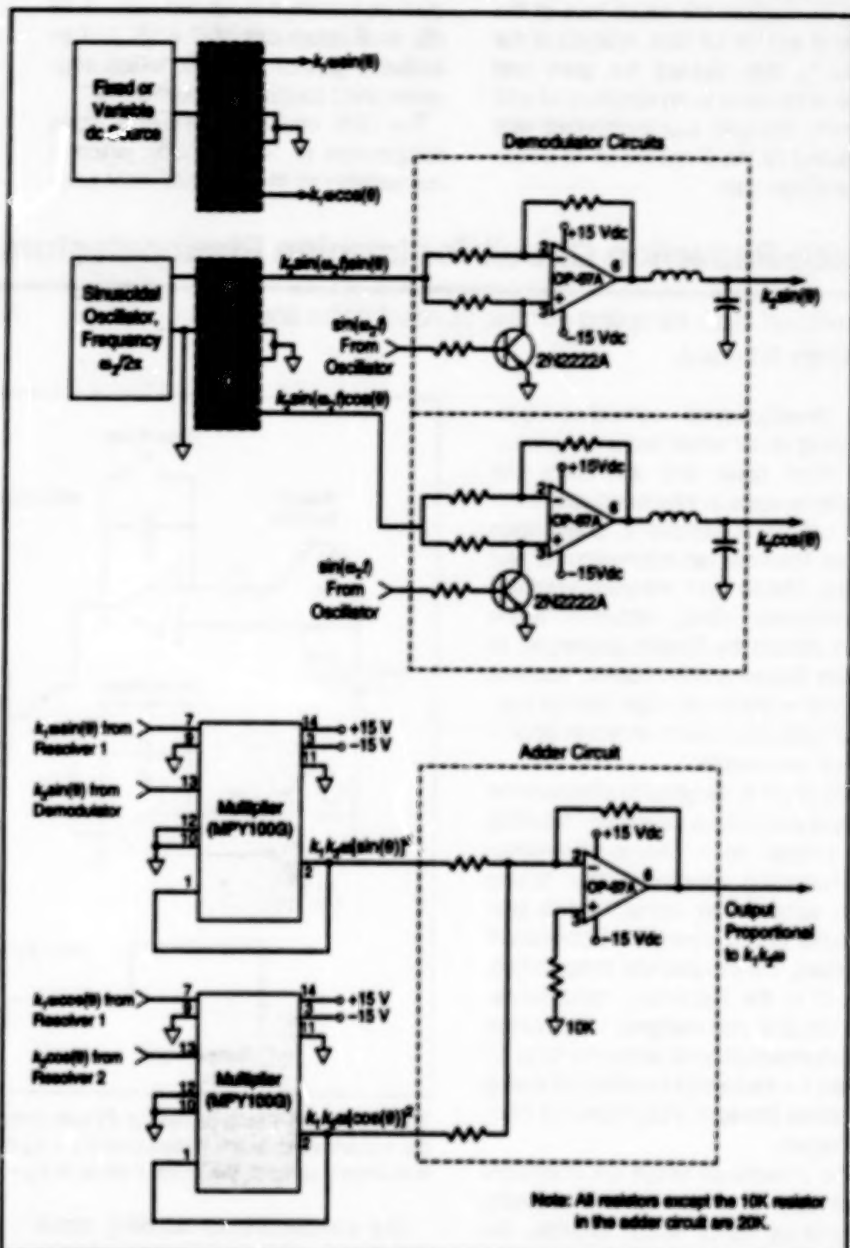
$$v_{2A}(t) = k_2 \sin(\theta) \sin(\omega_2 t)$$

$$v_{2B}(t) = k_2 \cos(\theta) \sin(\omega_2 t)$$

where t is time.

As shown in the figure, the output voltages of resolver 2 are demodulated to obtain amplitudes proportional to $k_2 \sin(\theta)$ and $k_2 \cos(\theta)$. Then each of these amplitudes is multiplied by the corresponding output of resolver 1 to obtain voltages proportional to $v_A = k_1 k_2 \omega [\sin(\theta)]^2$ and $v_B = k_1 k_2 \omega [\cos(\theta)]^2$. Then using the aforementioned trigonometric identity, these voltages are added to obtain an output voltage proportional to $k_1 k_2 \omega \theta$; that is, the output voltage is directly proportional to the speed to be measured. The dc excitation current can be adjusted to increase or decrease k_1 , and thereby increase or decrease the sensitivity of the measurement.

This work was done by David E. Howard of Marshall Space Flight



Note: All resistors except the 10K resistor in the adder circuit are 20K.

Two Brushless Shaft-Angle Resolvers and associated circuits generate a voltage proportional to the speed of rotation (ω) in both magnitude and sign.

Center. Further information is contained in a TSP [see page 1].

Inquiries concerning rights for the commercial use of this invention should

be addressed to the Patent Counsel, Marshall Space Flight Center [see page 1]. Refer to MFS-28793.

Wavelength Division Multiplexing With Integrated Optics

One integrated-circuit multiplexer/demultiplexer would communicate digital data at ≥40 Gb/s.

High-density wavelength-division-multiplexed optoelectronic integrated circuits

would be developed for use as transceivers in fiber-optic communica-

NASA's Jet Propulsion Laboratory, Pasadena, California

tions between computers, according to a proposal. The best wavelength-divi-

sion multiplexer available at present supports only four channels (at a data rate of 2 Gb/s each), and conventional time-division-multiplexing computer communication links introduce delays at the points of conversion between serial and parallel transmission. When fully developed, one of the proposed multiplexer/demultiplexer units would provide simultaneous communication on 32 wavelength channels at an overall data rate > 40 Gb/s, thereby (1) increasing the channel capacity and (2) simplifying the transmitting and receiving electronics and reducing the delay by eliminating the serial-to-parallel and parallel-to-serial "bottlenecks."

Development efforts are expected to focus on the integration of waveguide structures, surface and vertical diffraction gratings, lasers, photodetectors, and the associated signal-processing electronic circuits into monolithic devices in the InGaAs/InP material system. The devices would operate in the 1.3- and 1.55- μm wavelength bands. In a transmitter, the outputs of parallel integrated lasers, each at a different wavelength in the band, would be coupled into a single-mode optical fiber via a vertical diffraction grating. The multiple-wavelength beam entering a receiver from a single-mode optical fiber would be dispersed by a similar vertical diffraction grating into an array of parallel integrated positive/intrinsic/negative photodiodes—one photodiode for each wavelength (see Figure 1).

The vertical diffraction grating is so named because it would function similarly to a conventional diffraction grating oriented with its lines vertical with respect to devices illustrated in Figure 1. Two grating configurations would be investigated: a wide-band configuration for discrimination between 1.55 and 1.3 μm , and a narrow-band configuration for discrimination among closely spaced wavelengths in the 1.33- μm band.

Figure 2 is a schematic illustration of a proposed fiber optic-communication switch node. Wavelength-multiplexed inputs would enter the node from two fibers, then be separated into 1.3- μm and 1.55- μm bands by wide-band vertical diffraction gratings. Each 1.55- μm band, which contains a data channel, would be sent through a fiber-optic delay line to integrated control, routing, and signal-regeneration circuitry. Control channels in the 1.3- μm bands would be

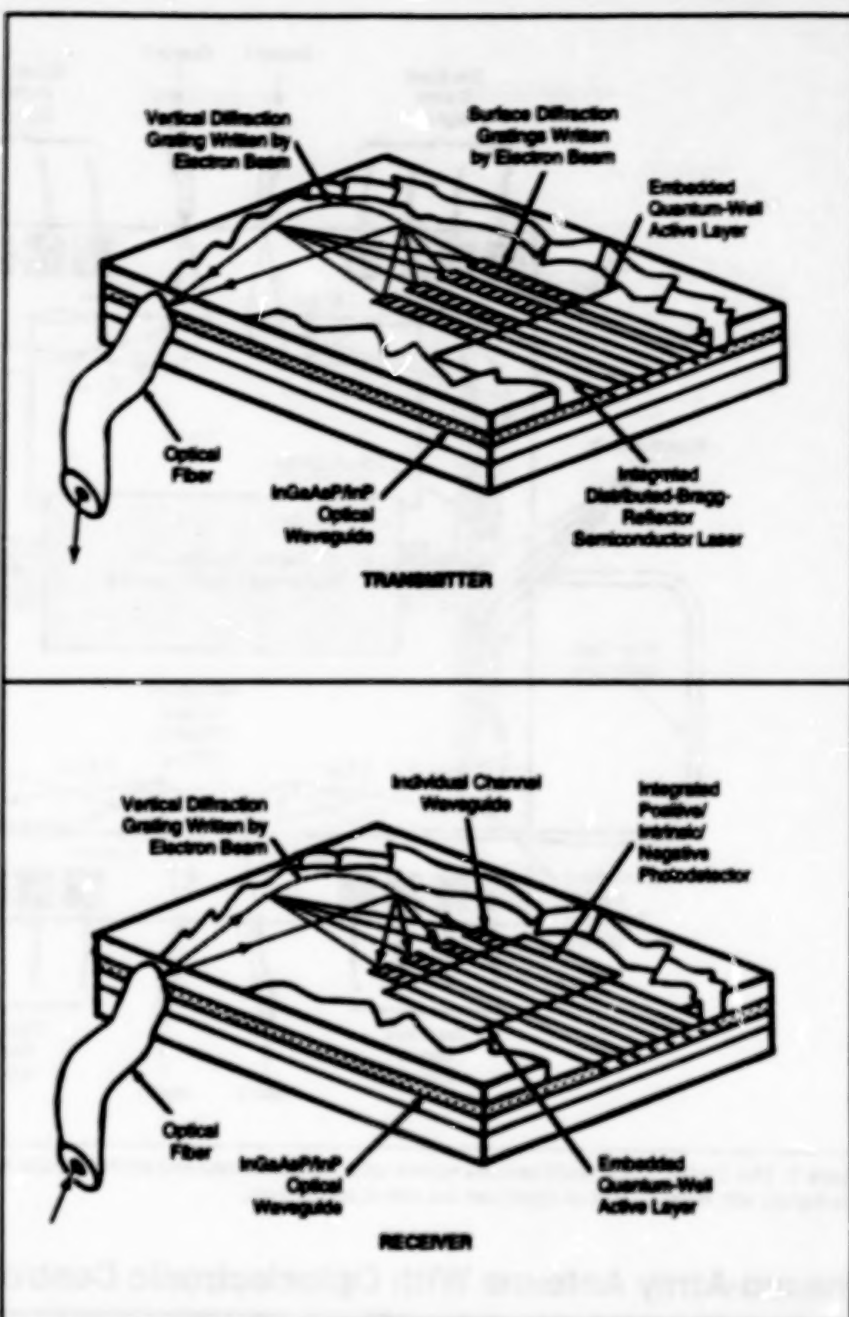


Figure 1. Single Chip Transmitters and Receivers would include arrays of integrated single-frequency semiconductor lasers (in transmitters) and integrated photodiodes (in receivers) coupled via integrated vertical diffraction gratings to single-mode optical fibers. Although only 4 lasers and 4 diodes are shown here the fully developed devices would contain 32 of each.

separated by narrow-band vertical diffraction gratings. The control signals would be detected and fed without delay to the control, routing, and signal-regeneration circuitry. Additional electronic control signals would be fed into and out of the node via electrical contacts. After processing the control and data signals, the node would recombine each data signal with modified control signals by wavelength-multiplexing onto one of the output optical fibers.

This work was done by Robert J. Lang and Siamek Forouhar of Caltech for NASA's Jet Propulsion Laboratory. Further information is contained in a TSP [see page 1].

Inquiries concerning rights for the commercial use of this invention should be addressed to the Patent Counsel, NASA Resident Office - JPL [see page 1]. Refer to NPO-18357.

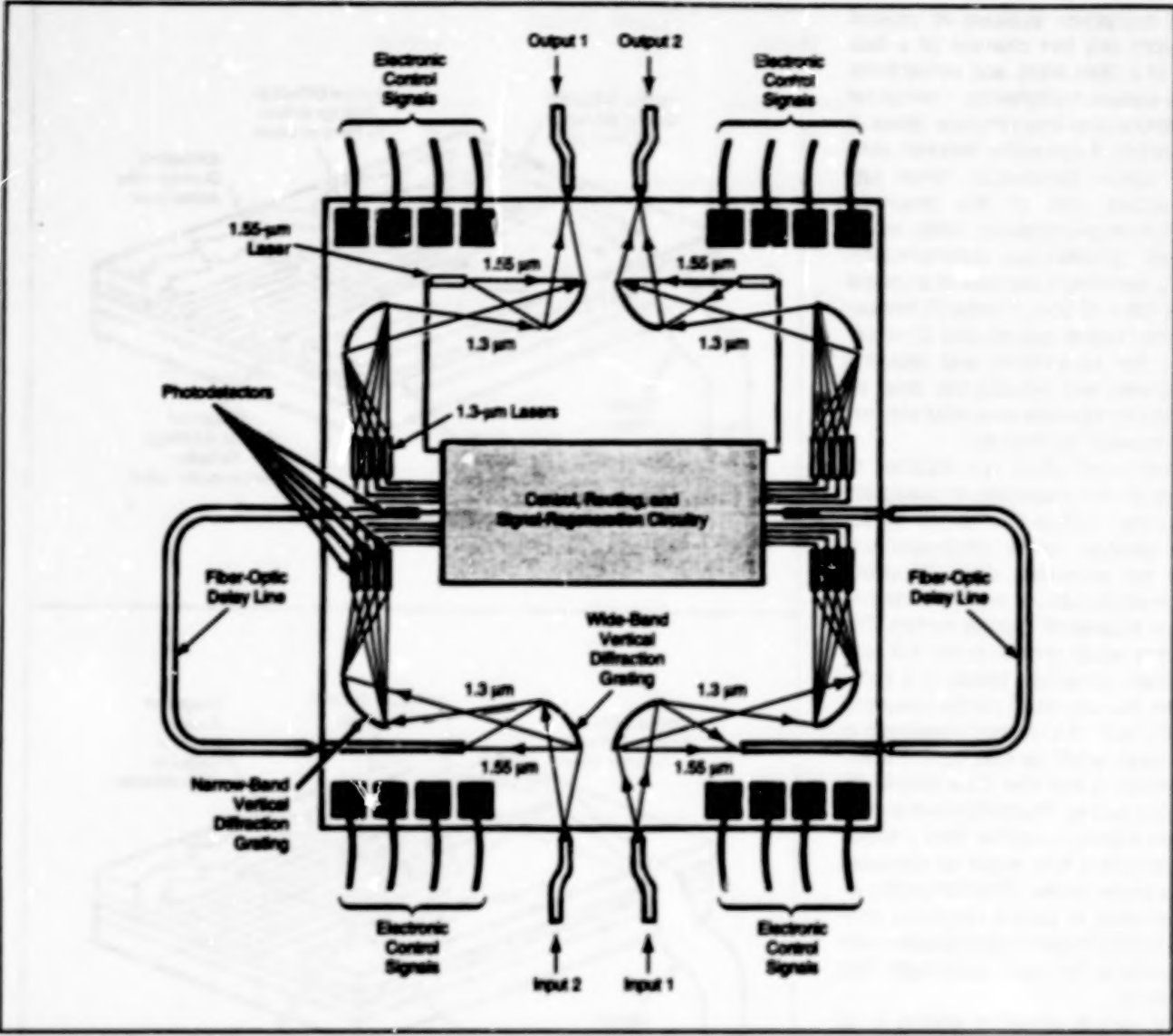


Figure 2. This Switch Node would process wavelength-multiplexed data and control signals from two input optical fibers and retransmit the data signals with modified control signals on two output optical fibers.

Phased-Array Antenna With Optoelectronic Control Circuits

Control signals are distributed via optical fibers.

Phased-array microwave antennas in which phase- and amplitude-controlling signals are distributed to the radiating elements via optical fibers are undergoing development. A four-element, Ka-band (27 to 40 GHz) prototype was expected to be completed shortly after this article was written.

Phased-array antennas that contain individually controllable elements offer

Lewis Research Center,
Cleveland, Ohio

the advantages of flexible, rapid electronic steering and shaping of beams. Furthermore, the greater the number of elements, the less the overall performance of an antenna is degraded by a malfunction in a single element. In an antenna of the type being developed, the Ka-band radio-frequency power is distributed to each element by a power divider (basically a transmission-line net-

work). The phase and amplitude of the signal radiated by each element are controlled by a monolithic microwave integrated circuit (MMIC), which includes a multiple-bit digitally controlled variable-gain amplifier and variable phase shifter.

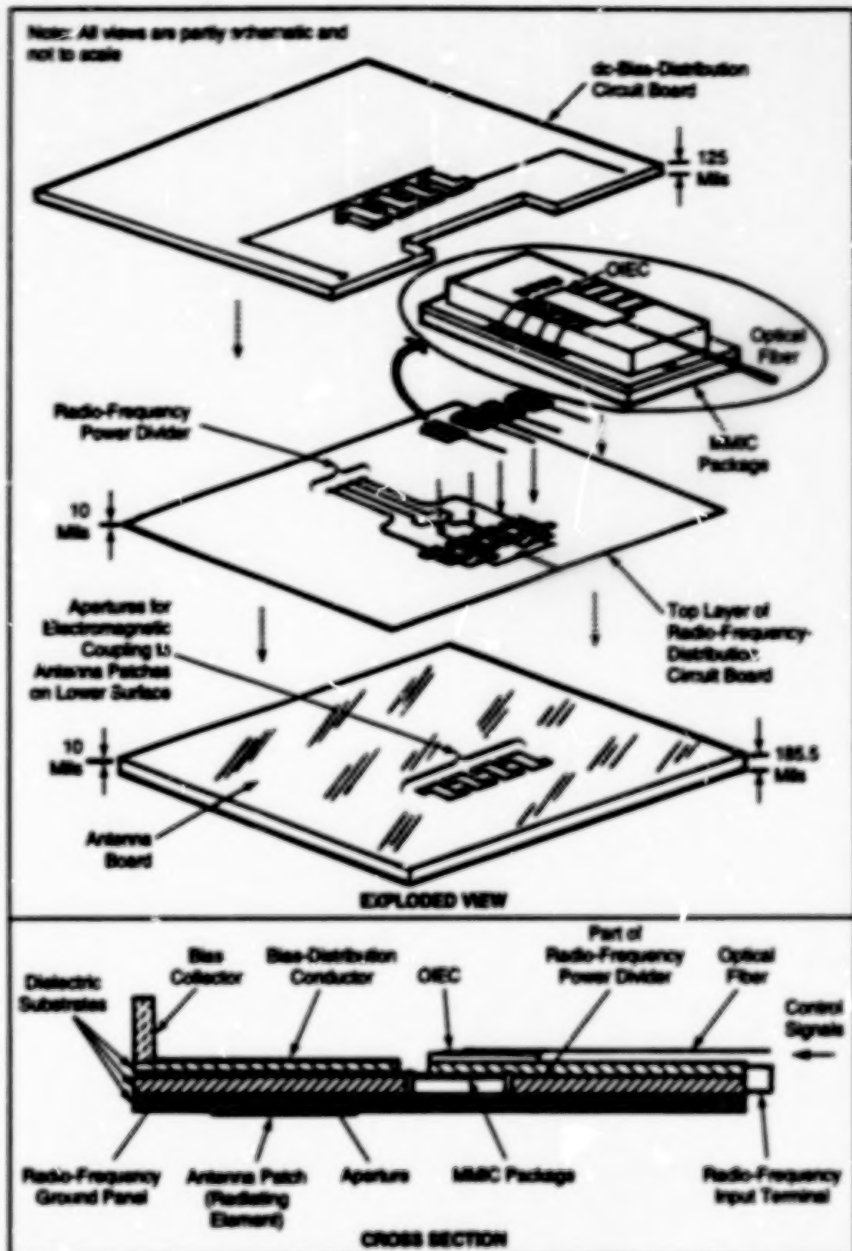
Ten or more control signals are needed for each element. Optical fibers are well suited to the distribution of the

many control signals in the limited space available on a typical array because they are relatively small and invulnerable to crosstalk. They also offer advantages of lightweight and mechanical flexibility.

The prototype four-element antenna is structured in layers (see figure). The topmost layer is a circuit board that distributes dc bias and serves as a structural support. The next lower layer is a circuit board with the radio-frequency power divider on its upper surface and the radio-frequency-ground plane on its lower surface. The digital control signals are transmitted serially on optical fibers to monolithic optoelectronic interface circuits (OEICs), which convert the signals to parallel format compatible with the MMICs. Each OEIC is adhesively bonded to the associated MMIC package and electrically connected via wires to the MMIC and to the dc-bias-distribution circuit board.

The radio-frequency output of each MMIC is coupled electromagnetically, through an aperture in the radio-frequency-ground plane, to an antenna patch (the associated radiating element) on the bottom surface of the structure. Such electromagnetic coupling is very efficient and eliminates the need for direct electrical coupling between the power-divider/MMIC layer and the antenna-patch layer.

This work was done by Richard R. Kunath, Kurt A. Shalkauskas, Konstantinos Martzaklis, Richard Q. Lee, and Alan N. Downey of Lewis Research Center and Raines N. Simons of Sverdrup Technology, Inc. Further information is contained in a TSP [see page 1].
LEW-15391



The Prototype Phased-Array Antenna features control of amplitude and phase at each radiating element. The amplitude- and phase-control signals are transmitted on an optical fiber to an OEC, then to an MMIC at each element.



Electronic Systems

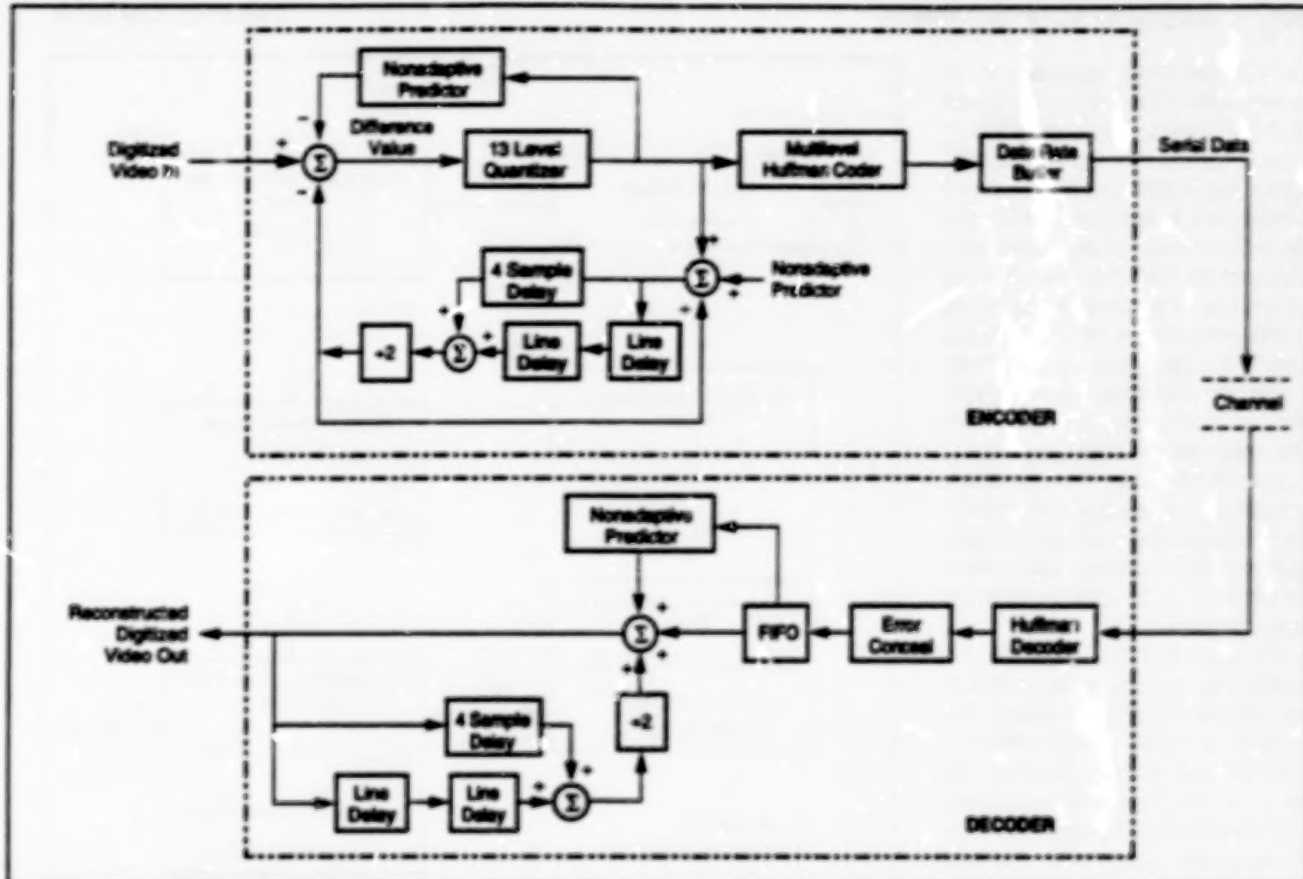
Hardware, Techniques, and Processes

- 13 Real-Time Compression of Digital Video
- 14 Controlled-Root Approach to Digital Phase-Locked Loops
- 15 Remote Neural Pendants in a Welding-Control System
- 15 Tilt/Integral/Derivative Compensators for Controllers
- 16 Ambient-Light Simulator for Testing Cockpit Displays

Real-Time Compression of Digital Video

Images are reconstructed without noticeable degradation.

Lewis Research Center, Cleveland, Ohio



The Enhanced DPCM Video Compression Algorithm utilizes a nonuniform quantizer, nonadaptive predictor, and multilevel Huffman coder to substantially reduce the data rate below that achievable with conventional DPCM.

A digital video compression algorithm was developed to process 8-bit samples of composite color NTSC video signals taken at four times the color subcarrier frequency. After compression, the amount of digital data required for video transmission is reduced by over 75 percent without noticeable degradation in the quality of the picture.

The algorithm is based on differential pulse code modulation (DPCM), a predictive compression technique where the anticipated value (prediction) of an incoming pixel is subtracted from the actual value. This difference is then assigned to a level from a limited set of quantization groups. For this implementation, all predictions of an incoming pixel are done on an intrafield basis to eliminate motion degradation and minimize the complexity of the processing circuits.

To improve on DPCM, the compression algorithm additionally utilizes a nonuniform quantizer, nonadaptive predictor, and multilevel Huffman coder. The nonuniform quantizer improves resolution of the reconstructed video, the

nonadaptive predictor increases edge preservation, and the multilevel Huffman coder provides additional data rate reduction.

Several issues must be resolved to transmit Huffman-coded digital video over a constant-rate serial channel. Two such issues are rate conversion (from variable to a fixed rate) and recovery from communication errors. An intelligent data rate buffer was implemented to perform the rate conversion, while also efficiently storing the compressed data and guarding against the memory underflow and overflow. An error concealment circuit was implemented to allow the decoder to mask and gracefully recover from bit errors.

A real-time system has been developed to implement the enhanced DPCM video compression algorithm. The hardware reduces the digital video information from 114 Mbps to 26 Mbps (approximately 1.8 bits per pixel). Quality of the reconstructed video is excellent with no motion degradation.

This work was done by Thomas P.

Bizon, Wayne A. Whyte, Jr., and Mary Jo Shalkauskas of Lewis Research Center and Vincent R. Marcopoli of Case Western Reserve University. Further information may be found in NASA TM-105616 (N92-19700/TB), "Real-Time Demonstration Hardware for Enhanced DPCM Video Compression Algorithm" and NASA TM-106032 (N93-22483/TB), "Real-Time Transmission of Digital Video Using Variable-Length Coding."

Copies may be purchased [prepayment required] from the NASA Center for AeroSpace Information, Lethbridge Heights, Maryland, Telephone No. (301) 621-0390. Rush orders may be placed for an extra fee by calling the same number.

This invention has been patented by NASA (U.S. Patent No. 5,057,917). Inquiries concerning nonexclusive or exclusive license for its commercial development should be addressed to the Patent Counsel, Lewis Research Center (see page 1). Refer to LEW-15866.

Controlled-Root Approach to Digital Phase-Locked Loops

Performance can be tailored more flexibly and directly to satisfy design requirements.

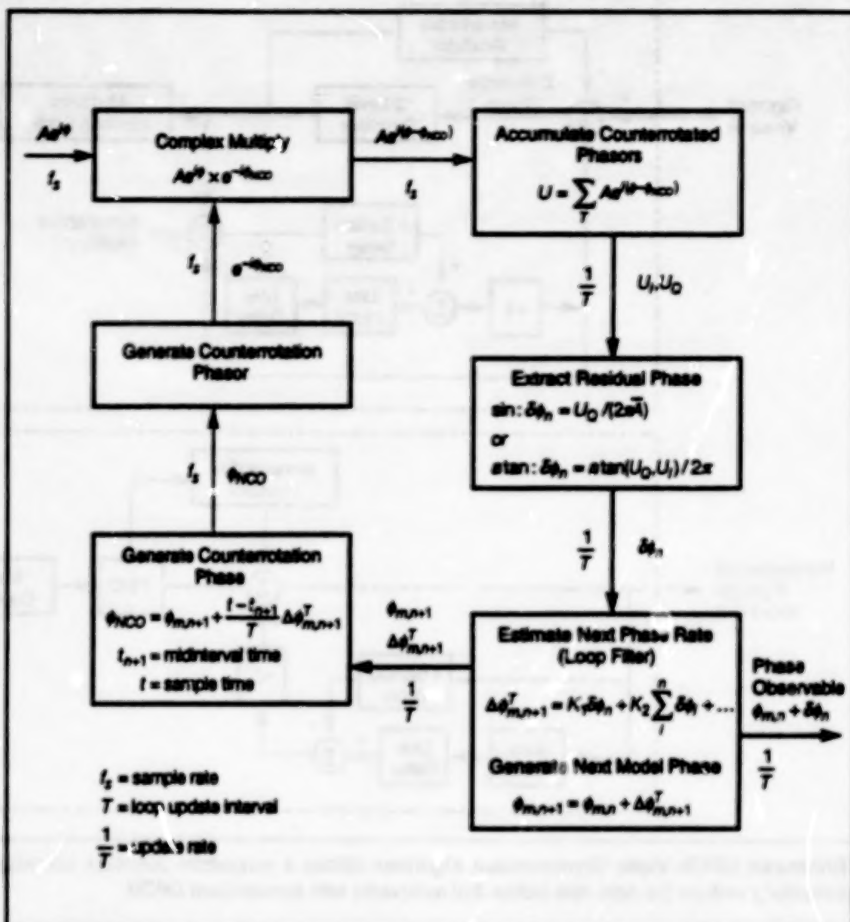
NASA's Jet Propulsion Laboratory,
Pasadena, California

The controlled-root approach is an improved method for analysis and design of digital phase-locked loops (DPLLs). Heretofore, DPLLs (see figure) have been designed and analyzed partly by reliance on analog-circuit traditions, which has made such analysis unnecessarily cumbersome. In contrast, the controlled-root approach has been developed rigorously from first principles for fully digital loops, making DPLL theory and design simpler and more straightforward (particularly for a third- or fourth-order DPLL) and controlling performance more accurately in the case of high gain. The formalism, which can be systematically extended to loops of arbitrary order, provides an easy flexibility by directly placing roots in the s-plane (where s is the Laplace-transform complex frequency).

In the controlled-root approach, the transient response and noise bandwidth of the loop can be selected directly. The roots of the transfer function of the loop are first placed in the s plane on the basis of a loop-bandwidth parameter and of root-specific damping and transient-decay-rate parameters. The loop constants are then calculated on the basis of these roots.

The controlled-root parameterization is made feasible by the fact that digital loops can usually be designed so that they do not suffer significantly from the effects of variation in gain. That is, variation in the amplitude of the signals, caused by either gain instability or changes in signal power, can usually be taken into account by use of a normalized phase extractor. A "fully digital" DPLL can be designed from this perspective, without the analysis or precautions that are needed in older design methods to cope with potential variation in gain.

Previous analyses have been begun with the closed-loop equation in the "continuous-update" (CU) limit in which $B_L T \rightarrow 0$, where B_L is the loop noise bandwidth and T is the loop update interval. For sufficiently small $B_L T$ (e.g., $B_L T \leq 0.02$), the CU approximation can provide an adequate starting point for analysis and design of loops via the controlled-root approach. In the continuous-update limit, loop constants for loops of first through fourth order have been obtained in closed form as a function of the afore-



A Phase-Locked Loop with phase and phase-rate updates and zero computation delay is illustrated schematically.

mentioned controlled-root-parameters. However, in the case of a "discrete-update" (DU) loop, for which $B_L T$ is assigned a larger value (e.g., $B_L T = 0.5$), the complexity of the equations necessitates a numerical solution. Numerical solutions have been obtained as a function of $B_L T$ for loops of first through fourth order with either phase-rate-only feedback or phase and phase-rate feedback, with supercritical damping or standard underdamping, and with zero computation delay or a computation delay equal to one update interval. With the controlled-root parameterization, the bandwidth and damping behavior of a high-order loop can be implemented simply and accurately, even when $B_L T$ is large.

Based on the controlled-root parameterization, loops of first through fourth order were simulated and characterized in terms of mean time to first cycle slip. The simulated loops have phase and

phase-rate feedback, supercritical damping and zero computation delay. For a given B_L , loops with larger $B_L T$ exhibited considerably better (longer) mean time to first cycle slip than did those of smaller $B_L T$. Performance of loops with respect to steady-state phase error has also been assessed. For a given value of B_L , steady-state phase error remains essentially constant for $B_L T \leq 0.02$, but increases at larger values of $B_L T$.

This work was done by Scott A. Stephens and J. Brooks Thomas of Caltech for NASA's Jet Propulsion Laboratory. Further information is contained in a TSP [see page 1].

This invention is owned by NASA, and a patent application has been filed. Inquiries concerning nonexclusive or exclusive license for its commercial development should be addressed to the Patent Counsel, NASA Resident Office-JPL [see page 1]. Refer to NPO-18757.

Remote Neural Pendants in a Welding-Control System

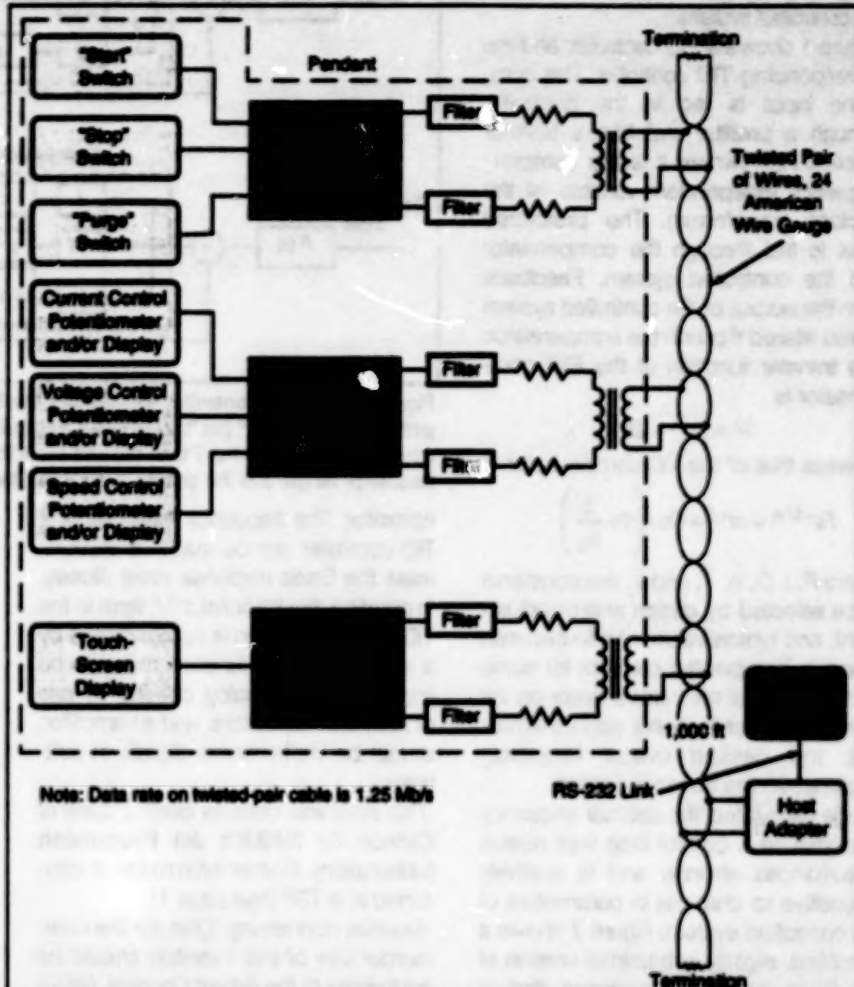
Neural-network circuits enhance functionality.

Marshall Space Flight Center, Alabama

Neural-network integrated circuits are used to increase the information capacities of remote terminals and of the communication links between those terminals and a host computer in the electronic control system of a large robotic welding facility. The neural-network integrated circuits enhance the functionalities of both the remote terminals (which are called "pendants" in the industry) and the communication links, without necessitating the installation of additional wires in the links. A neural-network integrated circuit makes it possible to incorporate many features into a pendant, including a real-time display of critical welding parameters and other process information, a capability for communication between a technician at the pendant and the host computer or a technician elsewhere in the system, and switches and potentiometers through which a technician at the pendant exerts remote control over such critical aspects of the welding process as current, voltage, rate of travel, flow of gas, starting, and stopping.

Heretofore, a separate microprocessor would probably have been needed for each of these features. Furthermore, communication links included double-shielded cables containing 50 twisted-wire pairs, which could handle only basic remote-control functions, and the addition of video displays in the electrically noisy welding environment was prohibitively expensive.

The pendants equipped with the neural-network integrated circuits are all transformer-coupled to a single twisted-pair cable, which thus constitutes the trunk line of a local-area network of neural-network terminals and the host computer (see figure). Each neural-network integrated circuit in a pendant is a commercial unit (Neuron 143150) that can handle as many as 11 input/output functions. Each display device (cathode-ray tube, liquid-crystal display, light-emitting diode, or meter) and each control switch in a pendant is connected to one of the input/out-



Neural-Network Integrated Circuits control the flow of information over a twisted-pair cable for communication with a host computer. Despite the high electromagnetic interference in a factory environment, the host computer can be positioned a large distance from the pendant.

put ports of its neural-network integrated circuit(s). The twisted-pair cable can be as long as 1,000 ft (about 300 m), and is connected to a host adapter that is, in turn, coupled to the host computer via standard equipment.

Other potential manufacturing applications of pendants and communication links like these could include control of spray coating and of curing of composite materials. Potential nonmanufacturing uses include remote control of heating, air

conditioning, and lighting in electrically noisy and otherwise hostile environments.

This work was done by Richard A. Venable and Joseph H. Bucher of Martin Marietta Corp. for Marshall Space Flight Center. No further documentation is available.

Inquiries concerning rights for the commercial use of this invention should be addressed to the Patent Counsel, Marshall Space Flight Center [see page 1]. Refer to MFS-26903.

Tilt/Integral/Derivative Compensators for Controllers

The responses of the controllers can be made to approximate the optimal responses more closely.

Tilt/integral/derivative compensators for tunable feedback control systems offer advantages over proportional/integral/deriva-

tive compensators, which until now have been the standard compensators in such controllers. In comparison with the propor-

NASA's Jet Propulsion Laboratory, Pasadena, California

tional/integral/derivative (PID) compensator that would otherwise be used in a given controller, a tilt/integral/derivative (TID)

compensator can be designed and adjusted more easily, and can be made to reject disturbances more strongly and be less sensitive to variations in the parameters of the controlled system.

Figure 1 shows a PID controller and the corresponding TID controller. The command input is fed to the controller through a prefilter that has a transfer function $R(s)$ (where s is the complex-frequency independent variable of the Laplace transforms). The prefiltered input is fed through the compensator into the controlled system. Feedback from the output of the controlled system is also filtered through the compensator. The transfer function of the PID compensator is

$$P + Is^{-1} + Ds$$

whereas that of the TID compensator is

$$Ts^{-1/n} + Is^{-1} + Ds \left(1 + \frac{s}{s_0} \right)$$

where P , I , D , n , T , and s_0 are constants to be selected by design and/or adjustment, and typical values of n lie between 2 and 3. The prefilter corrects for some of the effects of the compensator on the command input in such a way as to provide the desired overall frequency response to the command input.

Bode calculated the optimal frequency response of a control loop that rejects disturbances strongly and is relatively insensitive to changes in parameters of the controlled system. Figure 2 shows a simplified, slightly suboptimal version of the Bode frequency response that is adequate for industrial control, along with the frequency response of a PID

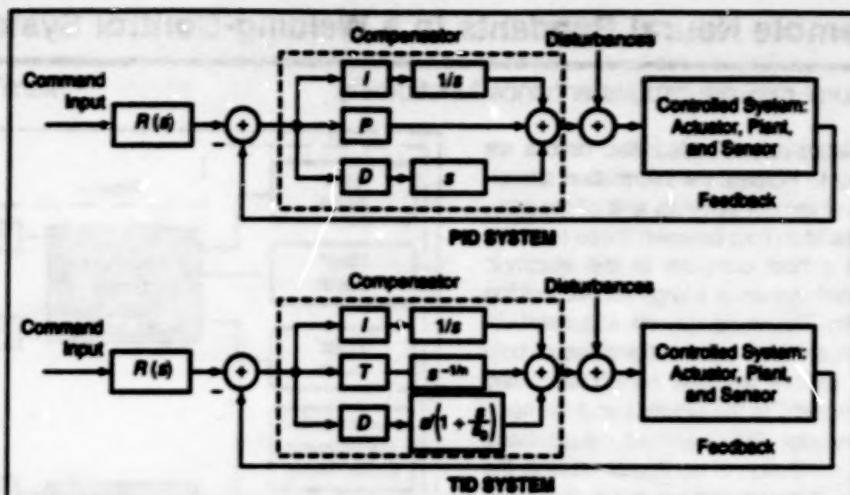


Figure 1. The TID Controller Resembles the PID Controller superficially, but offers better performance. The "T" (for "tilt") signifies a tilt in the gain-frequency response in the middle frequency range, where the T term dominates. In the PID controller, the P term dominates in this frequency range, and the gain-frequency plot there is horizontal.

controller. The frequency response of a TID controller can be made to approximate the Bode response more closely. In practice, the irrational $s^{-1/n}$ term in the TID transfer function is approximated by a rational transfer function that can be implemented in analog circuitry by use of resistors, capacitors, and an amplifier, or can be implemented digitally in software.

This work was done by Boris J. Lurie of Caltech for NASA's Jet Propulsion Laboratory. Further information is contained in a TSP [see page 1].

Inquiries concerning rights for the commercial use of this invention should be addressed to the Patent Counsel, NASA Resident Office - JPL [see page 1]. Refer to NPO-18492

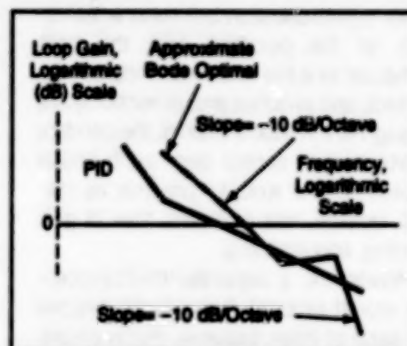


Figure 2. The Optimal Bode Response can be approximated in a TID controller by selection of the parameters of the TID transfer function.

Ambient-Light Simulator for Testing Cockpit Displays

A computer-controlled apparatus simulates sunlight, darkness, and lightning on demand.

An apparatus provides illumination from outside, through the windows and into the interior of a simulated airplane cockpit. The apparatus and cockpit are used to evaluate aircraft-instrumentation display devices under realistic lighting conditions.

The apparatus (see figure) simulates such diverse lighting conditions as direct sunlight shining onto the display surface through a side window or over the pilot's shoulder, sunlight reflecting from a white shirt onto the display surface, the Sun in the pilot's forward field of view at a low elevation angle over a deck of clouds, darkness, and lightning flashes in a dark



The Ambiant-Light Simulator surrounds the forward section of a simulated airplane. The simulator provides control over the intensity, color, and diffuseness of solar illumination and of the position of the Sun relative to the airplane.

*Langley Research Center,
Hampton, Virginia*

sky. Illuminance at the pilot's instrument panel can be controlled from darkness to over 10,000 foot-candles; luminance in the forward field of view can be controlled to as high as 18,000 foot-lamberts over a small area.

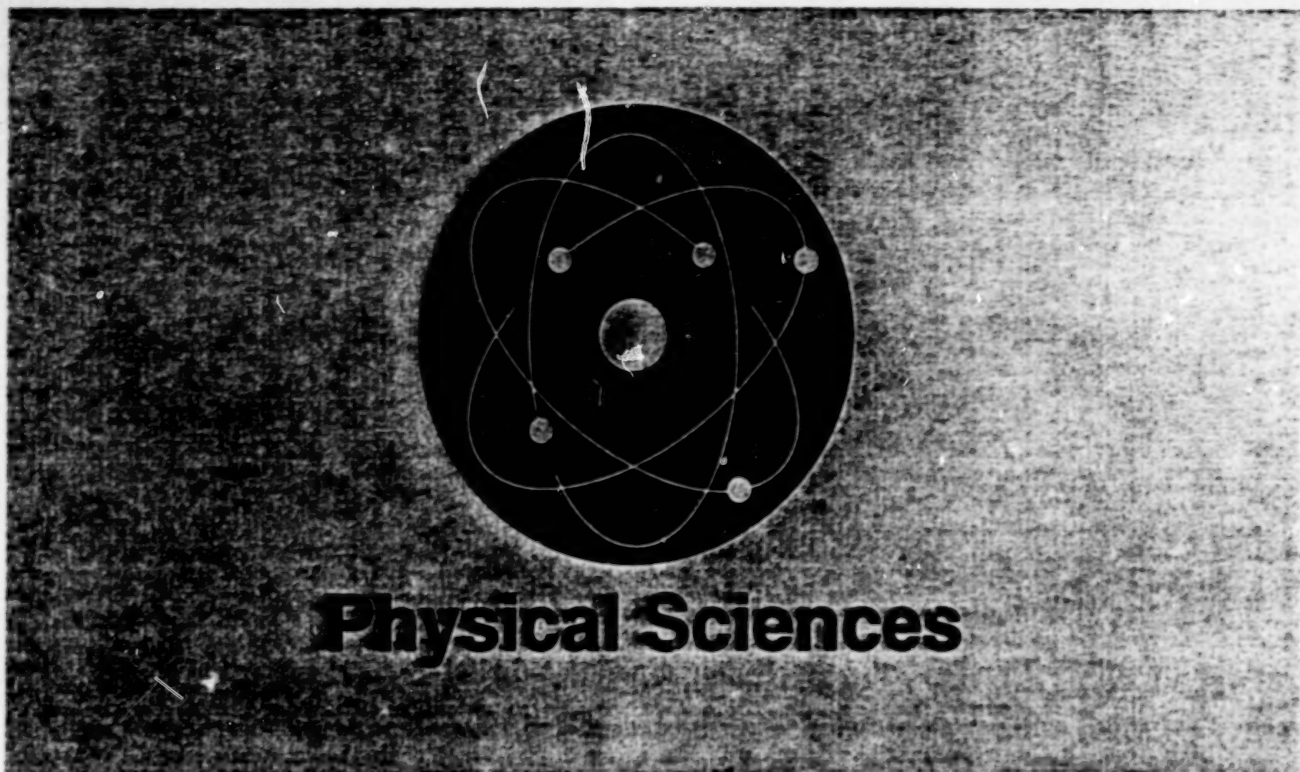
The apparatus includes a Sun simulator that comprises several movable sources of light with scrolling color filters and a diffusing cylinder. The apparatus also includes an array of stroboscopic lights of various powers, selectable to obtain multiple flashes of various intensities and durations to simulate a main lightning flash followed by a trailing sequence of flashes. The apparatus is

controlled by the same computer that hosts a software model of a modern transport aircraft represented in the simulated cockpit.

This work was done by Vernon M. Batson and Lawrence E. Gupton of

Langley Research Center. Further information may be found in AIAA paper 90-3146, "Design, Development, and Testing of an Ambient Lighting Simulator for External Illumination of a Transport Simulator Cockpit."

Copies may be purchased [prepayment required] from AEROPLUS, Burlingame, California 94010, Telephone No. (800) 682-2376, Fax No. (415) 259-5047.
LAR-14668



Hardware, Techniques, and Processes

- 19 Dual Telecentric Lens System for Projection Onto Tilted Toroidal Screen
- 20 Chromatic Image Analysis for Quantitative Thermal Mapping
- 20 Microsensor Hot-Film Anemometer
- 21 Two-Diffraction-Order, Beam-Splitting, Imaging Spectrometer
- 22 Electrostatic Separation of Layers in Thermal Insulation
- 23 Vapor Degreasing of a Large Tank
- 23 Measuring Thickness of Ice When Liquid Is Present
- 24 Improved Optics for Quasi-Elastic Light Scattering
- 25 Small-Modulation Ellipsometer
- 26 Real-Time, Holographic, Dynamic Image-Storage Device
- 27 Ultracold-Atom Accelerometers

Dual Telecentric Lens System for Projection Onto Tilted Toroidal Screen

One projection lens is optimized for the red and green spectral region; the other for the blue.

Lyndon B. Johnson Space Center,
Houston, Texas

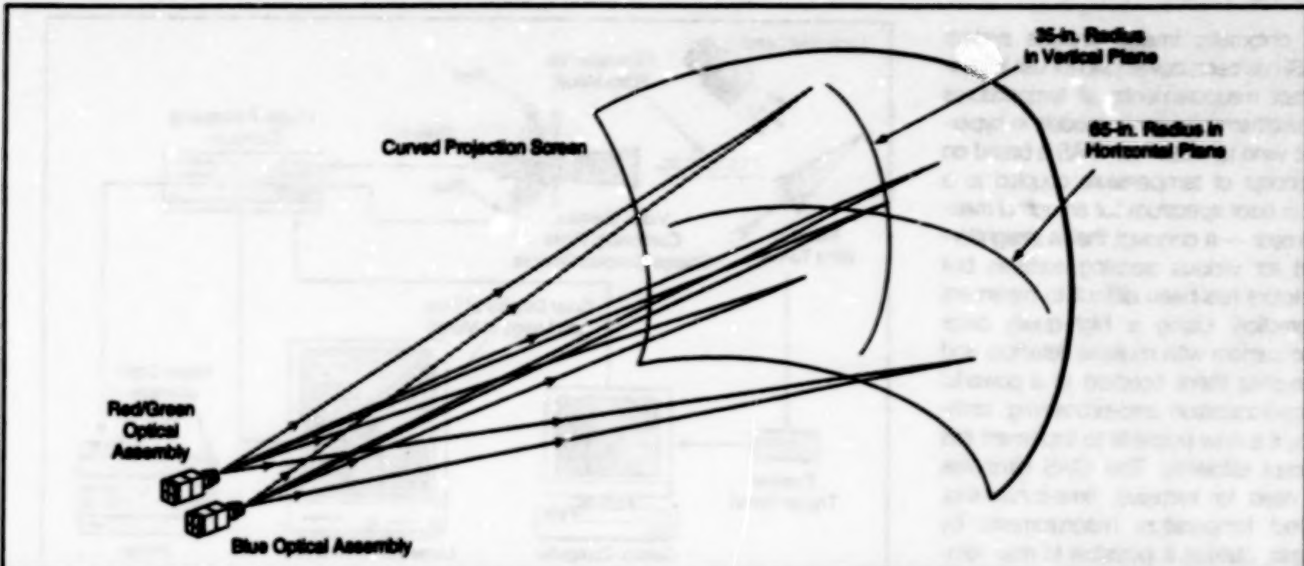


Figure 1. Two Different Spectral Components of the Same Image are projected onto a screen that is toroidally curved; its curvature in the horizontal plane differs from its curvature in the vertical plane. The screen is also tilted with respect to the optical axis of the red/green optical assembly.

Figure 1 shows a system of two optical assemblies for projecting an image onto a tilted toroidal screen. The system could be used in conjunction with any source of imagery but is designed especially to project images formed by reflection of light from a liquid-crystal light valve (LCLV).

The dual-channel approach is chosen because it offers several advantages which include: simplified color filtering, simplified chromatic aberration corrections, less complex polarizing prism arrangement, and increased throughput of blue light energy. However, the dual-channel approach introduces an off-axis projection geometry making correction of geometric distortion much more challenging. The design is optimized, as is customary, by selection of unique combinations of optical glasses and configurations of lens elements. The design of one optical assembly is optimized for red and green light, and this assembly is used to project only the red and green components of the image; the design of the other optical assembly is optimized for blue light, and this assembly is used to project only the blue component of the image. The separate color components of the image are superimposed on the screen to obtain a full color image with minimal chromatic aberration and minimal geometric distortion.

Figure 2 shows the ray trace layouts of the two telecentric optical assemblies. In each assembly, image light reflects from the LCLV, passes through a fluid-filled,

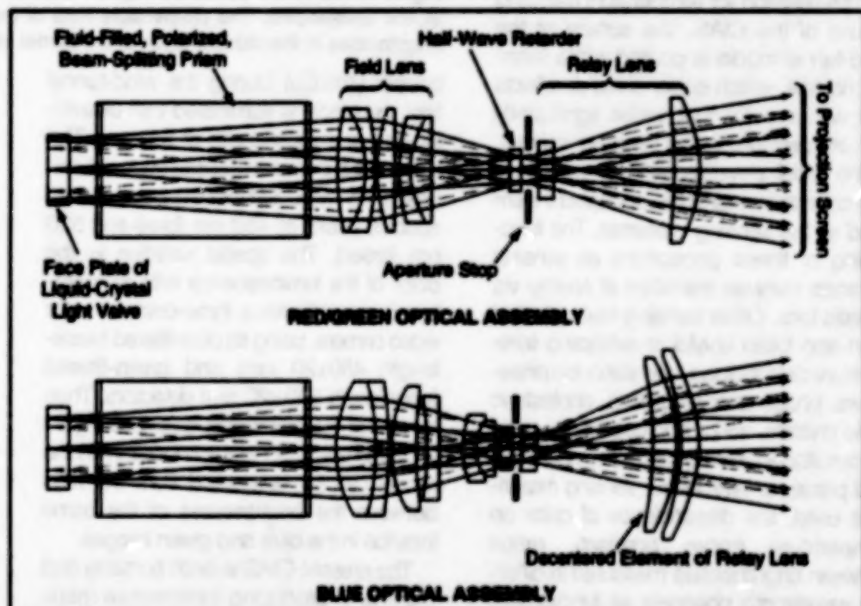


Figure 2. The Two Optical Assemblies have slightly different designs, each optimized for its region of the spectrum.

polarizing, beam-splitting prism, and is focused onto the tilted, curved screen by the projection lenses. An internal physical aperture stop helps to optimize performance. In the blue optical assembly, the projection lens includes an element that is decentered to compensate for the asymmetric aberrations which are induced by the off-axis geometry of the blue channel with respect to the optical axis of the red/green channel.

Each optical assembly includes a half-wave retarder for rotating the planes of

polarization when used with a polarization-sensitive viewing apparatus such as the pancake window (in-line-infinity-view optical system). The half-wave retarders are not needed for mere projection of an image on the screen.

This work was done by Ronald S. Gold and Russell M. Hudyme of Hughes Aircraft for Johnson Space Center. Further information is contained in a TSP [see page 1].
MSC-22443

Chromatic Image Analysis for Quantitative Thermal Mapping

Temperature maps are computed from various sensing surfaces using color image data.

Langley Research Center,
Hampton, Virginia

A chromatic image analysis system (CIAS) has been developed for use in non-contact measurements of temperatures on aerothermodynamic models in hypersonic wind tunnels. The CIAS is based on a concept of temperature coupled to a shift in color spectrum for an optical measurement — a concept that is straightforward for various sensing surfaces but heretofore has been difficult to implement in practice. Using a high-quality color video camera with multiple detectors and band-pass filters coupled to a powerful image-acquisition-and-processing computer, it is now possible to implement this concept efficiently. The CIAS eliminates the need for intrusive, time-consuming, contact temperature measurements by gauges, making it possible to map temperatures on complex surfaces in a timely manner and at reduced cost.

In preparation for temperature mapping by use of the CIAS, the surface of the wind-tunnel model is coated with a sensing material, which either emits or reflects light with a color that varies significantly with temperature in the range of interest. In the initial development of the CIAS, two-color thermographic phosphors were used as the sensing materials. The functioning of these phosphors as sensing materials involves transfers of energy via metallic ions. Other sensing materials that have also been useful in extracting temperature data include rare-earth-ion phosphors, phase-change paints, cholesteric liquid crystals, and a fluorescent dye used for simultaneous mapping of temperature and pressure. Whichever sensing material is used, the dependence of color on temperature (more precisely, ratios between brightnesses measured in different wavelength channels as functions of temperature) must be determined from calibration measurements on a similarly coated specimen at known temperatures.

Figure 1 illustrates the use of the CIAS in mapping the temperature on a model coated with a two-color thermographic phosphor made of zinc sulfide doped with

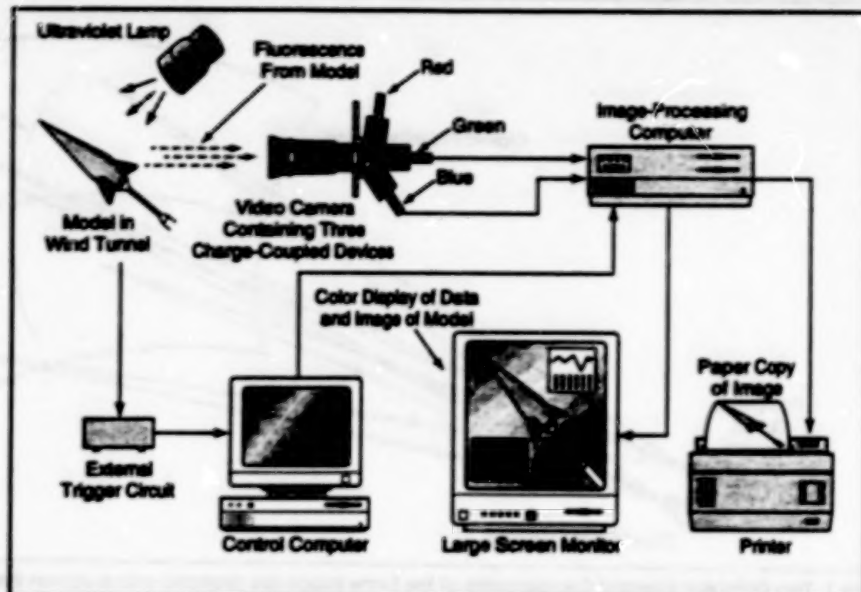


Figure 1. The Video Camera Images Fluorescence emitted by the phosphor-coated model at two wavelengths. The temperature map of the model is then computed from the relative brightnesses in the video images of the model at those wavelengths.

copper (ZnS:Cu). During the wind-tunnel test, the model is illuminated with ultraviolet light at a wavelength of 365 nm. The ultraviolet illumination causes surface luminescence with temperature-dependent spectral peaks at 450 nm (blue) and 520 nm (green). The spatial variation in the color of the luminescence with temperature is imaged with a three-detector color video camera, using its blue-filtered (wavelength 450 ± 20 nm) and green-filtered (wavelength 540 ± 20 nm) detectors. Then by use of the calibration data (see Figure 2), the temperature at each location on the model can be computed from the ratio between the brightnesses of the same location in the blue and green images.

The present CIAS is both portable and capable of producing temperature maps immediately following a measurement sequence. As many as 64 512-by-512-pixel, 8-bit images are stored in each measurement sequence at programmable data-acquisition rates, with a maximum video rate of 30 frames per second.

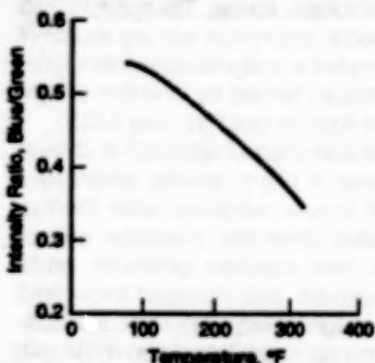


Figure 2. The Ratio Between the Radiometric Brightnesses of the band-pass-filtered light that reaches the blue and green camera tubes from the same location on the phosphor-coated surface is a function of temperature.

This work was done by Gregory M. Buck of Langley Research Center. Further information is contained in a TSP (see page 1).
LAR-14386

Microsensor Hot-Film Anemometer

Features include low thermal inertia, ruggedness, and reduced perturbation of flow.

An improved hot-film anemometer has been developed for making high-bandwidth turbulence measurements in mod-

erate-enthalpy supersonic and hypersonic flows (e.g., NASP inlets and control surfaces, HSCT jet exhaust). Traditional

Langley Research Center,
Hampton, Virginia

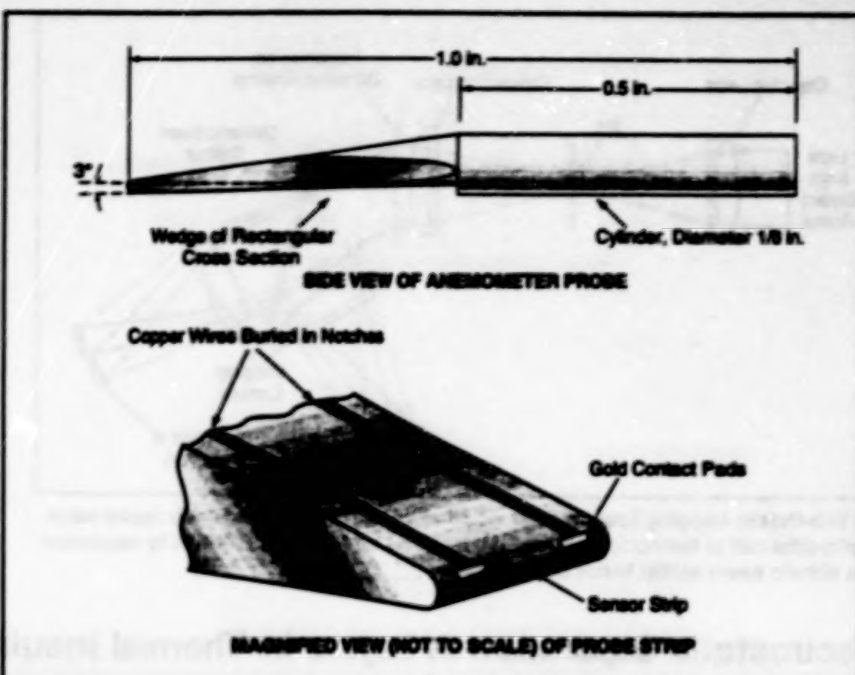
measurement techniques (e.g., hot-wires, LDV) are insufficient to meet the requirements of moderate-enthalpy flows, which

include elevated stagnation temperatures and high dynamic pressures. In addition, existing hot-film designs are not well suited for this purpose, most notably because they lack the bandwidth necessary to resolve the energy-containing portion of such flows.

The development of the improved hot-film anemometer involved the use of advanced materials and state-of-the-art fabrication techniques to achieve a combination of ruggedness and high-frequency response, while minimizing flow perturbation. The hot-film substrate is a 14-degree half wedge (see figure) 0.5 in. (12.7 mm) long by 0.125 in. (3.175 mm) wide, diamond-tooled out of sapphire. The narrow end of the wedge, which faces upstream, is rounded to a radius of 0.2 mm and polished to a surface finish of less than 1 μin . (0.03 μm).

In hot-film anemometry, the fragile wire sensing element used in hot-wire anemometry is replaced with a thin metallic film deposited along the stagnation line of the upstream edge of the substrate, thus increasing mechanical strength. To achieve the low thermal inertia necessary for high frequency response, the sensor strip is made significantly smaller than older hot-film anemometer strips: it is a "dog-bone"-shaped strip of iridium about 3,000 \AA thick by 12.5 μm wide by 0.25 mm long. High spatial resolution is an added benefit of this small size.

The half-wedge geometry shown in the figure was chosen to minimize flow disturbances and enable measurements near the model body. The half-wedge angle of 14° was chosen because it prevents the wedge from generating a detached shock through much of a hypersonic boundary layer. The 3° angle of one side of the wedge is intended to relieve shock-induced disturbances created by the finite curvature of the upstream edge: this will decrease any boundary-layer disturbance



The Microsensor Hot-Film Anemometer is a small strip of iridium on the rounded tip of a sapphire wedge.

that can propagate upstream, improving the accuracy of the measurement.

The iridium sensor strip is formed on the rounded edge of the wedge substrate by a microphotolithographic process. Gold contact pads are formed on the ends of the sensor strip by painting and baking a gold organometallic solution. Thin copper wires for connection to external circuitry are buried in notches and attached to the gold contact pads by use of a silver-filled polyimide adhesive.

The use of iridium as the hot-film material helps to increase thermoelectric stability at high temperatures, since it is the most corrosion-resistant element known. The use of sapphire not only enables the fabrication of a small, precisely shaped and finished anemometer substrate but also enables the anemometer to with-

stand severe temperatures without mechanical failure and without significant changes in dielectric properties. Preliminary testing at mach 6 in air has indicated a frequency response which extends out to over 800 kHz, which represents a five-fold increase over previous designs.

This work was done by Catherine B. McGinley, Ralph Stephens, Purcell Hopson, and James E. Bartlett of Langley Research Center and Mark Shapley and Eric F. Spine of Syracuse University. Further information is contained in a TSP [see page 1].

This invention is owned by NASA, and a patent application has been filed. Inquiries concerning nonexclusive or exclusive license for its commercial development should be addressed to the Patent Counsel, Langley Research Center [see page 1]. Refer to LAR-15112.

Two-Diffraction-Order, Beam-Splitting, Imaging Spectrometer

Spectral images would be made in two wavelength bands.

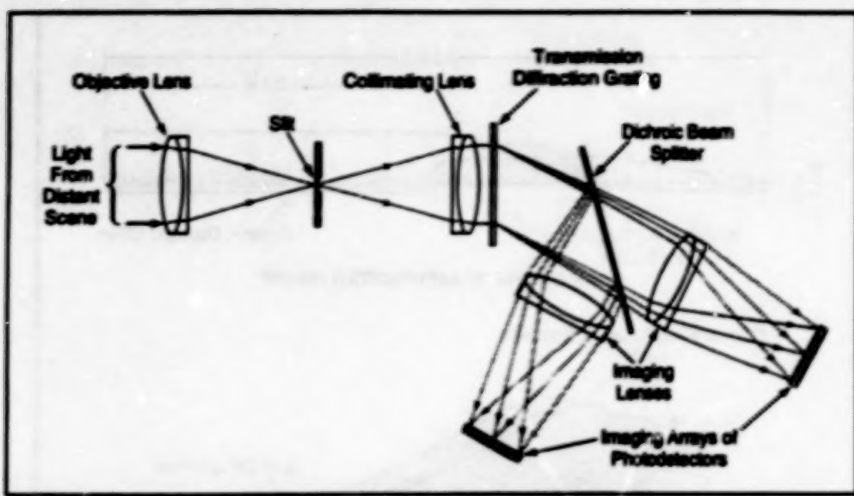
A proposed imaging spectrometer would generate spectral images of a line target in two adjacent, harmonically related wavelength bands: 0.45 to 0.80 μm and 0.90 to 1.8 μm . The conceptual design of the spectrometer calls for a minimum number of optical elements to achieve coverage of the required visible and near-infrared wavelengths in an instrument of reduced size, weight, and cost.

The instrument (see figure) has a single objective lens, which images the scene under observation onto a slit. As in other imaging spectrometers, the slit defines the line-target portion of the scene. A second lens collimates the slit image onto a transmission diffraction grating, which will spectrally disperse the beam. The extent of dispersion would depend on wavelength: For example, 0.9- μm light would be

NASA's Jet Propulsion Laboratory, Pasadena, California

deflected at an angle of 19.67°, while 1.8- μm light would be deflected at 45.28°.

In typical spectrometers, light diffracted to higher orders is regarded as spurious and is reflected and/or absorbed to keep it from the photodetectors. In this instrument, however, the second diffraction order would be utilized. The design of the instrument would exploit the fact that the angle of first-order diffraction of light of a



The Two-Octave Imaging Spectrometer would utilize light of two harmonically related wavelengths diffracted to harmonically related orders at the same angles, followed by separation via a dichroic beam splitter before final imaging.

given wavelength equals the angle of second-order diffraction of light of half that wavelength.

A dichroic, 50-percent transmitting, 50-percent reflecting beam splitter would intercept the diffracted light, separating it into its two component wavelength bands and the corresponding diffraction orders. A separate lens for each band would focus the light onto an imaging array of photodetectors sensitive to the light in that band. Thus, the spectral images would be formed in two octaves covering the required wavelength range.

This work was done by Clayton C. LaBew and Ronald N. Burns of Caltech for NASA's Jet Propulsion Laboratory. Further information is contained in a TSP [see page 1].
NPO-19086

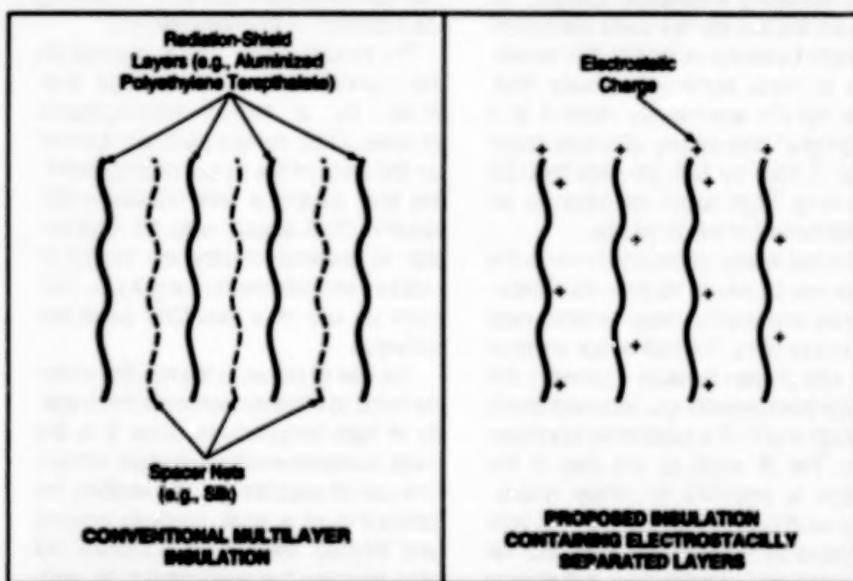
Electrostatic Separation of Layers in Thermal Insulation

Conduction between layers would be eliminated (except at the edges).

The layers of multilayer thermal insulation would be kept apart by electrostatic repulsion, according to a proposal. The insulation in question is of the type used to slow the leakage of heat into Dewar flasks that contain liquid helium. The proposal was originally meant to apply to insulation in cryogenic cooling subsystems of infrared-detector systems in outer space, but it also appears to be applicable to small panels of insulation for terrestrial cryogenic equipment, provided that the layers are contained in evacuated spaces and that the weight of each layer is a small fraction of the electrostatic force upon it.

Typically, a layer consists of a thin sheet of Mylar (or equivalent) polyethylene terephthalate coated with aluminum or gold. The metal coats provide the high reflectivity needed to minimize the radiative transfer of heat through a stack of such sheets. Heretofore, to prevent the conductive transfer of heat that would occur if the radiation-shield layers were allowed to touch, spacer nets made of Dacron (or equivalent) polyethylene terephthalate or silk have been placed between the radiation-shield layers to keep them apart (see figure). Unfortunately, there is some small residual conduction through the spacer nets. At temperatures lower than about 40 K, this residual conduction dominates over radiative-heat transfer for typically achievable layer densities. Hence, to achieve very low heat-leak rates, it becomes very critical to nearly eliminate any conduction between the layers.

NASA's Jet Propulsion Laboratory,
Pasadena, California



Layers in Multilayer Insulation would be charged to keep them separated by electrostatic repulsion, eliminating the need for spacer nets. Removal of the spacer nets would reduce conduction of heat between layers.

According to the proposal, thin channels of conductive material would be embedded in the dielectric substrate of each radiation-shield layer. Once the radiation-shield layers were stacked (without spacer nets) to assemble a panel of insulation, the conductive channels would be used to introduce electric charges of the same polarity into the layers.

The required density of charge in a layer is the amount needed to overcome internal, handling, and fabrication stresses that tend to bend and wrinkle the layers into

contact with each other. The cumulative effect of these stresses can be characterized by the pressure (typically less than 1 kPa) that is applied to hold a panel of stacked layers in place. A charge density of less than 10^{-4} coulomb/m² on each sheet would provide electrostatic repulsion equal to this pressure.

This work was done by Pradeep Bhanderi of Caltech for NASA's Jet Propulsion Laboratory. Further information is contained in a TSP [see page 1].
NPO-18559

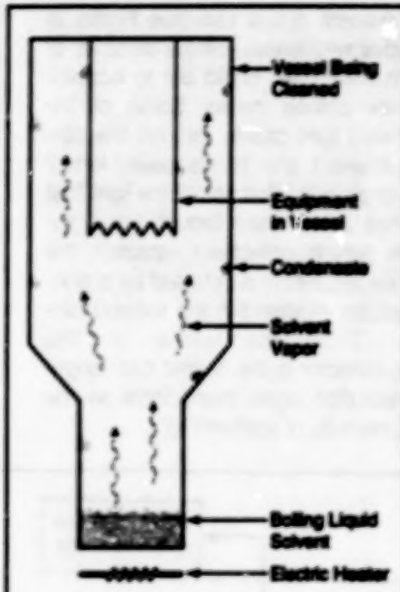
Vapor Degreasing of a Large Tank

Solvent is refluxed to concentrate less volatile contaminants at the bottom.

A vapor degreasing procedure provides for the removal of relatively nonvolatile oils and greases from the insides of large vessels. The procedure can ensure the required degree of cleanliness in high-purity chemical processing and high-vacuum processing vessels. The procedure was devised for, and proved successful in, cleaning a completely-shaped stainless-steel vacuum chamber that contains numerous difficult-to-clean features like screw holes and abutting surfaces.

The procedure begins with the attachment of plumbing to handle the flows of degreasing solvent into and out of the bottom of the vessel. Electric-heating tapes are applied to the bottom of the vessel, which is thus converted temporarily into a solvent boiler. The bottom of the vessel is filled with solvent to a suitable depth and the heat is turned on.

As the solvent boils, heated vapor moves to the upper levels of the tank, where the vapor condenses and dissolves



Solvent is refluxed in a vessel to dissolve oil and grease.

NASA's Jet Propulsion Laboratory,
Pasadena, California

greasy contaminants. The solvent refluxes to the boiler, carrying the dissolved contaminants with it. The procedure can be carried out at a moderate temperature (below 100 °C) if a low-boiling-temperature solvent is used. The vessel need not be pressurized because the vapor is condensed and returned to the boiler. The solvent is removed after refluxing for a suitable time. To achieve a higher degree of cleanliness, the procedure can be repeated.

The solvent can be a chlorofluorocarbon, provided that means are provided to recover most of it and minimize the portion that escapes into the air. Alternatively, a hydrocarbon or other flammable solvent can be used, provided that flammability is tolerable in the particular application.

This work was done by Robert E. Frazer of Caltech for NASA's Jet Propulsion Laboratory. Further information is contained in a T.O.P [see page 1]. NPO-19258

Measuring Thickness of Ice When Liquid Is Present

Capacitances are measured at two frequencies.

A proposed capacitive ice-thickness gauge would give a reliable measurement even when water or other liquid was present within or over the layer of ice. This capability is important for measuring the thickness of ice on an airplane wing or other surface because (1) some liquid water is often present during the formation of ice and (2) even when deicing fluid or heat is applied, there is still a need to measure the thickness of the remaining ice.

Heretofore, dual-geometry capacitive ice-thickness gauges have been used. A gauge of this type comprises two gauges with different electrode spacings to measure the thickness of a layer of ice, independent of the temperature and cleanliness of the ice. The gauge works well if the ice is reasonably homogeneous and no water or other liquid is mixed into or lying over the ice. In the presence of liquid, the apparent electric permeability and conductivity may vary considerably with position from near the electrodes to the outer surface of the ice. Such variations can cause large errors in the gauge readings, making the readings unusable.

The proposed gauge would correct for the effects of liquids by utilizing the known variations of the relative electric permeabilities (popularly called "dielectric constants")

even though they are not constants) of ice and liquids. Because of the mobility of their molecules, liquids respond very rapidly to changes in electric fields. Ice, on the other hand, responds relatively slowly to variations in electric fields because of the constraints of its crystal lattice. Moreover, ice and liquid water both have strong molecular dipole moments. As a result, the relative electric permeability of liquid water remains nearly constant (~60) throughout the range of frequencies (up to more than 10^6 Hz) used to measure it, whereas the relative electric permeability of ice varies from 3.1 at frequencies \geq about 10^4 Hz to more than 80 at frequencies \leq 50 Hz. The exact values of relative electric permeability and the frequency ranges in which the values change sharply with frequency are functions of temperature. In addition, polarization and conductivity affect capacitive measurements and are characterized by rapid responses in both ice and liquids.

In the proposed gauge, the capacitive effects of ice and water (or other liquid) would be measured at two frequencies — for example, 50 Hz and 10 kHz. The capacitance measured at the higher frequency would be subtracted from that measured at the lower frequency. The difference would be related only to the differ-

Langley Research Center, Hampton, Virginia

ence between the corresponding values of the relative electric permeability of ice. The other effects, which would be independent of frequency in the range that includes these two frequencies, would be common to both readings and therefore would be canceled in the subtraction. The absolute level of the difference would vary with temperature and composition, but a correction for this variation would be provided by the dual geometry retained from the previous gauge concept.

The common portion of the signal would be an indication of those parameters that are independent of frequency. The amount of the signal subtracted out would be at least partially indicative of liquid content. The frequencies used in a given case could differ from those mentioned above, as long as the result of the subtraction was reasonably large. Measurements at more than two frequencies might provide more accuracy, but would entail greater effort.

This work was done by Leonard M. Weinstein of Langley Research Center. No further documentation is available.

Inquiries concerning rights for the commercial use of this invention should be addressed to the Patent Counsel, Langley Research Center [see page 1]. Refer to LAR-15061.

Improved Optics for Quasi-Elastic Light Scattering

Spatial resolution is enhanced for better intensity and fluctuation measurements.

Lewis Research Center,
Cleveland, Ohio

An improved optical train has been devised for use in light-scattering measurements like those of quasi-elastic light scattering (QELS) and laser spectroscopy. Measurements of this type are typically performed on solutions, microemulsions, micellar solutions, and colloidal dispersions. In particular, simultaneous measurements of the total intensity and fluctuations in total intensity of light scattered from a sample at various angles (see Figure 1) provide data that can be used, in conjunction with diffusion coefficients, to compute the sizes of particles in the sample.

The present optical train (see Figure 2) includes two lenses, central portions of which have been bored out to accommodate pinhole masks. Some of the scattered light passes through the pinhole in lens 1, then travels toward lens 2 and its pinhole. That part of the light that reaches and passes through both pinholes (which collectively establish the angular resolution) is detected by a photodetector mounted in the second pinhole. Thus, the output of this photodetector is the desired high-angular-resolution signal proportional to the total intensity of scattered light.

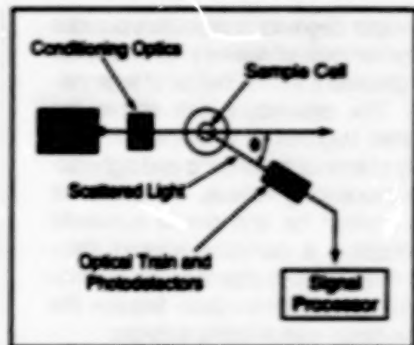


Figure 1. The Laser Beam is Scattered from particles suspended in the sample liquid. The intensity and fluctuations in the intensity of scattered light are measured as functions of θ .

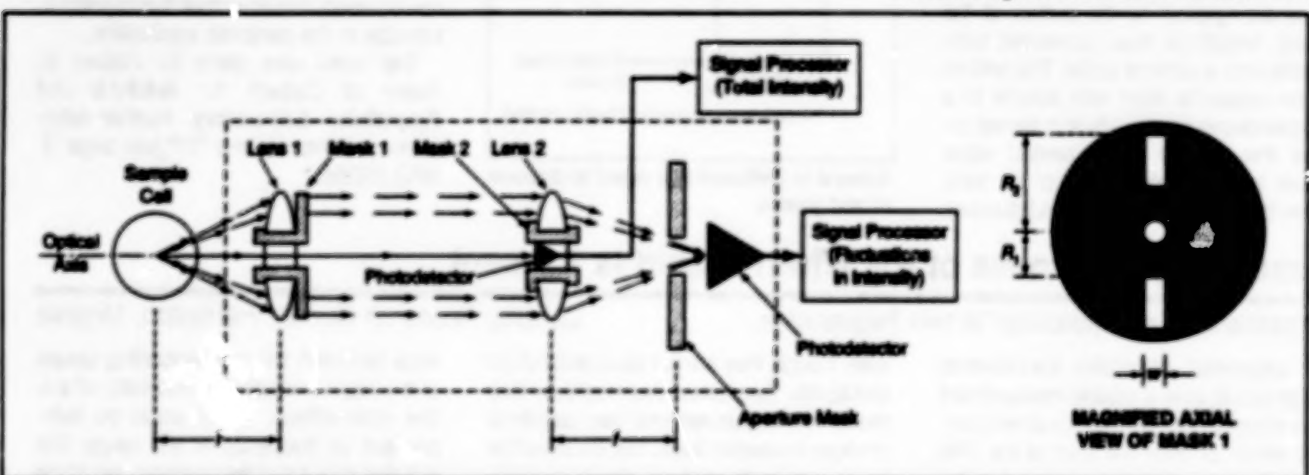


Figure 2. The Improved Optical Train enables simultaneous measurements with both depth and angular resolution.

Accurate determination of the angle of scattering, θ , is essential to the measurement of total intensity. Accurate determination of that plane in the sample from which the light was scattered is essential to the measurement of fluctuations in intensity; this is because light scattered spuriously from the sample/wall and wall/air interfaces of the cell that holds the sample can grossly affect the fluctuation measurement. Thus, there is a need for both a measurement with adequate angular resolution about the optical axis at scattering angle θ and a simultaneous measurement with adequate depth resolution along the same optical axis.

The present improved optical train satisfies these requirements by combining features of an older optical train — in which two pinholes provide angular resolution but no depth resolution — with features of another older optical train, in which lenses provide some depth resolution but inadequate angular resolution.

Lens 1 collimates the light that reaches it. The outer part of the pinhole mask at lens 1 also contains two slits that lie along a diameter perpendicular to the plane in which θ is measured and that pass only those collimated light rays that lie in strips of width w between radii R_1 and R_2 . The parts of the collimated light that survive the slits pass through lens 2, which focuses them onto another photodetector.

By eliminating those rays scattered at angles nearly parallel to the optical axis, the combination of masks and lenses thus selects only those rays that provide depth information. An aperture mask with an aperture of radius R_A discriminates further against light scattered from positions other than at the desired depth within the specimen. The minimum resolvable increment of depth is given by $\Delta z = R_A f / R_1$, (where f = the focal length of each lens) while the minimum resolvable increment of angle is given by $\Delta\theta = 2\arctan(w/2f)$. Thus, the output of the second photode-

tector has both some angular resolution and the depth resolution needed for accurate determinations of fluctuations in intensity.

This work was done by Harry Michael Cheung of the University of Akron for Lewis Research Center. Further information is contained in a TSP [see page 1].

Title to this invention, covered by U.S. Patent Nos. 5,026,135, 5,298,968, and 5,298,969 has been waived under the provisions of the National Aeronautics and Space Act [42 U.S.C. 2457 (f)]. Inquiries concerning licenses for its commercial development should be addressed to

H. Michael Cheung
The University of Akron
Akron, Ohio 44325-3906
Refer to LEW-15621, volume and number of this NASA Tech Briefs issue, and the page number.

Small-Modulation Ellipsometer

Alignment is simple, and no tedious calibration procedure is needed.

The small-modulation ellipsometer is an improved ellipsometer that can be made compact and rugged for operation in harsh environments. Older ellipsometers (the null, rotating-polarizer, and large-modulation ellipsometers) are sensitive to small misalignments and must be calibrated. In contrast, the small-modulation ellipsometer contains no rotating or sliding parts and tolerates small misalignments, and both its calibration parameters and misalignments are computed directly from the outputs of its sensors. Thus, it calibrates itself and operates with a minimum of intervention by a technician, in keeping with the trend to eliminate tedious setup procedures in modern scientific instrumentation.

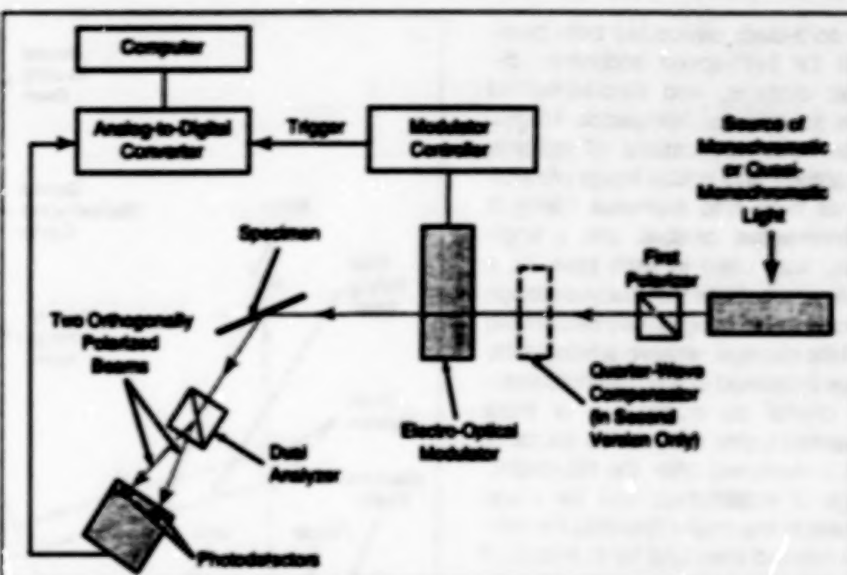
In ellipsometry, one characterizes a specimen of material (usually a thin film) by measuring the change in polarization of polarized light transmitted through the specimen or reflected from the specimen at a glancing angle. Ellipsometry can be used to measure optical constants of specimen materials, thicknesses of layers, roughnesses of surfaces, and anisotropies. Conventionally, the measured reflective polarization effects of a specimen are summarized by converting them into a standard form prescribed by the following equation

$$\frac{r_p}{r_s} = e^{i\Delta} \tan(\Psi)$$

where r_p and r_s denote complex reflection coefficients on two specimen reference planes called "p" and "s," $\tan(\Psi)$ denotes the ratio between the intensity of the p-polarized reflected light and that of the s-polarized light, and Δ denotes the difference between the phases of the p-polarized and s-polarized reflected light. In the case of transmission measurements, each reflection term is replaced by its corresponding transmission term.

The small-modulation ellipsometer provides simultaneous and continuous measurements indicative of $\tan(\Psi)$ and Δ of the specimen. This feature, plus its self-calibration capability and its ruggedness, makes it suitable for real-time monitoring of growth, annealing, treatment, or degradation of specimens.

Marshall Space Flight Center,
Alabama



The Small-Modulation Ellipsometer contains no moving parts and is insensitive to small misalignments. It provides real-time, simultaneous measurements of both ellipsometric parameters, without need for separate calibration measurement or tedious adjustments.

The small-modulation ellipsometer can be assembled in two slightly different versions (see figure). In the first version a beam of monochromatic or quasi-monochromatic light (from a laser, light-emitting diode, lamp with bandpass filter, and the like) is linearly polarized, then sent through an electro-optical modulator, which alters the state of polarization at a chosen frequency that can be as high as several gigahertz. The second version is similar to the first version except that a compensator is inserted between the first polarizer and the modulator. The compensator is a birefringent quarter-wave plate that converts the linear polarization to elliptical or circular polarization. The amplitude of the modulation is kept low so that the change in polarization remains small.

The modulated beam is reflected from the specimen, then passes into a dual analyzer (a polarizing beam splitter) that separates it into orthogonally polarized components. These components are sensed by photodetectors. The outputs of the photodetectors can be processed by use of any or all of a number of techniques that could include analog-to-digital conversion followed by digital computation, analog or digital filtering, lock-in amplification, and/or Fourier analysis. An essential part of the

processing is extraction of the amplitude of the dc components of the photodetector outputs, plus the amplitudes of the components at the modulation frequency and its first few harmonics. By use of a set of approximations that are accurate to second order in the modulation amplitude, M , one can compute $\tan(\Psi)$ and Δ from the amplitudes of the dc, fundamental, and second-harmonic components. To obtain greater accuracy and account for small misalignments, one can compute $\tan(\Psi)$ and Δ by use of another set of approximations that are accurate to fourth order in M and that include the third- and fourth-harmonic components in addition to the lower-frequency components.

This work was done by J. Woolam, B. Johns, S. Ducharme, and H. Machlab of J. A. Woolam Co. for Marshall Space Flight Center. Further information is contained in a TSP [see page 1].

In accordance with Public Law 96-517, the contractor has elected to retain title to this invention. Inquiries concerning rights for its commercial use should be addressed to

J. A. Woolam Co.
650 J Street, Suite 39
Lincoln, NE 68508

Refer to MFS-26235, volume and number of this NASA Tech Briefs issue, and the page number.

Real-Time, Holographic, Dynamic Image-Storage Device

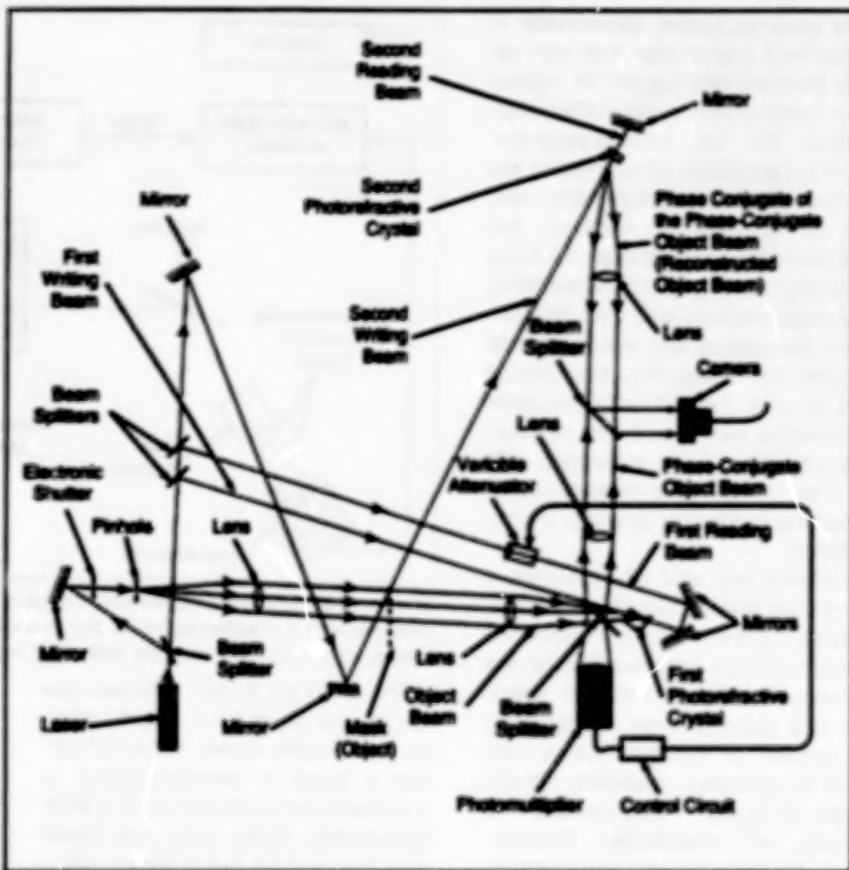
Multiple refractive crystals are used for dynamic storage of images.

Langley Research Center,
Hampton, Virginia

A solid-state device has been developed for high-speed acquisition, dynamic storage, and amplification of three-dimensional holographic images. In previous applications of real-time holography and optical image processing via two- and four-wave mixing in photorefractive crystals, only a single crystal was used in each case. As a result, applications that involved storage of holographic images have been limited to static storage, wherein a holographic image is created in a single photorefractive crystal by mixing two or more coherent beams of light. The source of light is removed after the holographic image is established, and the image remains in the crystal (provided the crystal is isolated from light) for an amount of time that depends upon the charge-migration characteristics of the crystal. The characteristic time (time constant) for retention of an image can range from fractions of a second to years, depending on the crystal. Any exposure to light erases the stored information.

In the present device (see figure), holograms are generated via four-wave mixing in two or more photorefractive crystals (or subelements of a single crystal) to create a single-crystal or multocrystal oscillator. The oscillator acts as a dynamic three-dimensional optical image-storage device (memory), or as the basic unit cell of an optical computer. A hologram is generated within the first crystal (or subelement) by mixing three beams of light that are coherent. One of these beams, denoted the reference or writing beam, is of an intensity much greater than that of the second beam, which is denoted as the object beam. The third beam, denoted the probe or reading beam, is counterpropagating with respect to the reference beam, and is of about the same intensity as that of the reference beam.

The mixing of these three beams in the first crystal creates a phase grating that diffracts a portion of the reading and writing beams. The diffracted beam leaves the crystal as a fourth beam that is the phase conjugate of the object beam and that counterpropagates with respect to the object beam. This phase-conjugated object beam is directed onto a second photorefractive crystal (or



This Four-Wave-Mixing apparatus provides dynamic storage of a holographic image of the object after the electronic shutter is closed to turn off the object beam.

subelement) and is mixed with another coherent reading and writing beam. A phase grating is thus established within the second crystal, and it diffracts a portion of the reading and writing beams into a fourth beam that is the phase conjugate of the phase-conjugated object beam. This beam is directed back to the first crystal to act as the object beam. Thus, the original object beam can be turned off, and the image information is stored in a dynamic way as it oscillates between the two or between more crystals or subelements of a single crystal.

Any material that exhibits photoconductivity or a photovoltaic operation can be used as the photo-refractive crystal. Examples include barium titanate and bismuth silicon oxide crystals, which are sensitive to visible light, plus such semiconductor materials as gallium arsenide and silicon, which are sensitive to infrared light.

This device is expected to provide the capability to store, amplify, process, and transmit time-varying, two-dimensional, spatial information. Possible developments include sensors, actuators, and optical computers that would operate at speeds on the order of the speed of light. This device may have potential in any application in which there is a need for high-speed acquisition and storage of three-dimensional holographic images.

This work was done by Raymond C. Montgomery and Sharon S. LaFleur of Langley Research Center. No further documentation is available.

This invention has been patented by NASA (U.S. Patent No. 4,913,534). Inquiries concerning nonexclusive or exclusive license for its commercial development should be addressed to the Patent Counsel, Langley Research Center [see page 1]. Refer to LAR-13889.

Ultracold-Atom Accelerometers

These accelerometers would be essentially frictionless.

A proposed class of accelerometers and related motion sensors would be based on the use of ultracold atoms as the inertial components of motion transducers. The ultracold atoms would supplant the spring-and-mass components of older accelerometers. As used here, "ultracold atoms" means atoms with kinetic energies equivalent to temperatures ≤ 20 mK.

The atoms would be trapped and cooled by use of laser beams. The motions of the atoms would be sensed via their radiative interactions with laser beams, using Doppler shifts of charac-

teristic absorption and emission spectral lines as measures of the motions of the atoms with respect to the lasers and photosensors. An accelerometer of the proposed type could be designed to focus on a single atom, possibly with the help of an electromagnetic feedback subsystem, that would respond to and regulate the position of the atom relative to a 1 observation window.

The ultracold-atom accelerometers would be essentially frictionless. The primary advantage over other accelerometers would be high sensitivity — even greater than the sensitivity of the best

Marshall Space Flight Center,
Alabama

currently available accelerometers based on electromagnetic interactions with superconducting inertial masses.

This work was done by David A. Noever of Marshall Space Flight Center. To obtain a copy of the report, "Frictionless Accelerometer Technology for Motion Detection Using Ultracold Single Atoms," see TSP's [page 1].

Inquiries concerning rights for the commercial use of this invention should be addressed to the Patent Counsel, Marshall Space Flight Center [see page 1]. Refer to MFS-28979.



Materials

Hardware, Techniques, and Processes

29	Sorbents Remove Oxygen at High Temperatures
30	Films Composed of Diamond and Diamondlike Carbon
30	Superacid-Based Lithium Salts for Polymer Electrolytes

Sorbents Remove Oxygen at High Temperatures

Cobalt-exchanged, platinized zeolites lower equilibrium oxygen levels to < 1 part per trillion

NASA's Jet Propulsion Laboratory,
Pasadena, California

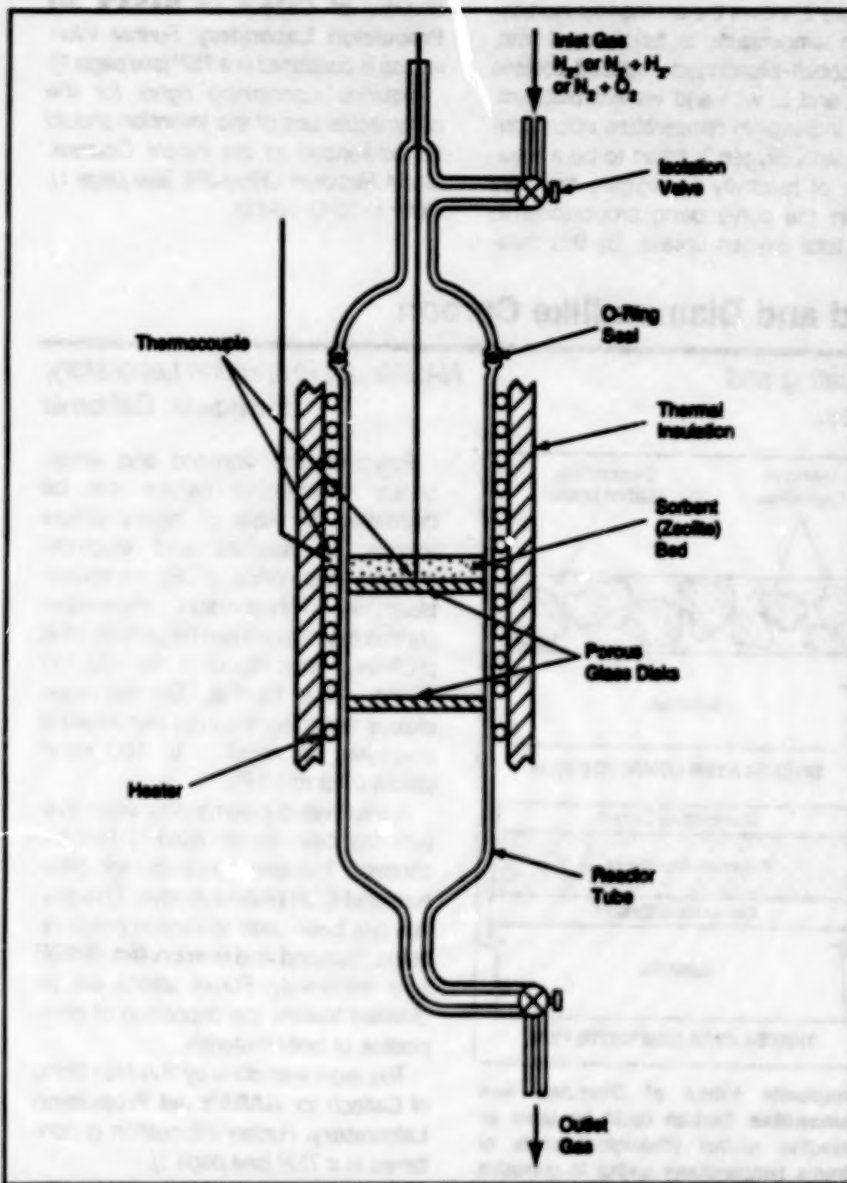


Figure 1. This Reactor Assembly was used to reduce the sorbents, then to test them for ability to chemisorb oxygen.

Cobalt-exchanged, platinized zeolites 13X and L have been found to be conveniently reducible in a hot gaseous mixture of hydrogen and nitrogen and to be thereafter useful as sorbents of trace amounts of oxygen at high temperatures. Aladed by the catalytic action of the platinum, the sorbents exhibit rapid oxygen-sorption kinetics and, according to the thermodynamic properties of the O₂/CoO system, should be capable of lowering the level of oxygen in an otherwise inert gaseous atmosphere to < 1 part per trillion in the temperature range of 400 to 800 °C. Inert atmospheres

with these oxygen levels, which cannot be achieved by use of prior copper-exchanged zeolites, are required for the processing of certain materials in the semiconductor industry.

In experiments, beads of zeolites 13X and L were first treated with a 1-molar aqueous solution of ammonium nitrate to replace Na⁺ in the zeolite by NH₄⁺. The ammonium-exchanged zeolites were then treated with 0.1 molar cobalt nitrate to replace the NH₄⁺ with Co²⁺. After rinsing in distilled water and drying in air at 250 °C, the cobalt-treated zeolites were further treated with an aque-

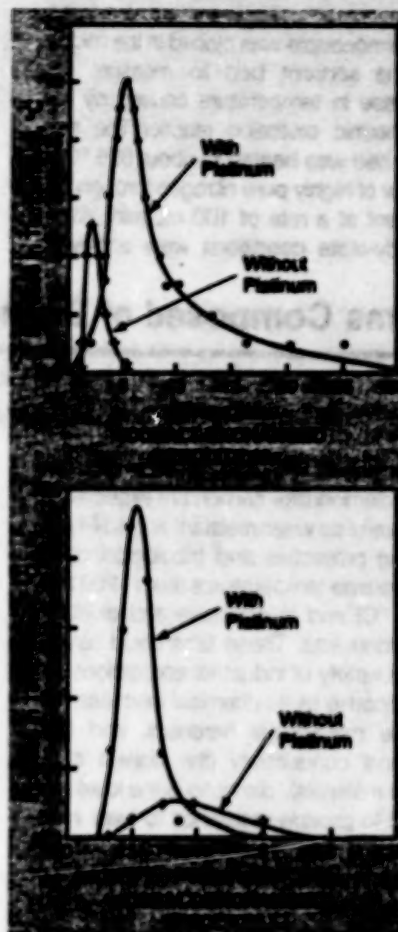


Figure 2. The Increase in Temperature caused by chemisorption of oxygen was measured in reduced sorbents with and without platinum.

ous solution of chloroplatinic acid, H₂PtCl₆, such that the amount of platinum introduced into each zeolite was approximately 0.1 percent of its weight. Each platinum-treated zeolite was then dried in air at 250 °C.

The dried, cobalt-exchanged, platinized zeolites were reduced by heating them in a mixture of nitrogen and hydrogen at a temperature of 600 °C in the system shown schematically in Figure 1. The concentration of hydrogen was gradually increased from 1 percent to 20 percent during 24 hours. At the end of this time, the zeolite beads were found to be fully black in color, indicating that extensive reduction had occurred. (In contrast, when cobalt-exchanged zeolites that did not contain platinum were subjected to the same reducing conditions, there was no appreciable change.)

in color, indicating a general lack of reduction.)

The uptake of oxygen by the reduced sorbents was investigated in the same apparatus as that used for reduction. Before exposing each sorbent to oxygen, a thermocouple was placed in the middle of the sorbent bed to measure the increase in temperature caused by the exothermic oxidation reaction. The sorbent bed was heated to about 625 °C in a flow of highly pure nitrogen through the sorbent at a rate of 100 mL/min. When steady-state conditions were achieved,

oxygen was introduced into the flow at a rate of 10 mL/min, so that a gas mixture consisting of 10 percent oxygen and 90 percent nitrogen flowed through the sorbent bed.

Figure 2 shows the exothermic increases in temperature, as functions of time, for cobalt-exchanged, reduced zeolites 13X and L, with and without platinum. The increase in temperature upon contact with oxygen is taken to be a measure of reactivity to oxygen, the area under the curve being proportional to the total oxygen uptake. By this mea-

sure, the sorbents that contained platinum absorbed much more oxygen than did the corresponding sorbents that did not contain platinum.

This work was done by Pramod K. Sharma of Caltech for NASA's Jet Propulsion Laboratory. Further information is contained in a TSP [see page 1].

Inquiries concerning rights for the commercial use of this invention should be addressed to the Patent Counsel, NASA Resident Office-JPL [see page 1]. Refer to NPO-18409.

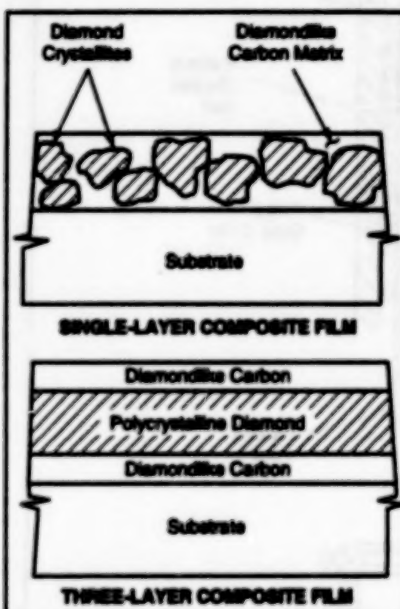
Films Composed of Diamond and Diamondlike Carbon

These films would be used as self-lubricating and protective coats at extreme temperatures.

Proposed films composed of diamond and diamondlike carbon are expected to be useful as wear-resistant and self-lubricating protective and tribological coats at extreme temperatures (from -269 to +600 °C) and in corrosive and oxidizing environments. These films could have a wide variety of industrial applications.

Because of its chemical inertness, extreme mechanical hardness, and high thermal conductivity (the highest of all solid materials), diamond is the ideal material to provide resistance to wear in tribological and protective coats. On the other hand, the characteristics of diamondlike carbon — an amorphous carbon material with a mixture of diamond and graphite molecular bonding configurations — enable it to act as a solid, self-lubricating agent. Therefore, it should be possible to design and fabricate films that are composed of both materials and that exhibit the desired wear-resisting and self-lubricating characteristics.

According to the proposal, two versions of films composed of diamond and diamondlike carbon could be made by chemical-vapor deposition. The upper part of the figure shows a version in which diamond crystallites would be embedded in a matrix of diamondlike carbon. The



Composite Films of Diamond and Diamondlike Carbon could be used as protective and/or tribological coats at extreme temperatures and/or in corrosive environments.

lower part of the figure shows the other version, in which a layer of polycrystalline diamond would lie between two layers of diamondlike carbon.

NASA's Jet Propulsion Laboratory, Pasadena, California

Polycrystalline diamond and amorphous diamondlike carbon can be deposited by use of high-pressure microwave plasmas and electron-cyclotron-resonance (ECR) microwave plasmas. High-pressure microwave plasma depositions can be performed at pressures from about 1 to 100 torr (about 0.13 to 13 kPa); ECR microwave plasma depositions can be performed at pressures of about 1 to 100 mtorr (about 0.13 to 13 Pa).

A microwave plasma deposition system has been constructed to test the concept. It operates in both high-pressure and ECR plasma modes. This system has been used to deposit polycrystalline diamond and diamondlike carbon films separately. Future efforts will be directed toward the deposition of composites of both materials.

This work was done by Yuh-Han Shing of Caltech for NASA's Jet Propulsion Laboratory. Further information is contained in a TSP [see page 1].

Inquiries concerning rights for the commercial use of this invention should be addressed to the Patent Counsel, NASA Resident Office - JPL [see page 1]. Refer to NPO-18501.

Superacid-Based Lithium Salts for Polymer Electrolytes

Performances of solid-polymer-electrolyte/lithium batteries could be enhanced by greater ionic conductivities.

Solid polymer electrolytes that exhibit high lithium-ion conductivities have been made by incorporating salts of superacids into thin films of polyethylene oxide (PEO). These and other solid-polymer elec-

trolytes are candidates for use in rechargeable lithium-based electrochemical cells, wherein increases in the room-temperature lithium-ion conductivities of the solid electrolytes are desirable

NASA's Jet Propulsion Laboratory, Pasadena, California

because they would increase the achievable power and energy densities.

Previously, research on solid polymer electrolytes for lithium batteries had centered around PEO and other organic poly-

mers complexed with lithium salts, which provide the lithium-ion conductivity. The lithium salts that have been used for this purpose include LiI, LiAsF₆, LiCF₃SO₃, LiBF₄, and LiClO₄. Of these salts, only LiCF₃SO₃ is derived from a superacid. ("Superacid" as used here denotes an acid with at least 1,000 times the strength of concentrated sulfuric acid.) Each of the solid polymer electrolytes tested in the previous research either (a) exhibited increased room-temperature conductivity but was made with a polymer that lacked mechanical integrity or (b) was made with PEO, which is mechanically robust, but was insufficiently conductive.

Accordingly, the present PEO/salt-of-superacid solid polymer electrolytes were conceived in an effort to take advantage of the mechanical robustness of PEO

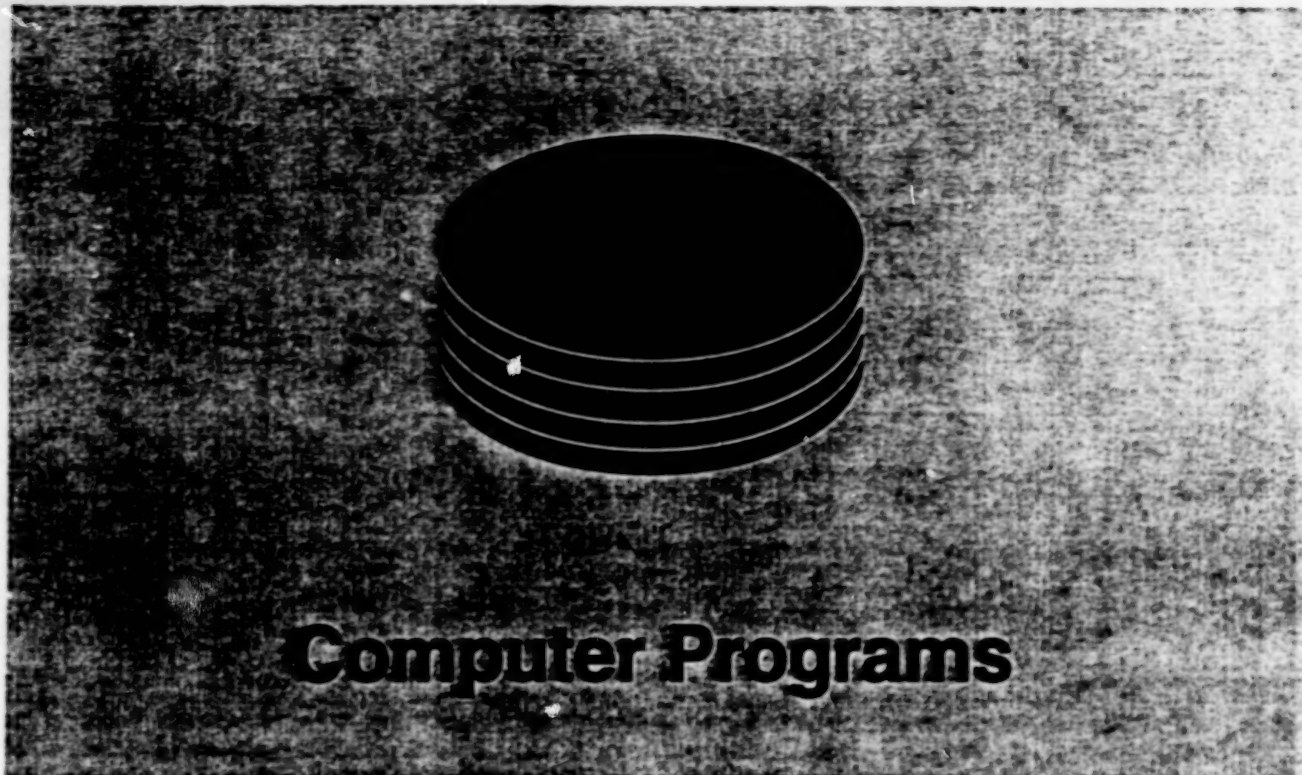
Solid Polymer Electrolyte	Conductivity (mho)
PEDIC ₇ SO ₃ Li	2.00 × 10 ⁻⁸
PEDIC ₉ SO ₃ Li	1.22 × 10 ⁻⁸
PEDIC ₁₁ SO ₃ Li	8.84 × 10 ⁻⁷
PEDIC ₁₃ SO ₃ Li	1.12 × 10 ⁻⁶

The Room-Temperature Conductivities of solid electrolytes that contained recently developed salts of superacids were greater than that of the first-listed solid electrolyte, which contained a previously known salt of a superacid.

while increasing the lithium-ion conductivity. Lithium salts of superacids were chosen in the hope of increasing the concentrations of free lithium ions while loading the PEO with the same proportions of salts as in the previous research.

In experiments, thin films of PEO containing lithium salts of superacids were fabricated by solution casting, in preparation for electrochemical evaluation. The salts used were LiCF₃SO₃ and three recently developed analogs of LiCF₃SO₃. As shown in the table, the room-temperature bulk electrical conductivities of the films (except the one that contained LiCF₃SO₃) ranged from about 43 to about 58 times that of the film that contained LiCF₃SO₃.

This work was done by Ganeshan Nagasubramanian, Surya Prakash, David H. Shen, Subbarao Surampudi, and George Oslar of Caltech for NASA's Jet Propulsion Laboratory. Further information is contained in a TSP [see page 1]. NPO-19286



Computer Programs

Electronic Components and Circuits

33 Computing Radiation From Multiple-Circular-Aperture Antennas

Physical Sciences

33 Computing Fluxes of Molecules on and Near a Spacecraft

Mathematics and Information Sciences

34 Application Portable Parallel Library

Computer Programs

These programs may be obtained from COSMIC. Please contact

COSMIC*

Computer Services Annex

University of Georgia

Athens, GA 30602

Telephone No. (404) 542-3265.

Electronic Components and Circuits

Computing Radiation From Multiple-Circular-Aperture Antennas

Electromagnetic fields are computed in terms of superpositions of circular-waveguide modes.

The Mutual Coupling Program for Circular Waveguide-fed Aperture Array (CWG) computer program was developed to calculate the electromagnetic interactions among elements of antenna arrays with circular apertures with specified distributions of electromagnetic fields in the apertures. The distributions are assumed to be superpositions of the electromagnetic modes that can exist in a circular waveguide. Various external media are included to provide flexibility of use; for example, the flexibility to determine the effects of dielectric covers upon the impedances of aperture-type antennas.

The impedance and radiation characteristics of an antenna that contains a planar array of elements depend upon the mutual interactions among all the elements. These interactions are influenced by several parameters, (e.g., the parameters of the grid on which the array is laid out, the geometry and excitation of each element, the medium outside the array, and the internal network that feeds the array).

In the case of an array antenna in which the radiating elements are small holes in a flat conducting plate, the electromagnetic problem can be divided

into an internal part and an external part. In solving the external part of the problem, CWG computes the mutual interactions among various combinations of circular apertures and distributions of circular-waveguide modes.

CWG computes the mutual coupling among various modes assumed to exist in circular apertures that are located in a flat conducting plane of infinite dimensions. The apertures can radiate into free space, into a homogeneous medium, into a multilayered region or onto a reflecting surface. These apertures are assumed to be excited by one or more modes that correspond to the distributions of modes in circular waveguides of the same cross sections as those of the apertures. The apertures can be of different sizes and different polarizations. However, the program implements the assumption that the fields in all the apertures contain the same distribution of modes, and it calculates a complex scattering matrix that summarizes the interactions among all modes and apertures. The scattering matrix can then be used to determine the complex modal field amplitudes for each aperture in the presence of a specified excitation of the array.

CWG is written in VAX FORTRAN for DEC VAX-series computers running VMS (LAR-15236) and IBM PC-series and compatible computers running MS-DOS (LAR-15226). It requires 350K of random-access memory for execution. To compile the source code for the PC version, the NDP Fortran compiler and linker are necessary; however, the medium for distribution of the PC version of CWG includes a sample MS-DOS executable code that was created by use of NDP Fortran with the -VMS compiler option. The standard medium for distribution of the PC version of CWG is a 3.5-in. (8.89-cm), 1.44MB, MS-DOS-format diskette. The standard medium for distribution of the VAX version of CWG is a 1,600-bit/in. (4630-bit/cm), 9-track magnetic tape in DEC VAX BACKUP format. The VAX version is also available on a TK50 tape cartridge in DEC VAX BACKUP format. Both machine versions of CWG include

an electronic version of the documentation in Microsoft Word for Windows format. CWG was developed in 1983 and is a copyrighted work with all copyright vested in NASA.

This program was written by M. C. Bailey of Langley Research Center.

Further information is contained in a TSP [see page 1].
LAR-15226/LAR-15236

Physical Sciences

Computing Fluxes of Molecules on and Near a Spacecraft

A free-molecular-flow mathematical model with perturbations accounts for nearly free flow.

The Molecular Flux (MOLFLUX) computer code is a versatile program that can be used to compute the following environmental effects induced by a spacecraft: (1) fluxes of molecules to, and deposition of molecules on, surfaces; (2) densities and column densities of molecules in surrounding space, and (3) return fluxes of molecules to surfaces caused by both collisions of the molecules with the ambient atmosphere and by self-scattering. MOLFLUX includes the capability to predict the buildup in the density of ambient gas in front of surfaces exposed to ram conditions by specifying the ambient flux rates for all species impinging on the surfaces. Surface chemical reactions can be represented as rates of emission from surfaces. The user has the option to modify spacecraft configurations and sources of contamination, and to choose which critical surfaces to examine.

MOLFLUX implements a free-molecular-flow mathematical model with perturbations to account for nearly free flow, and therefore appears to be adequate to deal with most applications related to outer space. "Nearly free flow" as used

here includes the mass flow in a thruster plume, with the exception of a small plume volume of viscous and transition flow close to the nozzle from which the plume issues.

The transport function for all species can include a small perturbation (due to molecular collisions) from the free-molecular-flow case, and can be used to calculate backscattering return flux and attenuation of flux. The perturbation applied to the prediction of the basic model is based on a numerical integration of the Bhatnagar, Gross, Krook (BGK-model approximation of the Boltzmann kinetic equation for a mixture of gases. As a result, MOLFLUX is a program of reasonable size and accuracy with maximum flexibility. To enhance flexibility of application, the capability to introduce input data as well as to evaluate output data is left very general and adaptable to the needs of the user.

Mathematical modeling of contamination generally requires addressing the following concerns: (1) the geometry of the spacecraft or other structure, (2) the processes of emission from all sources of contamination, (3) the transport of emitted contaminants, and (4) the induced effects of the contaminants upon critical surfaces and scientific objectives. The first three of these concerns are handled analytically in MOLFLUX. Once contamination levels have been established, other computer programs and analytical techniques can be used to determine the induced effects.

In general, the input of a new space-craft configuration involves development of the necessary geometric relationships and mass-transport factors for that configuration. The most common approach is to use a thermal-radiation program like the Thermal Radiation Analyzer System (TRASYS) program to generate new mass-transport-factor input data for MOLFLUX. Configurations can be geometrically synthesized with TRASYS by use of basic geometrical surfaces and shapes; for example, cones, cylinders, and spheres. The level of detail is selected to assure accurate surface shadowing and to establish adequate surface resolution for compatibility with the various

spacecraft-surface materials and available thermal-profile data. It is not necessary to run TRASYS to use MOLFLUX if the mass-transport-factor data have been precalculated and are available as permanent input data files. These input files must be regenerated only when new configurations are to be evaluated or existing configurations are to be modified.

MOLFLUX is written in FORTRAN and C language for DEC VAX-series computers running VMS. It requires up to 256MB of disk space and 120K of random-access memory for execution. The MOLFLUX software package includes sample executable codes, which were compiled by use of VMS FORTRAN 5.5.1. Sample input and output data files and sample batch files for compiling and linking are also included. The standard medium for distribution of this program is a 1,600-bit/in. (~630-bit/cm), 9-track magnetic tape in DEC VAX BACKUP format. The program is also available on a TK50 tape cartridge in DEC VAX BACKUP format. This version of MOLFLUX, which includes interactive menus, was developed between 1989 and 1992.

This program was written by H. K. Evers of Johnson Space Center and E. R. Rios, C. L. Hayes, and R. T. Rodriguez of Lockheed Engineering & Sciences Co. Further information is contained in a TSP [see page 1].

MSC-22260

Mathematics and Information Sciences

Application Portable Parallel Library

Program facilitates transport of application programs between computers.

The Application Portable Parallel Library (APPL) computer program is a subroutine-based message-passing software library intended to provide a consistent interface to a variety of multi-

processor computers on the market today. The objective of APPL is to minimize the effort needed to move an application program from one computer to another. A user can develop an application program once and then easily move the application program from a parallel computer on which it was created to another parallel computer. ("Parallel computer" may also include a heterogeneous collection of networked computers.)

APPL enables a programmer to think of an application program in terms of communicating processes, without the need to consider the underlying architecture of a computer during the development of the program. The application program can be mapped onto a particular computer architecture at run time. With APPL, this is accomplished by use of an initiator process, with a process-definition file as input.

The primitives in APPL enable a programmer to synchronously or asynchronously send and receive messages between processes. Among other APPL functions are the following: barrier, broadcast, probe, global operations, and other miscellaneous operations common to programming libraries of commercial distributed memory computers.

APPL is written in C language with one FORTRAN 77 subroutine for UNIX-based computers and it is callable from application programs written in C language or FORTRAN 77. The FORTRAN section of code could easily be rewritten in C language, but some FORTRAN vector compilers make this section of code more efficient than a C compiler would. APPL has been successfully implemented on a Sun4 computer running SunOS 4.1, an SGI computer running IRIX4.0.1, an Alliant FX/80-series computer running Concentrix 5.7.00, an IBM RS8000-series computer running AIX 3.1.6, an nCUBE2 computer running release 3.0 of the operating system, and a DEC Alpha computer running OSF/1. APPL requires a minimum of 1MB of random-access memory for execution. The standard distribution medium for APPL is a 0.25-in. (6.35-mm) streaming-magnetic-tape cartridge (Sun QIC-24) in UNIX tar format. Alternate distribution media and

formats are available upon request. The distribution medium for APPL includes both UNIX man pages and an electronic copy of the documentation in PostScript format. The development of

APPL began in 1990 and it was released for distribution through COSMIC in 1993.

This program was written by Gary L. Cole and Richard A. Blech of Lewis

Research Center, and Angela Quasly and Scott Townsend of Sverdrup Technology, Inc. Further information is contained in a TSP [see page 1].
LEW-15572



Mechanics

Hardware, Techniques, and Processes

- 37 Aircraft Sensor Platform Has Increased Angular Range
- 37 Inertial Linear Actuators
- 38 Planning Motions To Avoid Moving Obstacles

Books and Reports

- 39 Stresses in and Near a Bend in a Thin-Walled Duct

Aircraft Sensor Platform Has Increased Angular Range

Translation and rotation are combined to enhance adjustability within limited space.

Goddard Space Flight Center,
Greenbelt, Maryland

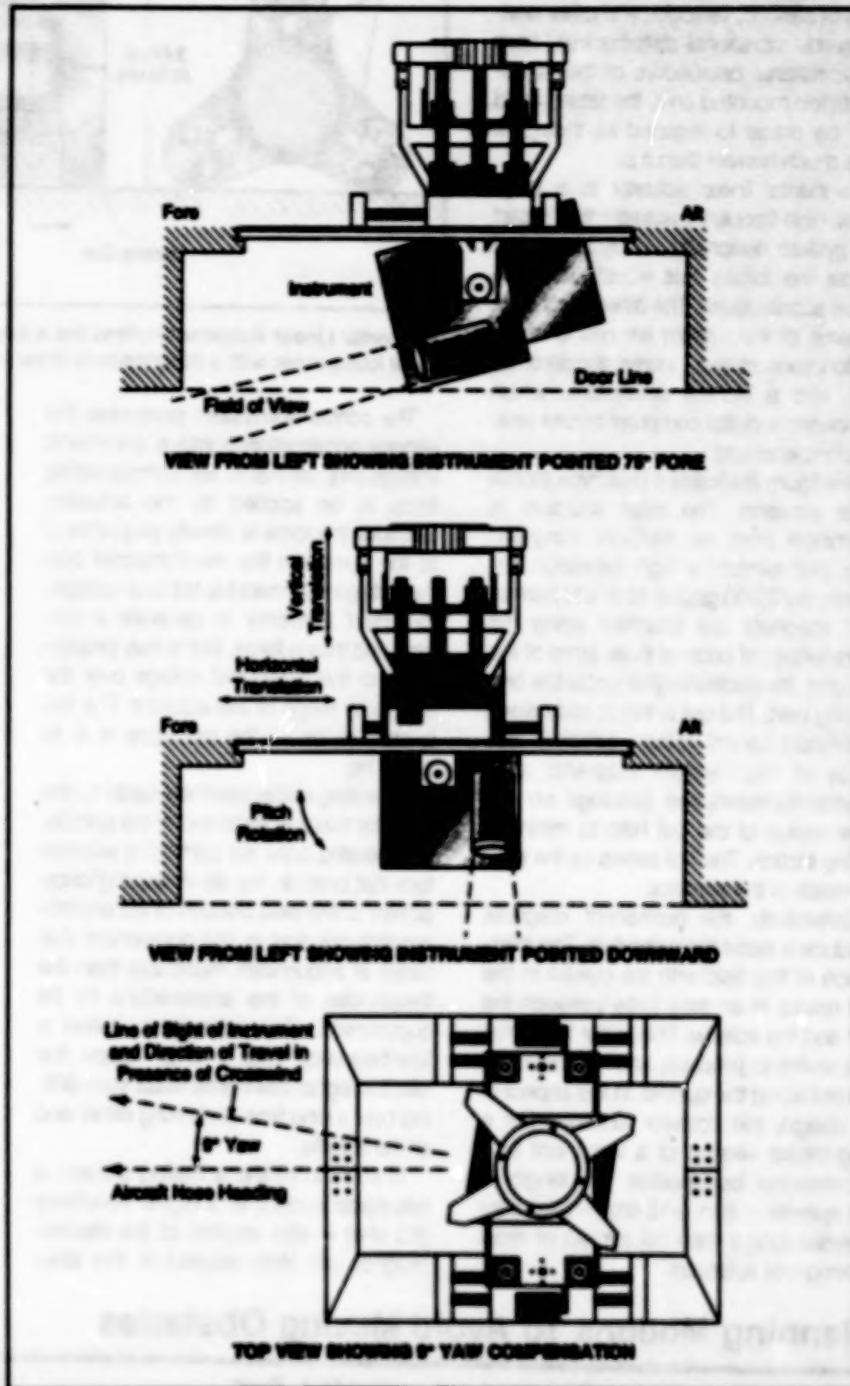
The figure shows selected aspects of a mechanism that rotates and translates an instrument platform within a pressure housing in an aircraft to aim a remote-sensing instrument toward a target on the ground below. In the original application, the mechanism enables an 80-lb (36-kg) imaging spectroradiometer to look 75° fore and 60° aft of the nadir. The mechanism moves the platform and instrument aft and down when pointing the instrument forward, or forward and down when pointing the instrument aft. These movements enable the instrument to look under the aircraft structure at larger fore and aft angles (more than the fore and aft angles of 45° of an older instrument mount) than it otherwise could, without having to deploy the instrument into the air stream outside.

In a typical operation, the instrument is initially positioned down and aft, aimed 75° forward of the nadir as the aircraft approaches the target. As the aircraft passes over the target, the instrument is stepped through a series of pointing angles. When angles of less than 45° forward of the nadir are reached, the instrument platform is moved up and forward to the midpoint between the fore and aft extremes of its translation. When the pointing angle passes 45° aft of the nadir after the aircraft has passed the target, the instrument is moved down and forward. As the aircraft continues to move away from the target, the instrument continues to pivot until it points 60° aft of the nadir.

The mechanism also provides 10° of yaw compensation, thereby reducing further the need for adjustment of the attitude of the aircraft to keep the target in sight. With yaw compensation, the pilot can fly with wings level and nose pointed into the crosswind while on the desired flight path over the target.

This work was done by Philip W. Dabney of Goddard Space Flight Center and Sunetra Bhardwaj of Hughes — STX. Further information is contained in a TSP [see page 1].

GSC-13624



The instrument can be rotated and translated to aim it along lines of sight over a wide range of angles.

Inertial Linear Actuators

Unbalanced masses are pushed and pulled magnetically.

Inertial linear actuators are being developed to suppress residual accelerations of nominally stationary or steadily moving

Lewis Research Center, Cleveland, Ohio

platforms. In the original intended application, the platforms would hold scientific instruments for materials-processing

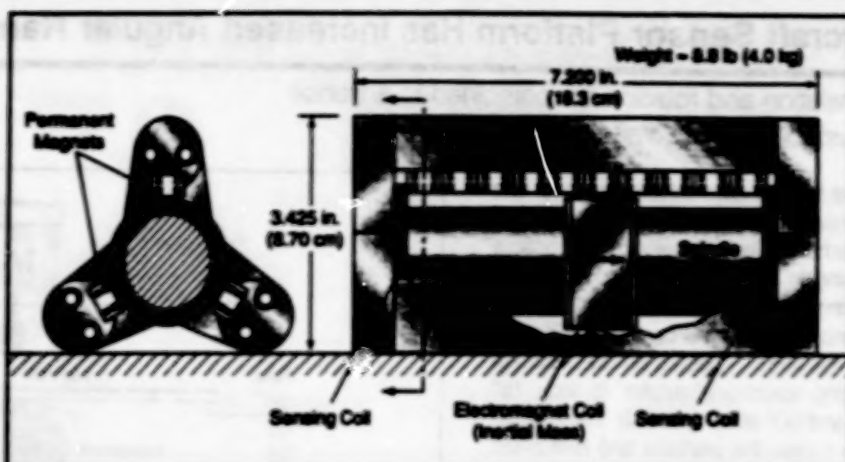
experiments in outer space. The basic concept of the inertial linear actuator should also be applicable to suppression

of vibrations of terrestrial platforms. For example, a laboratory table equipped with such actuators plus suitable vibration sensors and control circuits might be made to vibrate much less in the presence of seismic, vehicular, and other environmental vibrational disturbances; from the vibrational perspective of the instrumentation mounted on it, the table would thus be made to respond as though it were much heavier than it is.

An inertial linear actuator is a long-throw, high-frequency actuator that is part of a system designed to apply forces that cancel the forces that would otherwise cause accelerations. The other major subsystems of the system are one or more motion sensors (e.g., inertial accelerometers) and a control subsystem, which comprises a digital computer and/or analog compensators.

The figure illustrates a prototype inertial linear actuator. The main structure is machined from an Fe/Co/V magnetic alloy that exhibits a high saturation flux density (>23,000 gauss). Nd/Fe/B permanent magnets are attached along the entire length of each of three arms of the actuator. An electromagnet coil is the only moving part. The coil is free to slide along a polished central spindle, which is also made of the Fe/Co/V magnetic alloy. Polytetrafluoroethylene bushings on the inner radius of the coil help to minimize sliding friction. The coil serves as the inertial mass of the actuator.

Collectively, the permanent magnets produce a radial magnetic field. The interaction of this field with the current in the coil results in an axial force between the coil and the spindle. This is the force that one seeks to produce, and it accelerates the coil along the spindle. In this aspect of its design, the actuator functions like a long-stroke version of a voice coil in a conventional loudspeaker. The length of the spindle — 6 in. (~15 cm) — allows for a stroke longer than the strokes of most moving-coil actuators.



An Inertial Linear Actuator functions like a long-stroke version of a voice coil in a conventional loudspeaker, with a superimposed linear variable-differential transformer.

The control subsystem processes the sensed acceleration(s) into a command voltage proportional to the compensating force to be applied by the actuator. Because the force is directly proportional to the current in the electromagnet coil, the voltage command is fed to a voltage-to-current converter to generate a current, and thus a force, that is truly proportional to the command voltage over the frequency range of the actuator. The frequency range of the prototype is 0 to 1,000 Hz.

A sensing coil is attached rigidly to the actuator frame at each end of the spindle. The sensing coils are parts of a subsystem that controls the slowly-varying component of the axial position of the electromagnet coil; that is, the component that varies at frequencies much less than the frequencies of the accelerations to be suppressed. This subsystem, called a low-frequency caging loop, keeps the electromagnet coil/inertial mass from hitting over a long time and hitting either end of the spindle.

In addition to the actuating current, a sinusoidal current at a higher frequency (10 kHz) is also applied to the electromagnet coil. With respect to this sinu-

soidal excitation, the electromagnet coil functions as the primary winding of a variable-inductance transformer. The sensing coils are the secondary windings of this transformer. A simple measurement of the difference between outputs of the two sensing coils indicates the position of the electromagnet coil. In this aspect, the actuator functions as a linear variable-differential transformer. When the electromagnet coil is at the midlength of the spindle, the outputs of the sensing coils are equal in amplitude. When the electromagnet coil is off center, the output of the closer sensing coil exceeds that of the farther sensing coil. The sensing coils are connected in series so that the difference between their outputs can be detected and used to generate a slowly varying control voltage, which is fed back into the drive circuitry to force the electromagnet coil toward the midlength of the spindle.

This work was done by Darren Laughlin of Applied Technology Associates, Inc., for Lewis Research Center. Further information is contained in a TSP [see page 1]. LEW-15533

Planning Motions To Avoid Moving Obstacles

Collision cones in velocity space are computed, then maneuvers are chosen to avoid these cones.

A method of planning the motions of an object to prevent collisions with other moving objects has been derived from the concept of collision cones in relative-velocity space. This method can be considered a prototype of an automated method of planning motions in diverse applications, including complex manu-

NASA's Jet Propulsion Laboratory, Pasadena, California

turing tasks that involve coordination of multiple robots and controlling land, air, and sea traffic.

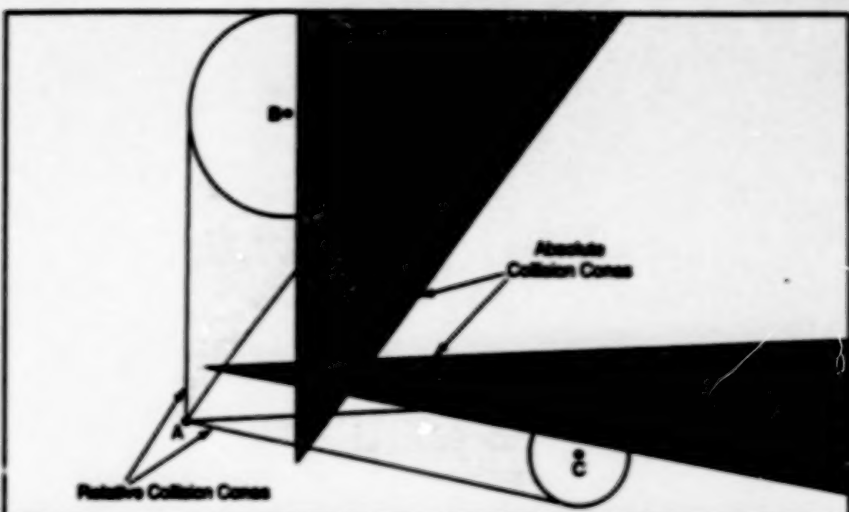
The basic simplifying assumptions that underlie the mathematical model of this method are that (1) both the object undergoing the planned motion (hereafter called simply "the object") and the

other objects (hereafter called "obstacles") are either circles or spheres, depending on whether motions are to be planned in a two- or a three-dimensional space, (2) each obstacle is either stationary or moving on a trajectory that can be approximated by a sequence of straight-line segments, and (3) the

object can travel along a trajectory that is approximated by a sequence of straight-line, constant velocity segments.

With respect to the object and one of the obstacles at their present positions, the collision cone in relative-velocity space is simply the conical range of relative velocities at which continued motion will eventually cause the object and obstacle to collide. The corresponding collision cones for the motion of the object in absolute-velocity space ("absolute collision cones" for short) is four (by translating the relative velocities into absolute velocities). Thus, to prevent a collision with a given obstacle, the object must avoid the corresponding absolute collision cones, which can be regarded as a velocity obstacle.

By extension, one way to prevent collisions with multiple obstacles is to choose a simple straight-line trajectory with a velocity that lies outside all of the applicable collision cones or velocity obstacles (see figure). Of course, in some cases, simple straight-line trajectories that avoid all collision cones will not exist; that is, traveling along any single straight line at any attainable velocity will result in a collision. In such cases, it becomes necessary to choose multiple-segment trajectories such that whenever a velocity must be chosen within a collision cone, there is enough margin of time before the collision so that the



Collision Cones in Velocity Space contain the range of velocities at which continued motion of object A will eventually result in a collision with obstacle B or C, respectively. To avoid a collision, the object must move at a velocity that does not point into the absolute collision cones.

object can avoid the collision by maneuvering to a safe velocity on the next segment of the trajectory.

The basic motion-planning problem then becomes one of choosing the sequence of straight-line segments and the corresponding maneuvers to avoid the collision cones and/or assure sufficient time before collisions on all segments of the straight-line-segment trajectory. Of course, abrupt maneuvers between straight-line segments are not possible in practice, and the trajectory can be computed with dynamic optimization that minimizes travel time or fuel

consumption subject to the dynamic constraints of the object. These factors can be taken into account in optimization algorithms that make use of the space outside the collision cones and use the straight-line-segment trajectory as a nominal trajectory.

This work was done by Paolo Fiorini of Caltech and Zvi Shiller of the University of California, Los Angeles, for NASA's Jet Propulsion Laboratory. Further information is contained in a TSP [see page 1].
NPO-19037

Books and Reports

Stresses in and Near a Bend in a Thin-Walled Duct

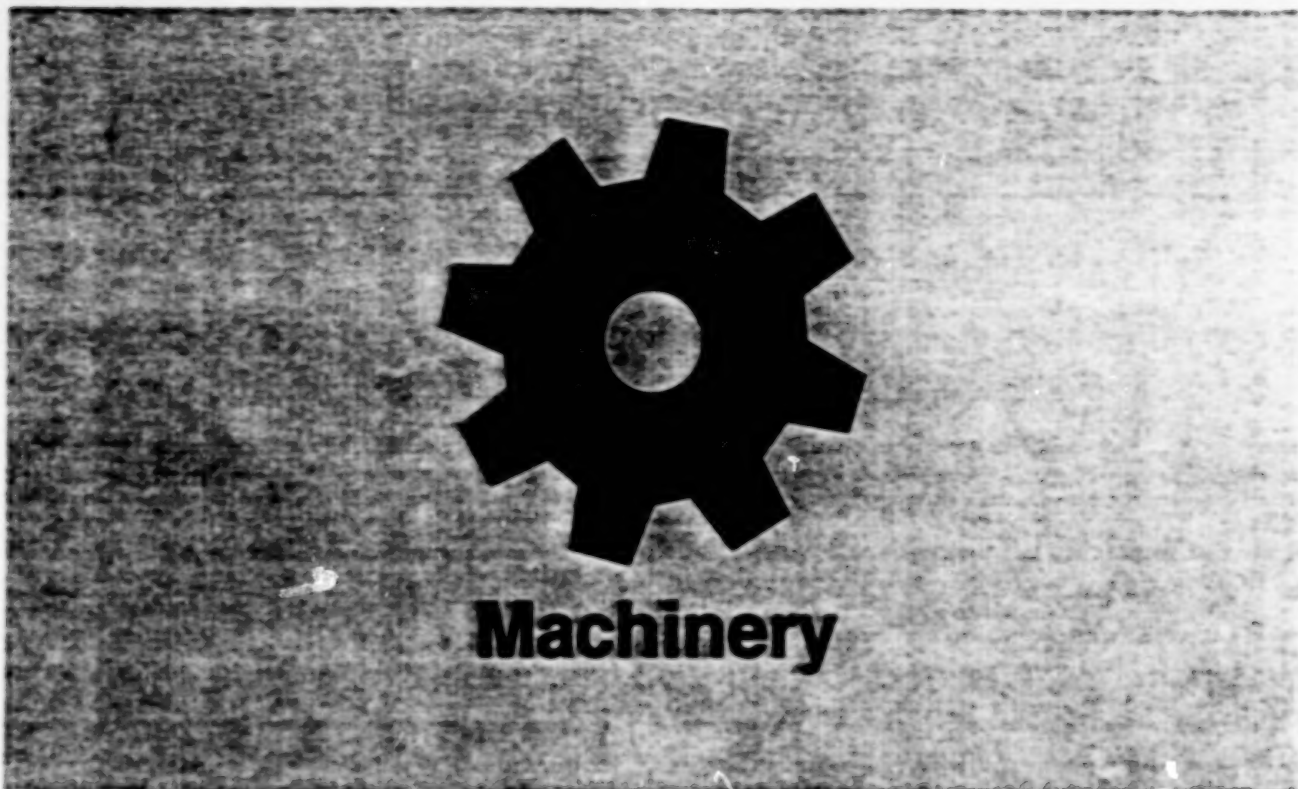
Accurate analysis of stress and longevity depends on clear understanding of effects of various loads.

A report describes a computational study of distributions of stresses in and near a 90° bend in a thin-walled duct subject to various applied loads. The purpose of this study was to help satisfy the need for more accurate knowledge of local concentrations of stresses caused by the loads; such knowledge would make it

possible to design lightweight ducts to survive reasonably foreseeable operating conditions with some degree of reliability. Such knowledge could also guide the selection of locations for mounting strain gauges to measure local stresses for comparison with computed values, thereby contributing to refinement of theoretical concepts and computational techniques. As in other recent studies of stresses in ducts, the calculations in this study were based on the classical theory of homogeneous, isotropic, thin shells within the range of linear elastic behavior, and the equations were solved by a finite-element technique. The numerical results showed that lack of knowledge of detailed stress profiles and locations of peak stresses

under various loads could result in erroneous predictions of structural behavior and fatigue life. For example, strain gauges mounted at the 0°, 90°, 180°, and 270° circumferential locations (where 0° is defined as lying on one of the two flat surfaces tangent to the duct in planes parallel to the plane of bending) for a test in which hot gas flows in the duct would indicate unrealistically low strains, possibly leading to overprediction of fatigue life.

This work was done by J. B. Min and P. K. Agarwal of Marshall Space Flight Center. To obtain a copy of the report "Effect of Type of Load on Stress Analysis of Thin-Walled Ducts," see TSPs [page 1].
MFS-28863



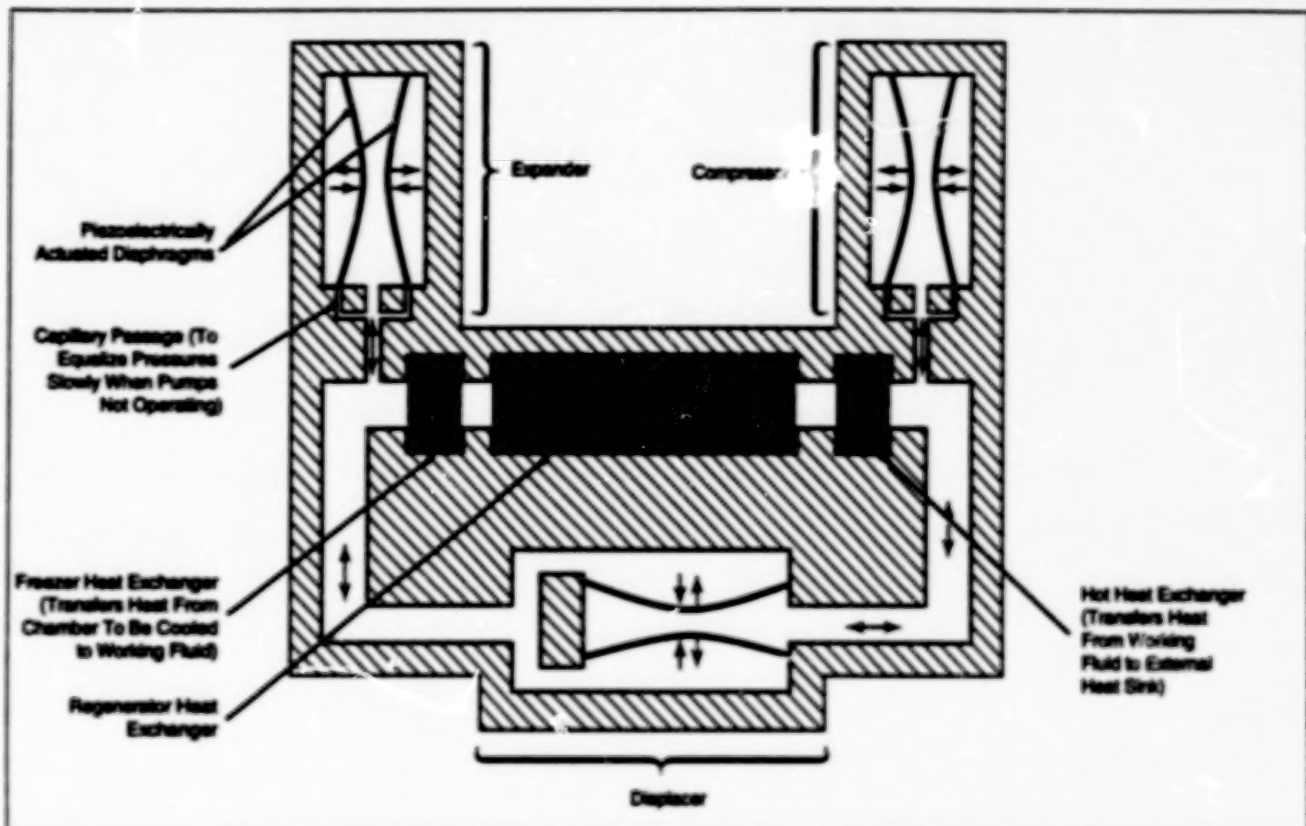
Hardware, Techniques, and Processes

41 Stirling-Cycle Refrigerator Containing Piezoelectric Pumps

Stirling-Cycle Refrigerator Containing Piezoelectric Pumps

Advantages would include greater reliability, relative simplicity, and lower cost.

Langley Research Center,
Hampton, Virginia



This Stirling-Cycle Refrigerator contains three diaphragm pumps in which the diaphragms are opposed, lightweight, reliable piezoelectric actuators. Electrically, these actuators are essentially capacitors; unlike the electric motors of older motor-driven refrigerators, they do not exhibit large resistive heat losses in copper windings and eddy-current heat losses in magnetic cores.

The figure shows an advanced Stirling-cycle cryogenic apparatus that is suitable for cooling sensitive infrared detectors to very low temperatures. The working fluid in this refrigerator is helium. The working fluid is compressed and circulated by three piezoelectrically actuated diaphragm pumps that offer advantages of greater reliability, relative simplicity, and lower cost in comparison with older piston-in-cylinder pumps.

Each diaphragm is a piezoelectric disk that has been chemically reduced on one side to give it a spherical curvature when no voltage is applied. Depending on the polarity of an applied voltage, the diaphragm becomes deformed, via the piezoelectric effect, toward a flatter or more curved shape. Each of the three pumps contains two diaphragms that are simultaneously deformed outward to increase the volume of the pump chamber (to draw fluid in) or simultaneously deformed inward to decrease the volume of the pump chamber (to expel fluid). Because

these deformations involve motion of lightweight parts in opposite directions, the pumping action contributes very little (other than through motion of the fluid) to vibration; this is an important advantage where vibration could disturb a delicately aimed infrared instrument.

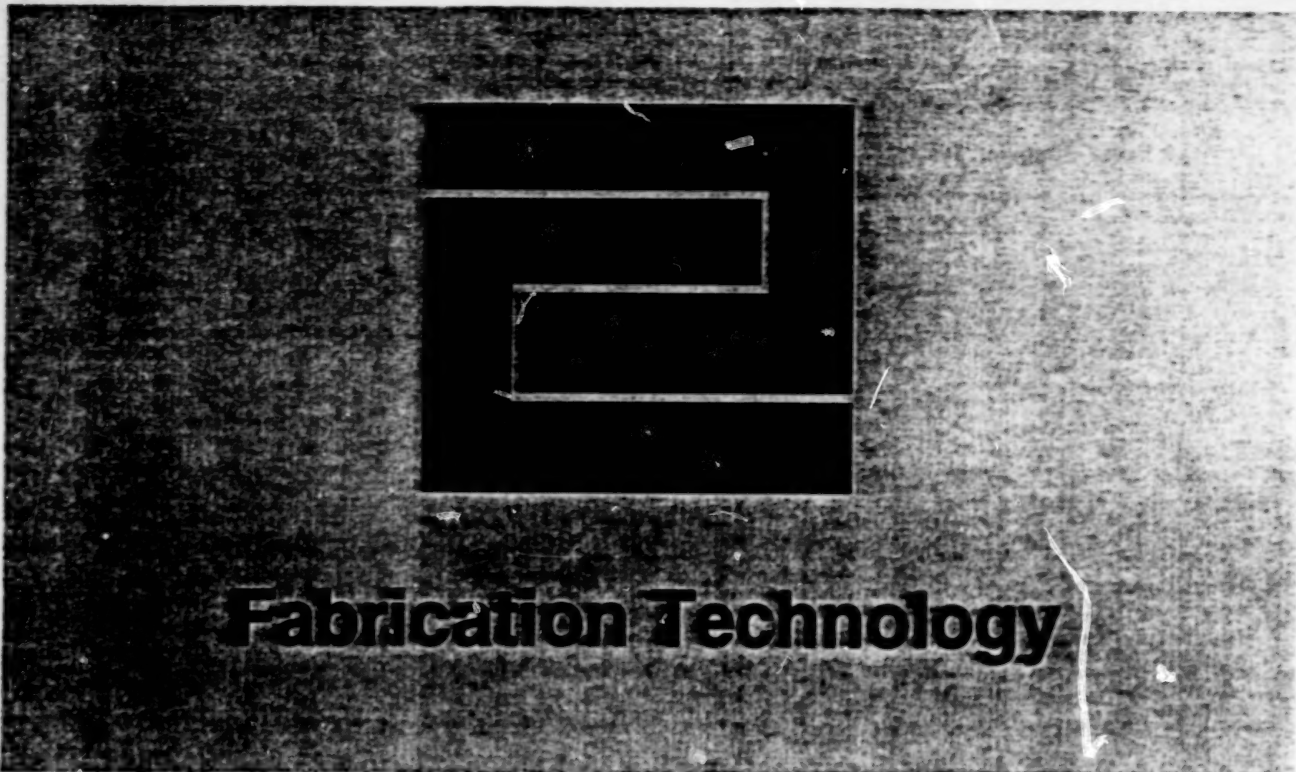
With respect to the compression and expansion of the working fluid, the circulation of the working fluid through the heat exchangers, and the transfer of heat to and from the working fluid, this apparatus operates according to principles that have long been familiar in the technology of refrigeration. One major innovative feature is the use of the piezoelectric pumps. Another major innovative feature is the particular three-pump configuration and pumping sequence, in which one pump serves as a compressor, one pump serves as an expander, and one pump serves as a displacer.

The operation of the pumps is coordinated by synchronizing the piezoelectric-actuator voltages in such a way that the

net effect of the displacer is to reduce the deleterious effect of dead space — that is, to circulate a greater fraction of the working fluid through the heat exchangers than would be possible by use of the compressor and expander alone. In addition, the displacer can be controlled separately to make the flow of working fluid in the heat exchangers turbulent (to increase the rate of transfer of heat at the cost of greater resistance to flow) or laminar (to decrease the resistance to flow at the cost of a lower heat-transfer rate). Thus, the innovative design provides for optimization of the heat-exchanger performance.

This work was done by Anthony Jalink, Jr., and R. F. Halbaum of Langley Research Center. Further information is contained in a TSP [see page 1].

Inquiries concerning rights for the commercial use of this invention should be addressed to the Patent Counsel, Langley Research Center, [see page 1]. Refer to LAR-15065.



Hardware, Techniques, and Processes

- 43 Redesigned Electron-Beam Furnace Boosts Productivity
- 44 Multilead, Vaporization-Cooled Soldering Heat Sink
- 44 Improved Screw-Thread Lock

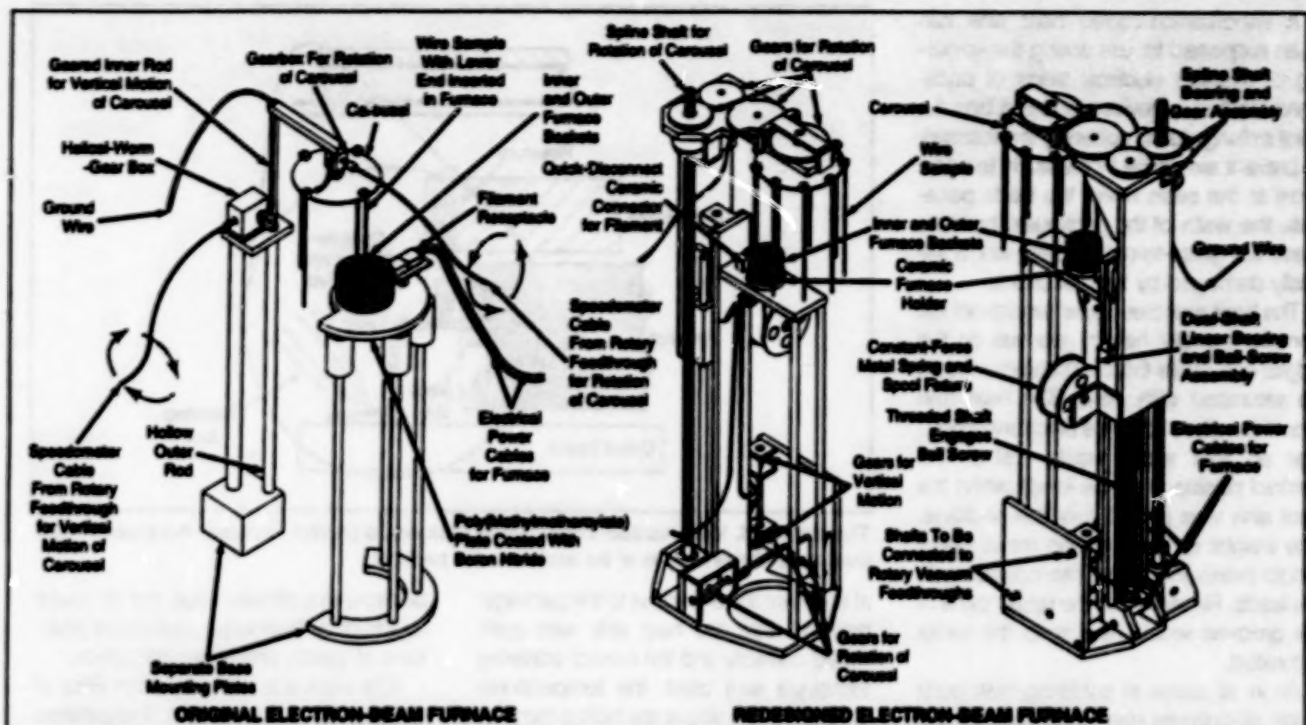
Books and Reports

- 45 More About Plasma-Spraying Ceramics Onto Smooth Metals
- 45 Rocket Combustion Chambers Resist Thermal Fatigue

Redesigned Electron-Beam Furnace Boosts Productivity

Modifications increase the number of experiments per loading, among other benefits.

Marshall Space Flight Center,
Alabama



The Redesigned Electron-Beam Furnace features a carousel of greater capacity so that more experiments can be conducted per loading, and time spent on reloading and vacuum pump-down is reduced. A common mounting plate for the electron source and the carousel simplifies installation and reduces vibration.

An electron-beam furnace has been redesigned to enable it to operate more efficiently and reliably. The furnace melts wires to make drops of molten metals for experiments on processing of materials in a drop tube. Samples of wire on a carousel are moved in sequence into a tungsten-loop filament and an electron-focusing grid, both at a potential of -4,000 Vdc with respect to the wires. Electrons from the filament bombard the tip of the wire in position at a given moment, melting the tip to form drops that fall into the tube.

In the redesigned furnace (see figure), both the source of electrons and the carousel mechanism are mounted on the same plate, whereas they were previously mounted on separate plates. As a result, they can now be installed and aligned more easily and quickly, and they vibrate less. The redesigned furnace holder is smaller and made of a high-temperature ceramic instead of

polymethylmethacrylate so that it outgases less and the vacuum bell jar in which the furnace operates can be evacuated faster.

The position of the main axis of the carousel has been changed, and the diameter of the carousel has been changed so that the carousel can accommodate nine samples of wire instead of only four. The net result of redesign of the carousel is that one can do about 36 experiments (that is, one can make about 36 drops) in a single loading of the carousel instead 8 to 12 experiments in the original design. Thus, productivity is increased greatly, and the time spent pumping down the bell jar is reduced.

The diameter of the outer furnace basket has been reduced and the shape of the inner furnace basket has been altered to give a video camera and pyrometer a better view of melting wires. The outer basket now restrains move-

ment of the inner basket, helping to preserve alignment of the baskets and filament and reducing stress on the filament.

A dual-shaft linear bearing system produces smooth, rigid, vibration-free vertical motion of the carousel. Mitre gears on stainless-steel shafts are linked with rotary feedthroughs by universal swivel joint unions; the linkage eliminates flexible cables and their attendant problems of twisting, jumping, and breakage. For rotation of the carousel, bevel gears are mounted in series on stainless-steel shafts with spur gears to provide a rigid drive.

This work was done by Gary A. Williams of the University of Alabama in Huntsville for Marshall Space Flight Center. Further information is contained in a TSP [see page 1].

MFS-26255

Multilead, Vaporization-Cooled Soldering Heat Sink

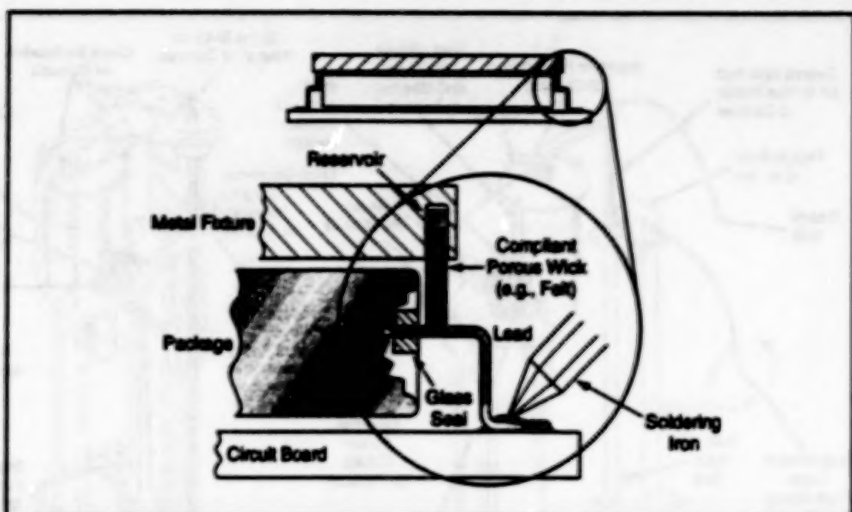
Compliant wicks would be saturated with water.

A vaporization-cooled heat sink has been proposed for use during the soldering of multiple electrical leads of packaged electronic devices to circuit boards. Heat sinking during soldering is necessary to prevent excessive increases in temperature at the seals where the leads penetrate the walls of the packages; typically, these are glass-to-metal seals, which are easily damaged by thermal shock.

The heat sink (see figure) would include compliant wicks held in grooves on the edges of a metal fixture. The wicks would be saturated with water. The heat sink would be sized to fit the electronic package so that wicks would rest in the desired positions on the leads when the heat sink was placed over the package. The weight of the overlying metal fixture would press the wicks into contact with the leads. Reservoirs in the upper parts of the grooves would help keep the wicks saturated.

As in all cases of soldering heat-sunk leads of delicate electronic devices, soldering should be performed quickly. Vaporization of the water in the wicks would limit the temperatures of the leads

NASA's Jet Propulsion Laboratory,
Pasadena, California



The Multilead, Vaporization-Cooled Heat Sink would prevent excessive increases in temperature at the entrances of the leads into the package.

at and near the entrances to the package: provided that the heat sink was positioned correctly and the correct soldering technique was used, the temperatures should not rise above the boiling temperature of water (100 °C at normal atmospheric pressure). In principle, a liquid other than water could be used to limit the tem-

perature to a different value, but of course liquids other than water could pose problems of toxicity and/or contamination.

This work was done by John Rice of Caltech for NASA's Jet Propulsion Laboratory. Further information is contained in a TSP [see page 1].

NPO-19182

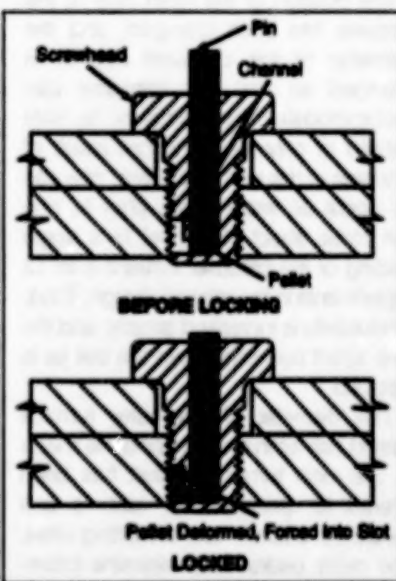
Improved Screw-Thread Lock

A hammer blow activates the locking.

An improved screw-thread lock can be engaged after the screw has been tightened in a nut or other mating threaded part. Unlike some other screw-thread locks, this one does not resist engagement of the screw with the mating threaded part without resistance from a mating part. In addition, this device does not release contaminating material during tightening of the screw, unlike some other screw thread locks that are sheared during tightening and thus release contaminating particles.

The improved screw-thread lock (see figure) includes a pellet of soft material that is encased in the screw and retained by a pin (see figure). The pin protrudes from the screw head. A hammer blow to the pin compresses the pellet and extrudes it through a hole into a slot on the shank of the screw, where the deformed pellet material locks the mating threads together. The

NASA's Jet Propulsion Laboratory,
Pasadena, California



A Hammer Blow on the Pin extrudes the pellet into a slot, where it engages the threads in a threaded hole or in a nut.

pellet and slot can be positioned to lock the screw thread in a threaded hole or in a nut.

This work was done by Malcolm MacMartin of Caltech for NASA's Jet Propulsion Laboratory. Further information is contained in a TSP [see page 1].

In accordance with Public Law 96-517, the contractor has elected to retain title to this invention. Inquiries concerning rights for its commercial use should be addressed to

William T. Callaghan, Manager
Technology Commercialization
JPL-301-350
4800 Oak Grove Drive
Pasadena, CA 91109

Refer to NPO-19010, volume and number of this NASA Tech Briefs issue, and the page number.

Books and Reports

More About Plasma-Spraying Ceramics Onto Smooth Metals

Variations of a previously reported technique are discussed and a specific application is described.

A short paper presents additional information on the fabrication process described in "Plasma-Spraying Ceramics Onto Smooth Metallic Substrates" (LEW-15164), *NASA Tech Briefs*, Vol. 17, No. 4 (April, 1993), page 56. To recapitulate, the process involves optional preoxidation of the substrate surface followed by low-pressure plasma spraying of a thin layer of a thermal-barrier ceramic (zirconia/ytria) onto the substrate, followed by atmospheric-pressure plasma spraying of a second layer of the ceramic onto the first layer. The new paper provides additional information on specific substrate materials such as NiAl-based alloys and composites that could be advantageously coated in the two-stage plasma-spraying process. The paper describes an application of the process to coating specimen substrates of NiAl + 0.1 atomic percent Zr. Specimen substrates coated in this process survived as many as 294 thermal cycles between ambient temperature and 1,200 °C in a burner rig, while specimen substrates coated in an older process survived an average of only 186 cycles.

This work was done by Robert A. Miller and Joseph Doychak of Lewis Research Center. To obtain a copy of the report, "Plasma Sprayed Ceramic Thermal Barrier Coating for NiAl-based Substrates," see TSP's [page 1].

This invention has been patented by NASA (U.S. Patent No. 5,302,465). Inquiries concerning nonexclusive or exclusive license for its commercial development should be addressed to the Patent Counsel, Lewis Research Center [see page 1]. Refer to LEW-15535.

Rocket Combustion Chambers Resist Thermal Fatigue

Gaps accommodate thermal strain.

Lewis Research Center developed an improved design concept for combustion chambers for rocket engines, described in three reports. The improved design concept provides compliance that allows unrestrained thermal expansion in the circumferential direction. This compliance lengthens the life of the rocket engine by reducing the amount of thermal deformation caused by repeated firings. Preliminary results of experiments on subscale models suggest that a suitable compliant design could double or perhaps even quadruple the life of the space shuttle main engine.

A conventional rocket engine combustion chamber contains a copper alloy liner with milled internal channels for coolant. Engine starts and stops subject the liner to thermal strains that exceed the plastic limit by factors of more than 10, and the liner eventually fails by rupture of one or more channels.

A compliant liner consists of an array of copper alloy coolant tubes bonded together to form the inner wall of the combustion chamber by electroforming.

The gaps between the tubes accommodate thermal expansion. Unlike more conventional ways of attaching tubes, such as brazing or welding, electroform bonding is a room-temperature process that does not degrade the properties of the tube material.

In the experiments, subscale models of the tube-lined combustion chamber were tested in laboratory firings under conditions similar to those of actual use. One model was still operational after 637 firings, when testing was stopped. There was no sign of the fatigue cracks that lead to failure in milled-channel combustion chambers, a comparable one of which would be expected to last for only 200 firings under the same conditions. Another subscale model, which was operated at a higher temperature, failed after 256 firings. Its milled-channel counterpart would be expected to last only 118 cycles. There was no evidence of fatigue failure - only simple pressure rupture failure.

This work was done by John M. Kazaroff and Robert S. Jenksovsky of Lewis Research Center and Albert J. Pavli of Sverdrup Technology, Inc. To obtain copies of the reports "Hot Fire Fatigue Testing Results for the Compliant Combustion Chamber" and "Hot Fire Test Results of Subscale Tubular Combustion Chambers," see TSP's [page 1].

Further information is also contained in AIAA paper 92A44509, "Advanced Tube-Bundle Rocket Thrust Chambers." Copies may be purchased [prepayment required] from AEROPLUS, Burlingame, California 94010, Telephone No. (800) 662-2376, Fax No. (415) 259-5047. LEW-15766



Mathematics and Information Sciences

Hardware, Techniques, and Processes

- 47** Learning Identification From One Set of Input/Output Data
- 47** Universal Formulation for Symmetries in Computed Flows
- 48** Cryptography Would Reveal Alterations in Photographs
- 49** Automated Selection of Pictures in Sequences

Learning Identification From One Set of Input/Output Data

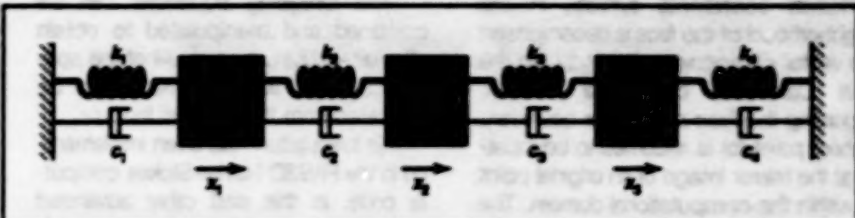
Recursive and nonrecursive techniques are used to estimate Markov parameters in state-space format.

Langley Research Center,
Hampton, Virginia

A method of learning identification from a single set of input/output data has been formulated. To make it possible to explain the significance of this development meaningfully, it is first necessary to define some specialized terms from the discipline of mathematical modeling of multi-variable linear systems like vibrating structures. "Learning" and "identification" as used in this discipline have meanings different from their colloquial meanings. "Identification" is short for "system identification," which means identification of the parameters of a mathematical model that represents the system. "Learning identification" is short for "learning system identification," which is a method of system identification in which new information from successive experiments on a system (e.g., excitation/response tests of a vibrating structure) is used to obtain increasingly refined estimates of the parameters.

In the usual approach to system identification, one determines the time-domain parameters of a system from input/output data (e.g., vibrational-excitation/vibrational-response data). It is customary to average together input/output data from multiple experiments in the hope that averaging will reduce the effects of irregularities such as slight nonlinearities, instrumentation errors, background noise, and repetitive disturbances.

In learning system identification, the parameters to be identified are the Markov parameters. Once the Markov parameters have been found, standard procedures can be used to compute the time-domain parameters. One of the advantages of this approach is that there is no ambiguity in the dimensions of the Markov parameters. Another advantage is that in learning system identification, the Markov parameters are related to input/output data via simple



This Mass-Spring-Damper System, which has six degrees of freedom, was simulated numerically in a test of the algorithm. Even when the order of the system was initially overestimated at 8 or underestimated at 2, 3, 4, or 5, the true order of 6 and all the Markov parameters were recovered at the final step. The algorithm failed only when the order of the system was grossly underestimated at 1.

linear equations and consequently any of the many techniques for handling linear equations can be applied. Yet another advantage is that for a given linear system, the Markov parameters are unique and invariant with respect to any coordinate transformation of vectors that are used to represent the state of the system ("state vectors" for short).

The Markov parameters of a system in state-space format are related to the impulse-response functions of the system, which can be used in identification of modal (as in vibrational modes) parameters. From the identified Markov parameters, such modal parameters as natural frequencies, modal damping ratios, and modal shapes can be deduced by use of standard procedures like the Eigenvalue Realization Algorithm. The Eigenvalue Realization Algorithm is a computational procedure which computes modal parameters from impulse-response functions.

The present method of learning system identification is derived from the previous method by extension of the concept of a repetition domain to include shifting time intervals. In a sense, for the purpose of successive approximation, the input/output data from each successive time interval can be regarded as data

from a new experiment. The present algorithm allows for application of both recursive and nonrecursive techniques to estimate the Markov parameters of a system in state-space format.

The model structure includes the conceptual equivalent of an embedded observer structure that, among other things, places the locations of the poles of the response of the observer system in the complex-frequency plane. The primary role of the observer structure is not to estimate the states of the system for identification, but rather to provide a set of asymptotically stable autoregressive-moving-average (ARMA) equations, the parameters of which can be identified. These parameters contain the desired information about the system. An initial assumption about the order of the system can be removed later by an iterative process (see figure) or by knowledge of an upper bound on the effective order of the system.

This work was done by Jen-Nan Juang of Langley Research Center, Richard W. Longman of Columbia University, and Minh Phan of Princeton University. Further information is contained in a TSP (see page 1).
LAR-14685

Universal Formulation for Symmetries in Computed Flows

Special procedures for coding symmetries of high order are no longer needed.

A universal formulation for high-order symmetries in boundary conditions on flows has been devised. Symmetries that are commonly encountered include symmetries across any or all of the three principal coordinate planes, polar symmetry, and symmetry across wedge sectors. Furthermore complex geometries can exhibit symmetries that are not aligned

with any of the principal coordinate axes. The present universal formulation eliminates the need for special procedures to incorporate such symmetries and the corresponding boundary conditions into computer codes that solve the Navier-Stokes and Euler equations of flow.

In the general case, a flow is computed in a general three-dimensional curvilinear

Langley Research Center,
Hampton, Virginia

coordinate system $\mathbf{x} = (x_1, x_2, x_3)^T$, where the superscript T denotes the matrix or vector transpose. For the purpose of the universal formulation of symmetry, a local Cartesian coordinate system $\mathbf{X} = (X_1, X_2, X_3)^T$ is established at each face of each cell of the computational grid defined by the curvilinear coordinate system (see figure). The three coordinate

axes of X are the inward normal to the face, plus two linearly independent axes in the plane of the face.

A velocity vector (\mathbf{u}) in the general curvilinear coordinate system, \mathbf{U} in the local Cartesian coordinate system) in the neighborhood of the face is decomposed into vector components (U_1, U_2, U_3) in the local Cartesian coordinate system. Regarding the face as a mirror boundary, a ghost point (\mathbf{b}) is assumed to be located at the mirror image of an original point (\mathbf{p}) within the computational domain. The velocity vector \mathbf{U}^P associated with the ghost point is the mirror image of the original velocity vector \mathbf{U}^P ; these two velocity vectors are related by

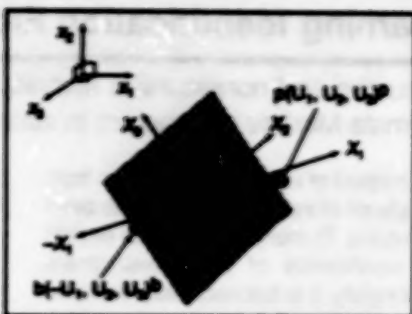
$$\begin{pmatrix} U_1 \\ U_2 \\ U_3 \end{pmatrix} = \begin{pmatrix} -U_1 \\ U_2 \\ U_3 \end{pmatrix}$$

The relationships between the velocities in the two coordinate systems are given by $\mathbf{U}^P = A\mathbf{U}^P$ and $\mathbf{U}^P = A\mathbf{U}^P$, where A is the matrix of direction cosines between the X and z coordinates, given by

$$A = \begin{pmatrix} n_1 & n_2 & n_3 \\ m_1 & m_2 & m_3 \\ l_1 & l_2 & l_3 \end{pmatrix} \text{ and } A^{-1} = A^T$$

The foregoing equations can be combined and manipulated to obtain $\mathbf{U}^P = \mathbf{U}^P - 2U_1(n_1, n_2, n_3)^T$. All of the special cases of flow symmetry can be recovered from this general formula.

This formulation has been implemented in the PAB3D Navier-Stokes computer code. In this and other advanced Navier-Stokes and Euler codes it simplifies the bookkeeping involved in the specification of boundary conditions and provides the flexibility to incorporate symmetrical boundary conditions into computational grids without need for planes of symmetry to be aligned with principal coordinate axes. It provides flexibility for choosing boundary conditions and computational domains in such a way as to save computer memory and computing time; in many cases, the use of these computational resources can be reduced by half or more.



A Local Cartesian Coordinate System is used, along with a global curvilinear coordinate system, to formulate boundary conditions that invoke symmetries of various kinds.

This work was done by S. Paul Pao of Langley Research Center and Khaled S. Abdol-Hamed of Analytical Services and Materials. No further documentation is available.

Inquiries concerning rights for the commercial use of this invention should be addressed to the Patent Counsel, Langley Research Center [see page 1]. Refer to LAR-15148.

Cryptography Would Reveal Alterations in Photographs

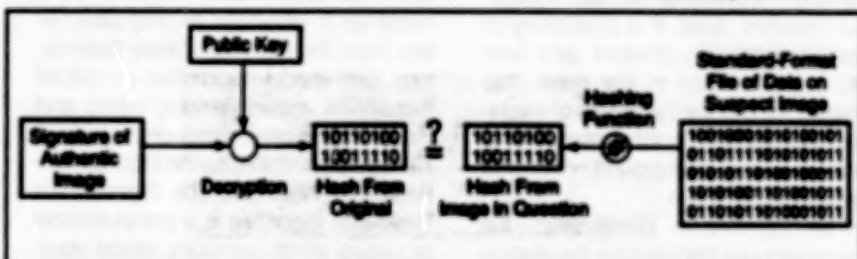
A public key would be used to decrypt a hash of the original image data.

A public-key decryption method has been proposed to guarantee the authenticity of photographic images represented in the form of digital files. The growing practice of altering digitized images by computer-based techniques has made it virtually impossible to verify the authenticity of the images. In the proposed method, a digital camera would generate the original data from an image in a standard public format; it would also produce a coded signature, which could be used to verify the standard-format image data. The scheme also helps protect against other forms of lying, such as attaching false captions.

The figure illustrates the overall coding/decoding verification scheme. By use of a private encryption key, the camera would generate the signature of an image from a hash of the original image data. The hash in this case would be a reduced set of data constructed by a hashing function, which would map values from a larger domain to a smaller range. (The hashing function could be public.) By using a public decryption key that corresponded to the private encryption key, anyone could decode the signature to recover the hash.

Any examiner could verify the authenticity of a suspected image in the following way: The examiner would generate the hash of the suspected image by use

NASA's Jet Propulsion Laboratory, Pasadena, California



The Image-Verification Process would involve comparison of a hash (a mapping) of a suspect image with that of the original image.

of the hashing function. The examiner would also decode the signature of the original image, by use of the public decryption key, to obtain the hash of the original image. Then, the examiner would compare the two hashes. If the hashes matched, the suspected image would be regarded as authentic. If even a single bit of the suspected image file were to be changed, the hashes would not match even approximately.

Within the border of the image, the camera records textural information that can thwart other time-honored methods of image deception. The camera records the date, time, exposure, light levels, and color balance at the time the picture was made. Additional information such as the direction the camera was pointing and Global Positioning Satellite coordinates help prove where in the world you were when the image was recorded.

The use of a public decryption key would not compromise security: the public key could decode correctly only those data that were encoded by use of the corresponding private key; an attempt at forgery by use of a different private encryption key would cause mismatch between the two. This system has the additional advantage of being backward-compatible with existing digital imaging systems.

This work was done by Gary L. Friedman of Caltech for NASA's Jet Propulsion Laboratory. Further information is contained in a TSP [see page 1].

This invention is owned by NASA, and a patent application has been filed. Inquiries concerning nonexclusive or exclusive license for its commercial development should be addressed to the Patent Counsel, NASA Resident Office-JPL [see page 1]. Refer to NPO-19108.

Automated Selection of Pictures in Sequences

Motion-picture frames to be stored or examined are culled by computer.

A method of automated selection of film or video motion-picture frames for storage or examination is undergoing development. Automated selection could be beneficial in situations in which (1) the quantity of visual information available exceeds the amount that can be stored or that can be examined by humans in a reasonable amount of time, and/or (2) it is necessary to reduce a large number of motion-picture frames to a few that convey significantly different information in a manner intermediate between that of a movie and that of a comic book or storyboard. For example, a computerized vision system that monitors an industrial process could be programmed to sound an alarm when changes in the scene exceed normal limits.

The method of automated selection involves preliminary sampling at regular intervals (e.g., the use of the first or last frame in each successive group of a few hundred frames). Each preliminarily sampled frame is digitized, then processed to extract a number of general, primitive features in histogram form. The quantities in the histogram can include hue, saturation, chroma, and grey levels; slopes and intensities of edges; lengths and slopes of lines; and distances of lines from the center of the picture. The data in the histograms are reduced to small sets of numbers, wherein each number is regarded as representing a structural attribute of the entire frame.

To render these numbers to common units of measurement, the mean and standard deviation of each such number over the entire set of preliminarily selected frames is computed so that each such number can be recomputed as a unit normal deviate from a normal curve. Then all the resulting numbers for each frame are added to obtain a single value that is regarded as representative of the entire structure of the frame. The set of such single values derived from all the preliminarily selected images is then regarded as constituting a training set, and the training set is processed to extract its mean and standard deviation. Then the automated selection process is

Lyndon B. Johnson Space Center,
Houston, Texas

based on a simple selection rule: retain those frames, the single representative values of which lie at a specified number of standard deviations from the mean.

At the present state of development, there is no way to guarantee an optimal automatic selection: the choices of the sampling interval, the primitive features to be analyzed statistically, the statistical techniques used to summarize the image data, and the selection rule are all arbitrary. Despite this nonoptimality, a prototype automated-selection algorithm applied to video records of astronaut activity was partly successful in selecting frames that indicated sequences of motions clearly (see figure).

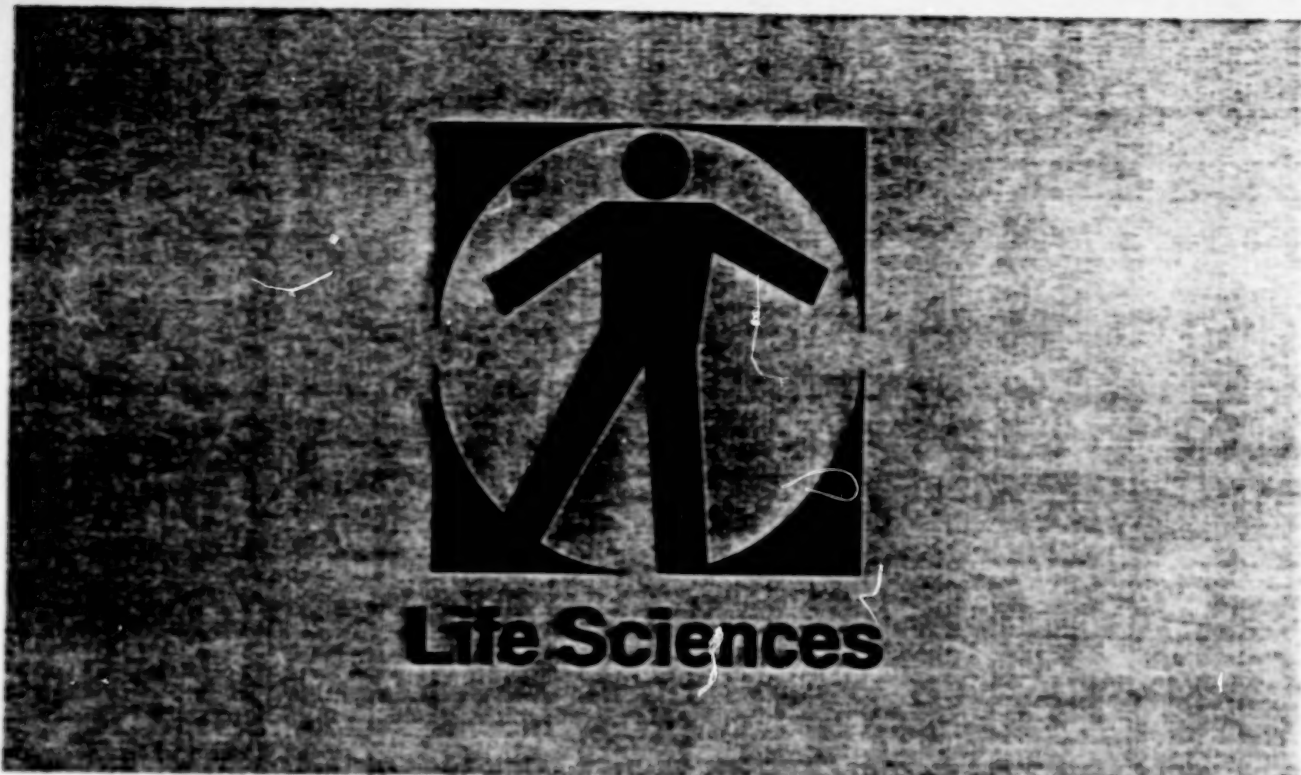
Notably, the frequency of selection within a given sequence was found to be inversely proportional to the number of scenes of the same type, where "type" denotes an average image composition in terms of light levels, edges, and other primitive features. This result is consistent with the fact that this approach to automated selection is based on a model of human attentiveness: at all times, we create mental running distributions of scenes, the distributions change with the addition and deletion of visible objects, and we attend to outliers in the distributions. Despite its sparseness, the model seems to account for a common phenomenon: one is less likely to notice the entry of a single person into a crowded room than into a nearly vacant room.

This work was done by Mark E. Ronig and Robert O. Shelton of Johnson Space Center. Further information is contained in a TSP [see page 1].

This invention is owned by NASA, and a patent application has been filed. Inquiries concerning nonexclusive or exclusive license for its commercial development should be addressed to the NASA Patent Counsel, Johnson Space Center [see page 1]. Refer to MSC-22093.



This Sequence of Images was selected, by the prototype algorithm, from a longer, more complete sequence. This sequence shows the shuttle lift-off.



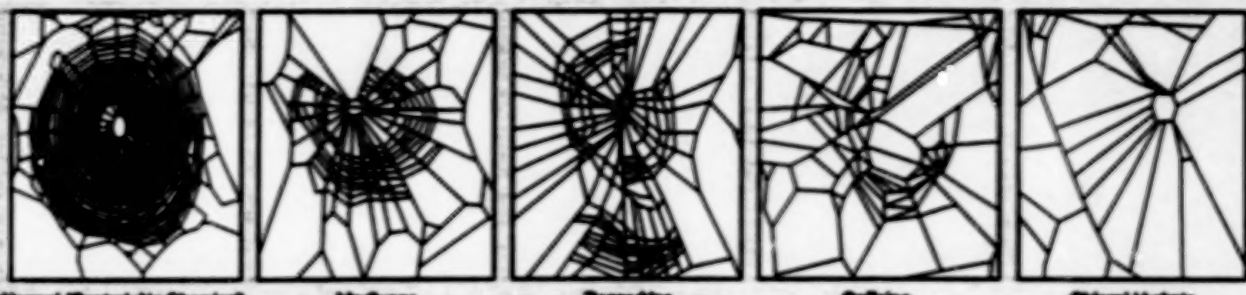
Hardware, Techniques, and Processes

- 51 Using Spider-Web Patterns To Determine Toxicity
- 51 Device Assists Cardiac Chest Compression

Using Spider-Web Patterns To Determine Toxicity

webs are visibly altered when spun by spiders exposed to chemicals.

Marshall Space Flight Center,
Alabama



The Web Spun by an *Araeosa diademata* (House Spider) is altered when the spider is exposed to chemicals. The alterations can be quantified and used as measures of toxicity.

A method of determining the toxicities of chemicals involves recording and analysis of spider-web patterns. The method is based on the observation that spiders exposed to various chemicals spin webs that differ, in various ways, from their normal webs (see figure). Spider-web toxicity testing has potential as an alternative to toxicity testing on higher animals, which is expensive, time-consuming and becoming increasingly restricted by law.

The changes in webs reflect the degree of toxicity of a substance. The more toxic

the chemical, the more deformed a web looks in comparison with a normal web. Inasmuch as the shape of a spider web resembles that of a crystal lattice in some respects, techniques of statistical crystallography are applied to obtain several quantitative measures of toxicity as manifested in the differences between photographs of webs spun under toxic and normal conditions.

The images of the webs are digitized and processed by an image-data-analysis program that computes various measures of

the cellular structures of the webs, including numbers of cells and average areas, perimeters, and radii of cells. It appears that one of the most telling measures of toxicity is a decrease, in comparison with a normal web, of the numbers of completed sides in the cells; the greater the toxicity, the more sides the spider fails to complete.

This work was done by David A. Nover, Raymond J. Oranski, and Rachna A. Patelani of Marshall Space Flight Center. Further information is contained in a TSP [see page 1]. MFS-26921

Device Assists Cardiac Chest Compression

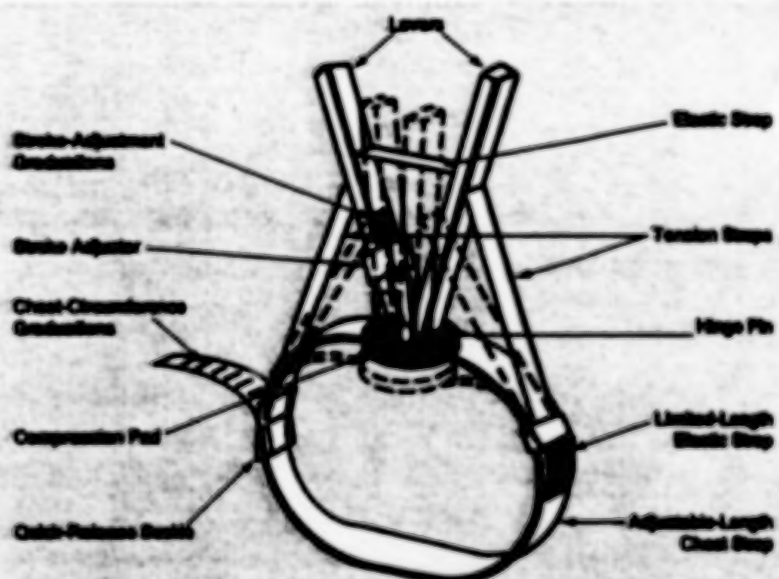
This device enables effective and prolonged resuscitation.

A portable device facilitates effective and prolonged cardiac resuscitation by chest compression. Developed originally for use in the absence of gravitation, the device may also be useful in terrestrial environments and situations (confined spaces, water rescue, medical transport) that are not conducive to standard manual cardiopulmonary resuscitation (CPR) techniques.

The figure shows one version of the device, which is attached to the patient by an adjustable chest strap. Unlike some other devices designed for the same purpose, this one does not require any structural attachments or supplemental restraints; both the patient and the medical technician can be floating.

The device includes a pair of levers hinged to a compression pad, which is positioned on the patient's sternum during attachment. By use of the levers and tension straps, the medical technician applies an effective combination of (1) compression of the entire chest by constriction via the chest strap and (2) localized compression of the sternum via the compression pad. The applied force and

Lyndon B. Johnson Space Center,
Houston, Texas



This Device Can Be Stored Comactly and Deployed Quikly to perform prolonged and effektive CPR.

the length of the stroke can be adjusted to fit the patient's needs. The device applies compression during more than half of the compression cycle, as is desirable for efficient CPR.

This work was done by Frank T. Eichstaedt of McDonnell Douglas Corp. for Johnson Space Center. Further information is contained in a TSP [see page 1]. MSC-22148

National Aeronautics and
Space Administration



END

DATE FILMED

03/14/96